Synchronization in the Second-order Kuramoto Model

Discontinuous phase transitions with frequency-degree correlations and basin stability

D I S S E R T A T I O N

zur Erlangung des akademischen Grades

d o c t o r r e r u m n a t u r a l i u m
(Dr. rer. nat.)
im Fach Physik

eingereicht an der
Mathematisch-Naturwissenschaftlichen Fakultät
der Humboldt-Universität zu Berlin

von
Dipl.-Phys. Peng Ji

Präsident der der Humboldt-Universität zu Berlin:
Prof. Dr. Jan-Hendrik Olbertz

Dekan der Mathematisch-Naturwissenschaftlichen Fakultät:
Prof. Dr. Elmar Kulke

Gutachter:

1. Prof. Dr. Dr. h.c. mult. Jürgen Kurths
2. Prof. Francisco Aparecido Rodrigues
3. Prof. Regino Criado Herrero

Tag der mündlichen Prüfung: 3. September 2015

To my wife and my daughter

Abstract

Synchronization phenomena are ubiquitous in the natural sciences and engineering, but also in social systems. Among the many models that have been proposed for a description of synchronization, the Kuramoto model is most popular. It describes self-sustained phase oscillators rotating at heterogeneous intrinsic frequencies that are coupled through the sine of their phase differences. The second-order Kuramoto model has been used to investigate power grids, Josephson junctions, and other systems. The study of Kuramoto models on networks has recently been boosted because it is simple enough to allow for a mathematical treatment and yet complex enough to exhibit rich phenomena. In particular, *explosive synchronization* emerges in scale-free networks in the presence of a correlation between the natural frequencies and the network topology.

The first main part of this thesis is devoted to study the networked second-order Kuramoto model in the presence of a correlation between the oscillators' natural frequencies and the network's degree. The theoretical framework in the continuum limit and for uncorrelated networks is provided for the model with an asymmetrical natural frequency distribution. It is observed that clusters of nodes with the same degree join the synchronous component successively, starting with small degrees. This novel phenomenon is named *cluster explosive synchronization*. Moreover, this phenomenon is also influenced by the degree mixing in the network connection as shown numerically. In particular, discontinuous transitions emerge not just in disassortative but also in strong assortative networks, in contrast to the first-order model.

Discontinuous phase transitions indicated by the order parameter and hysteresis emerge due to different initial conditions. For very large perturbations, the system could move from a desirable state to an undesirable state. *Basin stability* was proposed to quantify the stability of a system to stay in the desirable state after being subjected to strong perturbations.

In the second main part of this thesis, the basin stability of the synchronization of the second-order Kuramoto model is investigated via perturbing nodes separately. As a novel phenomenon uncovered by basin stability it is demonstrated that two first-order transitions occur successively in complex networks: an *onset transition* from a global instability to a local stability and a *suffusing transition* from a local to a global stability. This sequence is called *onset and suffusing transition*.

Different nodes could have a different stability influence from or to other nodes. For example, nodes adjacent to dead ends have a low basin stability. To quantify the stability influence between clusters, in particular for cluster synchronization, a new concept of *partial basin stability* is proposed. The concept is implemented on two important real examples: neural networks and the northern European power grid. The new concept allows to identify unstable and stable clusters in neural networks and also explains how dead ends undermine the network stability of power grids.

Zusammenfassung

Synchonisation ist ein universelles Phänomen welches in den Natur- und Ingenieurwissenschaften, aber auch in Sozialsystemen vorkommt. Verschiedene Modellsysteme wurden zur Beschreibung von Synchronisation vorgeschlagen, wobei das Kuramoto-Modell das am weitesten verbreitete ist. Das Kuramoto-Modell zweiter Ordnung beschreibt eigenständige Phasenoszillatoren mit heterogenen Eigenfrequenzen, die durch den Sinus ihrer Phasendifferenzen gekoppelt sind, und wird benutzt um nichtlineare Dynamiken in Stromnetzen, Josephson-Kontakten und vielen anderen Systemen zu analysieren. Im Laufe der letzten Jahre wurden insbesondere Netzwerke von Kuramoto-Oszillatoren studiert, da sie einfach genug für eine analytische Beschreibung und denoch reich an vielfältigen Phänomenen sind. Eines dieser Phänomene, *explosive synchronization*, entsteht in skalenfreien Netzwerken wenn eine Korrelation zwischen den Eigenfrequenzen der Oszillatoren und der Netzwerktopolgie besteht.

Im ersten Teil dieser Dissertation wird ein Kuramoto-Netzwerk zweiter Ordnung mit einer Korrelation zwischen den Eigenfrequenzen der Oszillatoren und dem Netzwerkgrad untersucht. Die Theorie im Kontinuumslimit und für unkorrelierte Netzwerke wird für das Modell mit asymmetrischer Eigenfrequenzverteilung entwickelt. Dabei zeigt sich, dass Cluster von Knoten mit demselben Grad nacheinander synchronisieren, beginnend mit dem kleinsten Grad. Dieses neue Phänomen wird als *cluster explosive synchronization* bezeichnet. Numerische Untersuchungen zeigen, dass dieses Phänomen auch durch die Zusammensetzung der Netzwerkgrade beeinflusst wird. Zum Beispiel entstehen unstetige Übergänge nicht nur in disassortativen, sondern auch in stark assortativen Netzwerken, im Gegensatz zum Kuramoto-Modell erster Ordnung.

Unstetige Phasenübergänge lassen sich anhand eines Ordnungsparameters und der Hysterese auf unterschiedliche Anfangsbedingungen zurückführen. Unter starken Störungen kann das System von wünschenswerten in nicht gewünschte Zustände übergehen. Diese Art der Stabilität unter starken Störungen kann mit dem Konzept der *basin stability* quantifiziert werden.

Im zweiten Teil dieser Dissertation wird die basin stability der Synchronisation im Kuramoto-Modell zweiter Ordnung untersucht, wobei die Knoten separat gestört werden. Dabei wurde ein neues Phänomen mit zwei nacheinander auftretenden Übergängen erster Art entdeckt: Eine *onset transition* von einer globalen Stabilität zu einer lokalen Instabilität, und eine *suffusing transition* von lokaler zu globaler Stabilität. Diese Abfolge wird als *onset and suffusing transition* bezeichnet.

Die Stabilität von Netzwerknoten kann durch die lokale Netzwerktopologie beeinflusst werden, zum Beispiel haben Knoten neben Netzwerk-Endpunkten eine geringe basin stability. Daraus folgend wird ein neues Konzept der partiellen basin stability vorgeschlagen, insbesondere für cluster synchronization, um die wechselseitigen Stabilitätseinflüsse von Clustern zu quantifizieren. Dieses Konzept wird auf zwei wichtige reale Beispiele angewandt: Neuronale Netzwerke und das nordeuropäische Stromnetzwerk. Die neue Methode erlaubt es instabile und stabile Cluster in neuronalen Netzwerken zu identifizieren und erklärt wie Netzwerk-Endpunkte die Stabilität gefährden.

Acknowledgements

I am deeply thankful to Prof. Jürgen Kurths for giving me the opportunity to pursue a PhD, the freedom to explore my ideas on synchronizations in the Potsdam Institute for Climate Impact Research (PIK), and especially for his personal supports to my whole family.

I am thankful to China Scholarship Council (CSC) scholarship for generously supporting my work financially.

I thank Thomas Peron and Francisco Aparecido Rodrigues for introducing to me the mean-field approximation which has shaped my interest and for daily fruitful discussions, Peter Menck for his guidance in understanding basic concepts of physics and our first two years' interesting Pappelallee life. I also thank Norbert Marwan and Wenlian Lu for numerous fruitful discussions.

For their comments and suggestions of this thesis, I thank Jakob Runge, Thomas Peron, Prof. Jürgen Kurths, Niklas Boers, Norbert Marwan, and Bedartha Goswami. Furthermore, I want to thank many other people I had the chance to meet and discuss: Jobst Heitzig, Lyuba Tupikina, Veronika Stolbova, Paul Schultz, Chiranjit Mitra's, Julian Maluck, Naoya Fujiwara, Carsten Grabow, Reik Donner, Jasper Franke, Jonatan Siegmund, Edmilson Roque dos Santos, Marc Wiedermann, Frank Hellmann, Xiujing Han, Lixiang Li, Jianquan Lu, Paige Martin, Vivek Kohar, Mirjam Neebe, Lutz Meyer-Ohlendorf, Hong Qu, Tiago Prado, Ellenbeck Saskia, Ye Wu, and Wei Zou and the whole Jürgen Kurths' group in particular Pappelallee mates.

Finally, and most important, I want to dedicate this thesis to my family, my wife Yanyan and daughter Xixi for their love, patience, understanding....

Contents

List of Figures

List of frequently used mathematical symbols

A	Adjacency matrix
$\mathcal{A}$	Assortativity
$\mathcal{BS}$	Basin stability
α	Dissipation parameter
k	Degree
L	Laplacian matrix
λ	Coupling strength
$\langle\cdot\rangle$	Ensemble average
N	Network size
Ω	Natural frequency
ω	Frequency
θ	Phase
t	Time
ψ	Mean phase
r	Order parameter

List of abbreviations

$\mathcal{BS}$	Basin stability (see section 2.2 and Chapter 5)
CES	Cluster explosive synchronization (see Chapter 4)
ES	Explosive synchronization (see Chapter 4)
$\mathcal{PBS}$	Partial basin stability (see Chapter 6)

Chapter 1

Introduction

1.1 The second-order Kuramoto model

Synchronization is a pervasive phenomenon in the natural sciences and engineering, but also in social systems (Arenas et al., 2008). This collective behavior emerges from the interaction of neurons in the central nervous system, power grids, crickets, heart cells, and lasers (Arenas et al., 2008; Pikovsky et al., 2003). Synchronization arises due to the adjustment of rhythms of self-sustained weakly connected periodic oscillators (Acebrón et al., 2005; Arenas et al., 2008; Pikovsky et al., 2003) and can be treated mathematically by the model proposed by Kuramoto (Kuramoto, 1975). Certain species of fireflies, e.g., Pteroptyx malaccae, are able to achieve perfect synchronization even for a stimulating frequency that is different from their intrinsic frequency. In the early 1990s this motivated Ermentrout (Ermentrout, 1991) to propose a model with frequency adaptation which has the ability to mimic such perfect synchrony between coupled oscillators. Acebrón and his coauthors (Acebrón and Spigler, 1998) pointed out that the Kuramoto model without inertia approached the synchronized state too fast compared to experimental observations and an infinite coupling strength is required to achieve perfect synchronization. The adaptive frequency model, where both phase and frequency evolve in time and inertia slows down synchronization, can solve such problems. Strogatz (Strogatz, 2001) and later Trees et al. (Trees et al., 2005) showed that such a model can be obtained from capacitively shunted junction equations to study synchronization in disordered arrays of Josephson junctions. Moreover, Filatrella et al. (Filatrella et al., 2008) derived this model from the classical swing equation to study self-synchronization in power grids.

1.2 Main research questions

The general Kuramoto model assumes that the natural frequencies of oscillators are selected from unimodal and symmetric random distributions (Arenas et al., 2008). In this case, a second-order phase transition to the synchronous state can be observed (Arenas et al., 2008; Acebrón et al., 2005). However, the first-order Kuramoto model can exhibit discontinuous phase transitions (Basnarkov and Urumov, 2008; Basnarkov and Urumov, 2007; Pazó, 2005). For instance, in one of the first works on this topic, Pazó (Pazó, 2005) showed that, if uniform frequency distributions are considered, first-order transitions emerge in fully connected Kuramoto oscillators.

Very recently, Gómez-Gardeñes et al. (Gómez-Gardenes et al., 2011) verified that a discontinuous synchronization transition can also occur in scale-free networks due to a positive correlation between the natural frequencies and network topology. This discovery has triggered many ensuing works, which analyzed explosive synchronization analytically and numerically (Coutinho et al., 2013; Skardal et al., 2013; Chen et al., 2013; Su et al., 2013; Zhang et al., 2013; Zou et al., 2014; Zhang et al., 2015; Leyva et al., 2012; Peron and Rodrigues, 2012a), but on the first-order Kuramoto model.

Following these works, our first main research question is

1. What determines the synchronization transition in the second-order Kuramoto model if the dynamics is correlated with the network topology?

To tackle this question, we firstly consider an ideal situation in uncorrelated networks and the continuum limit, where the network size $N \to \infty$, based on the theoretical framework derived by Tanaka et al. (Tanaka et al., 1997a; Tanaka et al., 1997b). The main difficulty here is to derive the self-consistent equation of the mean-field quantities when the frequency distribution is asymmetric. We then investigate effects of assortative mixing on the network synchronization in the presence of a positive correlation between a heterogeneity of connections and the natural frequencies.

Discontinuous phase transitions and hysteresis emerge due to frequency-degree correlations. Given perturbations, the system could jump from a desirable state to an undesirable state. To quantify the probability of the system returning to the desirable state after being subjected to a large perturbation, Menck et al. (Menck et al., 2013; Menck et al., 2014) proposed the concept of basin stability. This measure quantifies the basin of attraction of a desirable state, which can be non-local and nonlinear which is why basin stability can also be applied to high-dimensional dynamical systems to assess the stability of states.

Many complex networked systems, ranging from power grids to neural networks, consist of many components (clusters) and exhibit multistability. A fundamental property of complex networks is that perturbations on one component can significantly affect other components and potentially trigger cascading failure in power grids (Machowski et al., 2011) or cause functional impairment on human brain activation (Schnitzler and Gross, 2005). In realistic situations, a certain degree of perturbations are largely unavoidable. If the system is multistable, then it is hard to prevent a perturbed component jumping from one state to another. The problem is now whether it is possible to obtain a likelihood for retaining a desirable state from a statistical point of view.

This leads us to the second main research question

2. How to adapt the concept of basin stability to cluster synchronization?

To tackle the second question, we start by approximating basin stability as a function of parameters including the dissipation parameter, the coupling strength and the natural frequency in uncorrelated networks and in the continuum limit. To adapt the situation of cluster synchronization, we propose a novel concept of *partial basin*

stability ($\mathcal{PBS}$). This measure allows to quantify the likelihood that a component m returns to a desirable state after another component a has been subjected to a perturbation. $\mathcal{PBS}$ is related to the relative attracting basin of the desirable state and provides a directed stability influence from component a to m.

Before addressing the above two questions, we explore the low-dimensional behavior of the second-order Kuramoto model. The low-dimensional behavior of the first-order Kuramoto model has been discussed by Watanabe and Strogatz (Watanabe and Strogatz, 1994) for identical oscillators and was further developed by Ott and Antonsen (Ott and Antonsen, 2008) for phase density functions with a Poisson kernel. On the other hand, the low-dimensional behavior of the second-order Kuramoto model still remains to be investigated.

1.3 Contents and main findings

The study of Kuramoto oscillators in complex networks has been boosted thanks to rigorous mathematical treatments such as the Ott-Antonsen ansatz (Ott and Antonsen, 2008), the mean-field approximation (Strogatz, 2000), or stability analyses (Menck et al., 2013). The main novel contributions of this thesis are the study of the low-dimensional behavior of the second-order Kuramoto model with inertia by an extension of the Ott-Antonsen ansatz (Chapter 3), the mean-field approximation of the second-order Kuramoto model (Chapter 4), and advanced stability analyses (Chapters 5 and 6).

The detailed contents of this thesis are as follows:

Chapter 2 provides an overview over the literature on the derivation of the second-order Kuramoto model, the mean-field approximation, and the basin stability concept.

In Chapter 3, we generalize the Ott-Antonsen ansatz to second-order Kuramoto models in complex networks. With an additional inertia term, we find a low-dimensional behavior similar to the first-order Kuramoto model, derive a self-consistent equation and derive the time-dependence of the order parameter.

Correlations between intrinsic dynamics and the local topology have recently become very popular in the study of synchronization in complex networks. In Chapter 4, we investigate the influence of network topology on the dynamics of networks made up of second-order Kuramoto oscillators. In particular, based on mean-field calculations, we provide a detailed investigation of the phenomena of *cluster explosive synchronization* (CES), analyzing the model in scale-free and small-world networks as a function of several topological properties. We show that, in contrast to scale-free networks, the transition to the synchronous state in small-world structures tends to be continuous as the probability of rewiring increases. Moreover, we investigate the robustness of discontinuous transitions by including an additional quenched disorder, and we show that the phase coherence decreases with increasing strength of the quenched disorder. In the presence of a positive correlation between the heterogeneity of connections and the natural frequencies in scale-free networks, we numerically show that discontinuous transitions emerge not just in disassortative, but also in strongly

assortative networks, in contrast to the first-order Kuramoto model. We also find that the effect of assortativity on network synchronization can be compensated by adjusting the phase damping. Our results show that it is possible to control collective behavior of damped Kuramoto oscillators by tuning the network structure or by adjusting the dissipation related to the phases movement. These results complement the previous findings regarding CES and also fundamentally deepen the understanding of the interplay between topology and dynamics under the constraint of correlating natural frequencies and local structure.

In Chapter 5, we use basin stability in complex networks of second-order Kuramoto models to demonstrate a novel phenomenon where two first-order transitions occur successively: an *onset transition* from an unstable to a locally stable synchronous state, and a *suffusing transition* from a locally stable to a globally stable synchronous state; we call this sequence *onset-suffusing transitions* and provide an analytical treatment of basin stability by a mean-field analysis. Considering small networks, we start by investigating the global basin stability of a single-node system and then extend it to two and four oscillators. We calculate the basin stability of the stable fixed point over the whole parameter space, in which different parameter combinations give rise to a stable fixed point and/or a stable limit cycle depending sensitively on initial conditions.

In Chapter 6, we adapt basin stability to evaluate the stability of partial synchronization, which plays a pivotal role in a wide variety of engineered and natural systems. The novel stability measure, *partial basin stability*, is demonstrated on two important real data case studies: neural networks and the northern European power grid. In the case study of neural networks, a patient group of schizophrenia is compared to a healthy control group. We are able to detect abnormal regions (the precuneus and the left middle occipital gyrus) in the human brain from a dynamical point of view which confirms previous findings based on observations. For the northern European power grid, we provide new insights and uncover the local mechanisms of how dead ends diminish power grid stability. Summarizing, the analyses of stability in real systems can provide a better understanding of the interplay between structure and collective behavior.

Finally, Chapter 7 concludes the main results of this thesis and discusses promising avenues for future research.

Chapter 2

Mean-field analysis and stability

The second-order Kuramoto model consists of an ensemble of network coupled phase oscillators θ_i, for $i = 1, \ldots, N$, and whose dynamics are governed by

$$\ddot{\theta}_i = -\alpha\dot{\theta}_i + \Omega_i + \lambda \sum_{j=1}^{N} A_{ij} \sin(\theta_j - \theta_i), \tag{2.1}$$

where Ω_i is the natural frequency of the i-th oscillator with a given probability density $g(\Omega)$, α is the dissipation parameter, λ is the coupling strength and A is the adjacency matrix. A accounts for the underlying topology with $A_{ij} = 1$ if there is a link between nodes i and j and $A_{ij} = 0$, otherwise.

From a methodological standpoint, as the focus of this section, Tanaka et al. (Tanaka et al., 1997a; Tanaka et al., 1997b) analyzed the collective behavior of a set of coupled Kuramoto model with inertia using a mean-field analysis. In terms of stability against perturbations, Menck et al. (Menck et al., 2014) quantified the stability of network coupled oscillators in terms of the basin of attraction of a synchronized state against large perturbations, termed basin stability, and intended to find the correlation between the stability and underlying structures.

In section. 2.1, we introduce the mean-field approximation implemented on the second-order Kuramoto model. In particular, we illustrate the derivation of the second-order Kuramoto model from power grids, explain the basic behavior of the single-node model in Sec. 2.1.1, and introduce the mean-field theoretical framework on the second-order Kuramoto model in Sec. 2.1.3. In section 2.2, we illustrate the basin stability formalism.

2.1 Second-order Kuramoto model

2.1.1 Illustration

To mimic essential properties of the nonlinear dynamics of a population of N interconnected dynamical units in power grids, we consider the a power grid model on coarse scales (Filatrella et al., 2008).

The state of each unit (machine) $i = 1, \dots N$ is determined by its phase angle $\phi_i(t)$ and its velocity $d\phi_i(t)/dt$. Each unit rotates with the same frequency $\Omega = 2\pi \times 50$ Hz or $\Omega = 2\pi \times 60$ Hz, thus

$$\phi_i(t) = \Omega t + \theta_i(t), \tag{2.2}$$

where θ_i indicates the phase difference to the reference phase Ωt.

During the rotation, the dissipated power is given by $P_{\text{diss},i} = K_D(\dot{\phi}_i)^2$, where K_D is a fraction coefficient. The kinetic energy follows $E_{\text{kinetic},i} = I_i\dot{\phi}_i^2/2$ and the accumulated kinetic power is given by $P_{\text{acc},i} = \frac{dE_{\text{kinetic},i}}{dt}$, where I_i is the moment of inertia. If a power flow between machines i and j exists, the power transmission is proportional to the sine of the phase difference, i.e. $\sin(\phi_j - \phi_i)$ and the transmitted power follows $P_{\text{trans},ij} = -P^{\max,ij}\sin(\phi_j - \phi_i)$, where $P^{\max,ij}$ is the maximal capacity of the transmission line. If there is no power flow, $P_{\text{trans},ij} = 0$.

The power source $P_{\text{source},i}$, which is fed into each machine i, has to be met by the sum of the power transmitted within the grid plus the accumulated and dissipated power, i.e., $P_{\text{source},i} = P_{\text{diss},i} + P_{\text{acc},i} + \sum_{j=1}^{N} P_{\text{trans},ij}$. Inserting the expressions of powers into such equation, one gets

$$P_{\text{source},i} = I_i\ddot{\theta}\dot{\phi}_i + K_D(\dot{\phi}_i)^2 - \sum_{j=1}^{N} P^{\max,ij}\sin(\phi_j - \phi_i). \tag{2.3}$$

Via subsutiting Eq. (2.2) into Eq. (2.3) and assuming a small perturbation of the synchronous frequency compared to the reference frequency $\dot{\theta}_i \ll \Omega$, $I_i\ddot{\theta}_i$ and $K_D\dot{\theta}_i^2$ can be neglected compared to $I_i\ddot{\theta}_i\Omega$ and $K_D\Omega^2$, respectively. Eq. (2.3) therein becomes (Filatrella et al., 2008; Witthaut and Timme, 2012; Rohden et al., 2012)

$$I_i\Omega\ddot{\theta}_i = P_{\text{source},i} - K_D\Omega^2 - 2K_D\Omega\dot{\theta}_i + \sum_{j=1}^{N} P^{\max,ij}\sin(\theta_j - \theta_i). \tag{2.4}$$

For the sake of simplicity, provided that the moment of inertia I_i and the line maximal capacity $P^{\max,ij}$ are the same for all elements of the grid, defining $\Omega \equiv (P_{\text{source},i} - K_D\Omega^2)/(I\Omega)$, $\alpha \equiv 2K_D/I$ and $\lambda A_{ij} \equiv P^{\max}/(I\Omega)$, this finally yields the original dynamics Eq. (2.1) (Filatrella et al., 2008; Witthaut and Timme, 2012; Rohden et al., 2012; Ji et al., 2013).

2.1.2 Dynamics of the one-node model

Consider the one-node model, where one node is connected to a grid and, whose dynamics follows

$$\ddot{\theta} = -\alpha\dot{\theta} + \Omega + \lambda\sin(\theta_L - \theta). \tag{2.5}$$

The grid is considered to be infinite in the sense that its state can not be effected by the node's dynamics. Hence as always $\theta_L \equiv 0$. Such model also depicts the governing dynamics of the driven pendulum (Strogatz, 2001), the Josephson junction (Strogatz, 2001), and the one-machine infinite bus system (Chiang, 2011).

The node can either converge to a fixed point or oscillate periodically. Menck et al. (Menck et al., 2014) proposed a way to approximate its oscillating curve. For $\lambda = 0$, the model (2.5) has one stable limit cycle with frequency $\omega(t) = \Omega/\alpha$ and phase $\theta(t) = \omega(t)t + \theta(0)$. For large λ, a similar solution is still fulfilled with the average frequency $\langle\omega\rangle = \int_{t=0}^{T} \omega(t)dt/T \approx \Omega/\alpha$ and $\theta(t) \approx \langle\omega\rangle t + \theta(0)$, where T is a long integrating period. To derive an expression of the instant frequency, they assumed $\omega(t) = \langle\omega\rangle + f(t)$, where $f(t)$ remains to be solved. Inserting this into Eq. (2.5) yields

$$\dot{f} = -\alpha f - \lambda \sin(\langle\omega\rangle t + \theta(0)), \tag{2.6}$$

which has one special solution as follows

$$f(t) = -\frac{\alpha\lambda}{\langle\omega\rangle^2 + \alpha^2}\left(\sin\left(\langle\omega\rangle t + \theta(0)\right) - \frac{\langle\omega\rangle}{\alpha}\cos\left(\langle\omega\rangle t + \theta(0)\right)\right). \tag{2.7}$$

For $\langle\omega\rangle \gg \alpha$ and via inserting $\langle\omega\rangle \approx \Omega/\alpha$ into Eq. (2.7), the instant frequency therein is approximated by

$$\omega(t) \approx \Omega/\alpha + \frac{\alpha\lambda}{\Omega}\cos(\Omega t/\alpha + \theta(0)). \tag{2.8}$$

Eq. (2.8) has a good agreement with numerical results (Menck et al., 2014). Integrating Eq. (2.8) yields (Menck et al., 2014)

$$\theta(t) \approx \Omega t/\alpha + \frac{\alpha^2\lambda}{\Omega^2}\sin\left(\Omega t/\alpha + \theta(0)\right) + \theta(0). \tag{2.9}$$

If $\Omega^2 \gg \alpha^2\lambda$, $\theta \approx \Omega t/\alpha + \theta(0)$ which is consistent with the previous assumption.

For the one-node model, Chiang (Chiang, 2011) considered the following energy function $E(\theta, \omega)$ consisting of kinetic energy $E_k(\omega)$ and potential energy $E_p(\theta)$ functions:

$$E(\theta, \omega) = E_k(\omega) + E_p(\theta), \tag{2.10}$$

where $\omega \equiv \dot{\theta}$, $E_k(\omega) = \frac{\omega^2}{2}$ and $E_p(\theta) = -\Omega\theta - \lambda\cos(\theta)$.

Strogatz (Strogatz, 2001) provided useful guidelines for analyzing the dynamics of the one-node model. Firstly, in the absence of damping and external driving, i.e. $\alpha = 0$ and $\Omega = 0$, by introducing a dimensionless time $\tau = \lambda t$, Eq. (2.5) becomes the

simplest version

$$\frac{d^2\theta}{d\tau^2} = -\sin(\theta). \tag{2.11}$$

Such system has two fixed points within the range of $[0, 2\pi)$. One fixed point $(\theta^*, \omega^*) = (\pi, 0)$ is a saddle. The other is located at $(\theta^*, \omega^*) = (0, 0)$. The origin is a nonlinear center, as the system is reversible and conservative with the energy function $E(\theta, \omega) = \omega^2/2 - \cos(\theta) = \text{constant}$. A local minimal energy is located at the fixed point with $E(0, 0) = -1$. Small obits around the center are small oscillations, called librations. The obits grow with the increases in E until $E = 1$ along with the heteroclinic trajectories linking saddles. With further increases in E, i.e. $E > 1$, the system starts oscillating periodically over or below the heteroclinic trajectories.

Secondly, Strogatz (Strogatz, 2001) added linear damping to this system, i.e. $\alpha > 0$ and $\Omega = 0$. The system therein has one stable fixed point at $(\theta^*, \omega^*) = (0, 0)$ and one saddle $(\theta^*, \omega^*) = (\pi, 0)$. With small damping, librations start converging to the stable fixed point. The energy decreases monotonically along the trajectories with the rate $\frac{dE(\theta,\omega)}{dt} = \frac{d(\omega^2/2 - \lambda\cos(\theta))}{dt} = -\alpha\omega^2$, except for the fixed points with $\omega^* = 0$.

Thirdly, Strogatz (Strogatz, 2001) considered the original system (2.5) with damping as well as external driving, i.e. $\alpha > 0$ and $\Omega > 0$. For notational convenience, one could either set $\lambda = 1$ or introduce a dimensionless time $\tau = \sqrt{\lambda}t$. For $\Omega > 1$, all rotations converge to a unique and stable limit cycle and no fixed points are available. For $\Omega < 1$, two fixed points comprise a saddle and a sink, and they satisfy $\omega^* = 0$ and $\sin(\theta^*) = \Omega$. The linear stability of the fixed points is determined by the Jacobian matrix

$$J = \begin{pmatrix} 0 & 1 \\ -\cos(\theta^*) & -\alpha \end{pmatrix}$$

with two eigenvalues

$$\lambda_{1,2} = \frac{-\alpha \pm \sqrt{\alpha^2 - 4\cos(\theta^*)}}{2}. \tag{2.12}$$

The fixed point with $\cos(\theta^*) = -\sqrt{1 - \Omega^2}$ with $\lambda_1 > 0$ and $\lambda_2 < 0$ is a saddle. The other with $\cos(\theta^*) = \sqrt{1 - \Omega^2}$ is stable due to its real part of both eigenvalues $Re(\lambda_{1,2}) < 0$. Moreover, it is a stable node for $\alpha^2 - 4\sqrt{1 - \Omega^2} > 0$ and a stable spiral, otherwise.

For small α, suppose that we start from $\Omega > 1$ and the system rotates periodically. We slowly decrease Ω and, at some critical values $\Omega_c < 1$, rotations merge with the saddle and are destroyed in a homoclinic bifurcation. Its critical value is determined by

$$\Omega_c = \frac{4\alpha}{\pi}, \tag{2.13}$$

as $\alpha \to 0$ based on the Melnikov's analysis (Strogatz, 2001). Manik et al. (Manik et al., 2014) reproduced such result according to Lyapunov's second method. For large α, we slowly decrease Ω from $\Omega > 1$, rotations are destroyed by the infinite-period bifurcation and fixed points appear. For small α, suppose that we start from a stable fixed point and slowly increase Ω. Two fixed points collide and annihilate each other in a saddle-node bifurcation with $\Omega_c = 1$.

Rohden et al. (Rohden et al., 2012) considered a two-nodes model consisting of one generator ($\Omega_g = \Omega_0$) and one consumer ($\Omega_c = -\Omega_0$). The phase difference $\phi = \theta_g - \theta_c$ follows

$$\ddot{\phi} = -\alpha\dot{\phi} + 2\Omega_0 - 2\lambda \sin(\phi).$$

Its stability diagram follows the same rule as in the one-node model.

2.1.3 Mean-field theory

Tanaka et al. (Tanaka et al., 1997a; Tanaka et al., 1997b) provided the mean-field framework for investigating the hysteretic behavior in the large network size and validated theoretical results with a uniform, bounded intrinsic frequency distribution. The hysteresis exhibits the hysteretic response in each oscillator and is termed *adaption induced* hysteresis. To compare to the case of without inertia, they took the following general form of the second-order Kuramoto model

$$m\ddot{\theta}_i = -\dot{\theta}_i + \Omega_i + \frac{\lambda}{N}\sum_{j=1}^{N} \sin(\theta_j - \theta_i), \tag{2.14}$$

where $m\ddot{\theta}_i$ denotes the inertia of the i-th oscillator.

After a suitable coordinate transformation via replacing the coupling term by the mean-field quantities (r, ψ) with $re^{i\psi} = \frac{1}{N}\sum_j e^{i\theta_j}$, Eq. (2.14) is rewritten as

$$m\ddot{\theta}_i = -\dot{\theta}_i + \Omega_i + \lambda r(t) \sin(\psi(t) - \theta_i). \tag{2.15}$$

The linear stability of the incoherent solution of such model with white noise, inertia and the natural frequency distribution is rigorously analyzed (Acebrón et al., 2000). In the limit of zero noise, Gupta et al. (Gupta et al., 2014) derived the critical threshold λ_c, where the system exhibits the first-order transition from incoherent to coherent states, as follows

$$\frac{1}{\lambda_c} = \frac{\pi g(0)}{2} - \frac{m}{2}\int_{-\infty}^{\infty} \frac{g(\Omega)}{1 + m^2\Omega^2} d\Omega, \tag{2.16}$$

where $g(\Omega)$ is unimodal with width σ. Without inertia, i.e. $m \to 0$, Eq. (2.16) reduces to the exact formula of the onset of collective synchronization of the first-

order Kuramoto model. For Lorentzian $g(\Omega)$, Olmi et al. (Olmi et al., 2014) obtained an explicit formula of the critical coupling strength

$$\lambda_c = 2\sigma(1 + m\sigma), \tag{2.17}$$

which is consistent with the results obtained by Acebron et al. (Acebrón et al., 2000). For a Gaussian distribution and with a rather small m, Olmi et al. (Olmi et al., 2014) derived the first corrective terms

$$\lambda_c = 2\sigma\sqrt{\frac{2}{\pi}}\left\{1 + \sqrt{\frac{2}{\pi}}m\sigma + \frac{2}{\pi}m^2\sigma^2 + \sqrt{\left(\frac{2}{\pi}\right)^3 - \frac{2}{\pi}}m^3\sigma^3\right\} + O(m^4\sigma^4). \tag{2.18}$$

With the increases in m and σ for the Lorentzian distribution as well as the Gaussian distribution, they (Olmi et al., 2014) also verified that the system becomes harder and harder to achieve complete synchronization.

When the natural frequency distribution $g(\Omega)$ is unimodal, symmetric, and has zero mean, the mean phase could be taken as a constant, e.g. $\psi(t) \equiv 0$. In the continuum limit, where $N \to \infty$, the fluctuations of the phase coherence $r(t)$ vanish and $r(t)$ therein is assumed to be constant, e.g. $r(t) \equiv r$. In this case, the system could be considered a set of a one-node model. With respect to parameter values in the stability diagram, one oscillator could be located in the region of the stable limit cycle, the stable fixed point or the region of bistability with the coexistence of such two stable solutions.

Following the classical process of the first-order Kuramoto model, the set of oscillators is splitted into one subgroup of oscillators locked to the mean phase and the other subgroup of drifting oscillators whirling over (or below depending on the sign of Ω) the locked subgroup. Therefore, the overall phase coherence r sums two certain coherence r_{lock} and r_{drift}, contributed by these two subgroups, respectively, i.e.,

$$r = r_{\text{lock}} + r_{\text{drift}}. \tag{2.19}$$

To study the adaption induced hysteresis, two kinds of simulations are considered, by increasing and decreasing adiabatically the coupling strength (Tanaka et al., 1997b; Tanaka et al., 1997a), respectively. (I) When the coupling strength λ increases from a small value, the phase coherence r^{I} persists around a small fluctuation due to the effects of network sizes until a critical coupling strength, denoted by λ_c^{I}. Above λ_c^{I}, the system jumps to a weakly synchronized state. r^I increases with further increases in λ and saturates to a constant for sufficiently large coupling strengths. (D) When the coupling strength λ decreases from a sufficiently large value, the system is initially in the strongly synchronized state and r^{D} remains nearly constant until a critical coupling strength, denoted by λ_c^{D}. Beyond this threshold, the system jumps back to a incoherent state. Hysteretic behaviors therein are observed. Two critical coupling strengths λ_c^{I} and λ_c^{D} are almost the same for small m (e.g. $m = 0.95$) but its difference

enlarges for large m (e.g. $m = 2.0$ or 6.0) (Tanaka et al., 1997a). λ_c^{D} is the same as the first-order Kuramoto model's (Tanaka et al., 1997b). Different dynamics regimes are observed (Tanaka et al., 1997a; Tanaka et al., 1997b), including the incoherent state (IS), the weakly synchronized state (WSS), the strongly synchronized state (SSS), a transition state from WSS to SSS and vice versa.

In the case (I) of increasing λ, all oscillators initially drift around its own natural frequency Ω_i. With increasing λ, oscillators with small natural frequency below the threshold Ω_P, i.e. $|\Omega_i| < \Omega_P$, start being attracted to the locked group. With further increases in λ, Ω_P enlarges, oscillators with large natural frequency become synchronized and the phase coherence r^{I} increases. For sufficiently large coupling, Ω_P exhibits plateaus and $r^{\mathrm{I}} \approx 1$. If the inertia is rather small, i.e. $\frac{1}{\sqrt{m\lambda r^{\mathrm{I}}}} \ll 1$, the homoclinic bifurcation is tangent to the line (2.13), and Tanaka et al. (Tanaka et al., 1997b) obtained the approximation of the threshold Ω_P as $\Omega_P = \frac{4}{\pi}\sqrt{\frac{\lambda r^{\mathrm{I}}}{m}}$. During this process, a secondary synchronization of drifting oscillators is observed for larger m. The phenomenon was confirmed by Olmi et al. (Olmi et al., 2014), where the authors validated the synchronized motions by comparing the evolution of the instantaneous frequency $\omega_i(t) = \dot{\theta}_i$ of the secondary synchronized oscillators and also observed such phenomenon in realistic Italian high-voltage power grid. But the underlying mechanism needs further investigation.

In the case (D) of decreasing λ, initially almost all oscillators are locked to the mean phase ψ if the starting coupling strength λ is large enough, and $r^{\mathrm{D}} \approx 1$. With decreasing λ further, locked oscillators are desynchronized and start whirling when their natural frequency exceeds the threshold Ω_D, i.e. $|\Omega_i| > \Omega_D = \lambda r^{\mathrm{D}}$, where the saddle node bifurcation occurs.

Therefore, given the synchronized boundary Ω_P and Ω_D, the contribution to the locked coherence follows (Tanaka et al., 1997a; Tanaka et al., 1997b; Olmi et al., 2014)

$$r_{\mathrm{lock}}^{\mathrm{I,D}} = \lambda r^{\mathrm{I,D}} \int_{-\theta_{P,D}}^{\theta_{P,D}} \cos^2\theta g(\lambda r^{\mathrm{I,D}} \sin(\theta)) d\theta, \tag{2.20}$$

where $\theta_P = \sin^{-1}(\Omega_P/(\lambda r^{\mathrm{I}}))$ and $\theta_D = \sin^{-1}(\Omega_D/(\lambda r^{\mathrm{D}}))$.

The phase coherence from drifting oscillators takes the same form as in the first-order Kuramoto model (Acebrón et al., 2005) and follows (Tanaka et al., 1997a; Tanaka et al., 1997b; Olmi et al., 2014)

$$r_{\mathrm{drift}}^{\mathrm{I,D}} = \int_{|\Omega|>\Omega_{P,D}} \oint e^{i\theta} \rho_D(\theta;\Omega) g(\Omega) d\theta d\Omega, \tag{2.21}$$

where ρ_D is the density of the drifting oscillators with phase θ given by the frequency Ω. $\rho_D(\theta;\Omega)$ is proportional to $|\omega|^{-1}$, i.e. $\rho_D(\theta;\Omega) = \frac{\hat{\Omega}}{2\pi}|\omega|^{-1}$, where $\hat{\omega}$ is the frequency of the periodical solution of θ (Tanaka et al., 1997b). Via expanding the cosine function by the Bessel functions and the Poicare-Lindstead method (Tanaka et al., 1997b),

Eq. (2.21) can be simplified as

$$r_{\text{drift}}^{\text{I,D}} = \int_{|\Omega|>\Omega_{P,D}} \int_0^{\hat{T}} \cos(\theta(t,\Omega)) g(\Omega) dt d\Omega, \tag{2.22}$$

where $\hat{T} = \frac{2\pi}{\hat{\omega}}$ is the period of the running periodical solution of θ.

Based on this theoretical framework, Tanaka et al. (Tanaka et al., 1997a) studied a general distribution of $g(\Omega)$ with extended tails and solved the self-consistent equations of the order parameter r analytically.

2.2 Basin stability

In the last decades, much research effort has been devoted to explore how the synchronizability of network coupled oscillators depends on network topology (Pecora and Carroll, 1998; Arenas et al., 2008), but from a local perspective, related to the spectral properties of the underlying structure. The seminal work by Wiley, Strogatz and Girvan (Wiley et al., 2006) initiated a new line of research by proposing a new stability approach that is related to the size of the basin of attraction for a synchronous state. Additional, they proposed two questions to be answered: How likely will a network fall into sync, starting from random initial conditions? And how does the likelihood of synchronization depend on the network topology? Alternatively, Menck et al. (Menck and Kurths, 2012; Menck et al., 2013) addressed the first questions differently: How likely a network returns to the synchronous state after random perturbations? Substantially, Menck et al. (Menck et al., 2014) uncovered the correlation between basin stability and the network architecture in the second-order Kuramoto model.

Menck et al. (Menck et al., 2014) quantified the stability of network coupled oscillators in terms of the basin of attraction of a synchronized state against large perturbations, termed basin stability, and intended to find the correlation between the stability and underlying structures.

The traditional linear stability is too local to adequately quantify how stable a state is (Menck et al., 2013). Menck et al. (Menck and Kurths, 2012; Menck et al., 2013) profound a new concept, termed *basin stability*, which quantifies the likelihood that a system will retain a desirable state after even large perturbations. Basin stability is non-local, nonlinear and easily applicable to high-dimensional systems, even with fractal basin boundaries. It is related to the volume of the basin of attraction. Although volumes of basins have been studied before, the concept has not yet been applied on complex networks (Menck and Kurths, 2012; Menck et al., 2013; Menck et al., 2014). Therefore, basin stability is a widely applicable tool.

Menck et al. (Menck and Kurths, 2012; Menck et al., 2014) implemented the novel concept on the second-order Kuramoto model. To quantify how stable a synchronous

state is against large perturbations depending on network topologies, they defined basin stability $\mathcal{BS}_i$ at each node i as (Menck et al., 2014)

$$\mathcal{BS}_i = \int \chi(\theta_i, \omega_i)\rho(\theta_i, \omega_i)d\theta_i d\omega_i, \quad \text{with } \theta_j = \theta_j^* \text{ and } \omega_j = 0 \quad \text{for all } j \neq i \tag{2.23}$$

where $\chi(\theta_i, \omega_i)$ is an indicator function with $\chi(\theta_i, \omega_i) = 1$ if (θ_i, ω_i) belong to the basin of attraction of the synchronous state, and $\chi(\theta_i, \omega_i) = 0$, otherwise. ρ is a perturbation density function with the normalization condition $\int \rho(\theta_i, \omega_i)d\theta_i d\omega_i = 1$. $\theta_j = \theta_j^*$ and $\omega_j = 0$ for all $j \neq i$ indicate that initially all nodes in the synchronous state except i. The value of $\mathcal{BS}_i$ at node i expresses the likelihood that the system returns to the synchronous state after i having been subjected to large perturbations. $\mathcal{BS}_i = 0$ when the node i is unstable, and $\mathcal{BS}_i = 1$ when i is globally stable.

Numerically, basin stability $\mathcal{BS}_i$ is estimated by means of a Monte-Carlo method. More specifically, the system of equations is integrated independently for M_i different initial conditions drawn according to ρ, one can count the number S_i of initial conditions at which the system converges to the synchronous state and calculate basin stability as (Menck et al., 2014)

$$\mathcal{BS}_i = \frac{S_i}{M_i}. \tag{2.24}$$

This is a repeated Bernoulli experiment, and thus the standard error e of basin stability follows (Menck et al., 2014)

$$e = \frac{\sqrt{\mathcal{BS}_i(1 - \mathcal{BS}_i)}}{M_i}. \tag{2.25}$$

e is independent of the system's dimension.

Chapter 3

Low-dimensional behavior

3.1 Introduction

In 2008, Ott and Antonsen (Ott and Antonsen, 2008) introduced an ansatz for studying the behaviour of globally coupled oscillators. The Ott-Antonsen ansatz has been considered to investigate continuously time-dependent collective behavior (Petkoski and Stefanovska, 2012) and for the study of delay heterogeneity (Lee et al., 2009). In addition, such ansatz has enabled to find nonuniversal transitions to synchrony in the model with a phase lag for certain unimodal frequency distributions (Omelchenko and Wolfrum, 2012).

Although these works have provided important contributions to synchronization theory, only oscillators with global coupling have been taken into account (Omelchenko and Wolfrum, 2012; Lai and Porter, 2013; Iatsenko et al., 2013; Lee et al., 2009; Petkoski and Stefanovska, 2012). Thus, a natural extension of these works can investigate how these results change when different coupling schemes are introduced. Barlev et al. (Barlev et al., 2011) studied the dynamics of coupled phase oscillators, but such approach involved integrating N ordinary differential equations. To overcome this limitation, in this report we generalize the Ott-Antonsen ansatz to complex networks in the continuum limit to investigate a time-dependent phase transition to synchronization. We reduce the dimension of the system of equations from N to the number of possible degrees in the network.

The Kuramoto model with inertia has been widely used as shown in Chapter 1. Therefore a theory that investigates the low-dimensional character of such systems giving access to their time-dependent behavior can bring important new insights into the study of the second-order Kuramoto model. We substantially address this problem for what is perhaps the simplest choice of inertia term. In this case, the Fourier series expansion, the key approach of the Ott-Antonsen ansatz, no longer applies directly. Thus, a generalized framework for the second derivative needs to be developed, as already pointed out in recent studies (Sonnenschein et al., 2013; Lai and Porter, 2013). In order to fill this gap, we derive self-consistent equations and seek the time evolution of the order parameter. Comparison of analytical and simulation results shows a good agreement. Our results shed light on the impact of the topology on the global dynamics.

In Sec. 3.2, we obtain the low-dimensional behavior of the first-order Kuramoto model in complex networks. In Sec. 3.3, we investigate the extension of the ansatz to the Kuramoto model with inertia. Sec. 3.4 shows the conclusions.

The findings presented here have been published in (Ji et al., 2014b).

3.2 First-order Kuramoto model

We consider the first-order Kuramoto model on an unweighted and undirected complex network. The state of oscillator i is denoted by its phase $\theta_i (i = 1, 2, \cdots, N)$, and the governing equation of the model (Kuramoto, 1975) is

$$\frac{d\theta_i}{dt} = \Omega_i + \lambda \sum_{j=1}^{N} A_{ij} \sin(\theta_j - \theta_i), \tag{3.1}$$

where Ω_i stands for the natural frequency of oscillator i, which is distributed according to some probability density $g(\Omega)$, λ specifies the homogeneous coupling strength between interconnected nodes, and A_{ij} is the element of the adjacency matrix $\mathbf{A}$, i.e., $A_{ij} = 1$ if nodes i and j are connected or $A_{ij} = 0$, otherwise.

In uncorrelated networks, if N approaches infinity (in thermodynamic limit), the probability of selecting an edge connected to a node with degree k, natural frequency Ω, and phase θ at time t is $kP(k)\rho(k; \Omega, \theta, t)/\langle k \rangle$, where we define $P(k)$ as the degree distribution and $\rho(k; \Omega, \theta, t)$ as the probability distribution function of nodes with degree k that have natural frequency Ω and phase θ at time t and $\langle k \rangle$ the average degree (Ji et al., 2013; Peron and Rodrigues, 2012a; Ichinomiya, 2004).

In complex networks, in order to understand the dynamics of the system, it is natural to use the definition of order parameter r (Ichinomiya, 2004) as

$$re^{i\psi} = \frac{\sum_i k_i e^{i\theta_i}}{\sum_i k_i} \tag{3.2}$$

instead of the definition $re^{i\psi} = \frac{\sum_i e^{i\theta_i}}{N}$, which accounts for the mean-field in the fully connected graph regime.

The magnitude $r \in [0, 1]$ quantifies the phase coherence, while ψ denotes the average phase of the system. In particular, $r \simeq 0$, if the phases are randomly distributed over $[0, 2\pi]$ and all nodes oscillate at its natural frequency. On the other hand, if all oscillators run as a giant component, $r \simeq 1$. The system is known to exhibit a phase transition from the asynchronous state ($r \simeq 0$) to the synchronous one ($r \simeq 1$) at a certain critical value λ_c characterizing the onset of partial synchronization and, for unimodal and symmetric frequency distributions $g(\Omega)$, the transition is continuous. It turns out that for uncorrelated networks, λ_c is given by $\lambda_c = \frac{2}{\pi g(\Omega) \lambda_{\max}}$ (Restrepo et al., 2005), where $\lambda_{\max}$ is the maximal eigenvalue of the adjacency matrix.

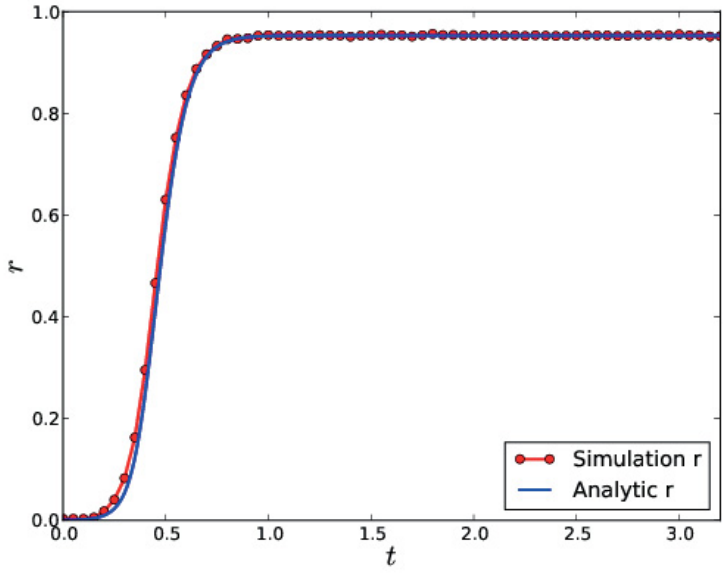

Figure 3.1: The order parameter as a function of time. Numerical simulations of the first-order Kuramoto model [Eq. (3.1)] are conducted on a scale-free network with $N = 10000$, $P(k) \propto k^{-3}$ and $k \geq 5$. The coupling strength $\lambda = 2.5$ and θ are randomly selected from $-\pi$ to π at $t = 0$.

To characterize the macroscopic behavior of the oscillators, in the continuum limit, we consider the order parameter

$$\begin{aligned} re^{i\psi} &= \int dk \int d\Omega \int d\theta P(k) k \rho(k;\Omega,\theta,t) e^{i\theta} / \int dk P(k) k \\ &= \int dk P(k) k r_k e^{i\psi_k} / \int dk P(k) k, \end{aligned} \tag{3.3}$$

where r_k quantifies the local synchrony of oscillators with degree k

$$r_k e^{i\psi_k} = \int d\Omega \int d\theta \rho(k;\Omega,\theta,t) e^{i\theta}. \tag{3.4}$$

For simplicity, we assume that the natural frequencies Ω_i are distributed according to an unimodal and symmetric Cauchy-Lorentz distribution ($g(\Omega)$) with zero mean. We set $\psi = \psi_k = 0$ without loss of generality (Strogatz, 2000). The coupling term in Eq. (3.1) can be written as $\sum_{j=1}^{N} A_{ij} \sin(\theta_j - \theta_i) = k_i r \mathrm{Im}[e^{\psi - \theta_i}]$ (Ichinomiya, 2004; Peron and Rodrigues, 2012a; Ji et al., 2013). Thus the governing Eq. (3.1) can be rewritten as

$$\frac{d\theta}{dt} = \Omega + \lambda k r \frac{e^{-i\theta} - e^{i\theta}}{2i}, \tag{3.5}$$

which shows that the oscillators are coupled via the mean-field order parameter r. The restoring force tends to bring each oscillator towards equilibrium and the amount of forcing is proportional to its degree k.

The evolution of $\rho(k;\Omega,\theta,t)$ is governed by the continuity equation, i.e., $\frac{\partial\rho}{\partial t}+\frac{\partial\rho v}{\partial\theta}=0$, where $v(k;\Omega,\theta,t)=\frac{d\theta}{dt}$. We use the Ott-Antonsen ansatz (Ott and Antonsen, 2008) and expand the density function in a Fourier series, i.e.,

$$\rho(k;\Omega,\theta,t)=\frac{g(\Omega)}{2\pi}\left\{1+\left[\sum_{n=1}^{\infty}[a(k;\Omega,t)]^n e^{in\theta}+c.c.\right]\right\}. \tag{3.6}$$

where $c.c$ stands for the complex conjugate. Substituting the expansion into Eqs. (3.4) and in the continuity equation, we get that $r_k=a(k)$ and r_k evolve according to

$$\frac{dr_k}{dt}=-r_k+\frac{Kkr}{2}(1-r_k^2)\ \text{ for } k\in[k_{\min},k_{\max}] \tag{3.7}$$

where $k_{\min}$ and $k_{\max}$ are the minimum and the maximum degree, respectively. This method works efficiently compared to the reference (Barlev et al., 2011) especially when the power law behavior has some cutoff (Del Genio et al., 2011). $a(k)$ therein allows a clear physical interpretation as measuring the internal synchrony of the nodes with the same degree k. The global order parameter r is a sum of different r_k multiplied by their degree and degree distribution (see Eq. (3.3)).

To verify the accuracy of the time evolution of the order parameter r_k (see Eq. (3.7)), we compare the time evolution of the order parameter r with numerical simulations. Eqs. (3.7) and (3.13) are solved by a 4^{th} order Runge-Kutta method with time step $h=0.01$ and with the Cauchy-Lorentz distribution $g(\Omega)=\frac{1}{\pi(1+\Omega^2)}$. Fig. 3.1 shows the results. Initially, the values of oscillators are selected at random from π to $-\pi$, which implies that the initial value of each $r_k(0)$ tends to zero. In our simulations, we set $r_k(0)=0.001$. As we can see in Fig. 3.1, the results obtained through the solution of the reduced system in Eq. (3.7) are in good agreement with the numerical simulations.

3.3 Kuramoto model with inertia

The analysis above shows the remarkable usefulness of the Ott-Antonsen ansatz of the first-order Kuramoto model in complex networks, but what happens when we consider the Kuramoto model with inertia? The simplest and most straightforward way is to include one unity inertia term. This leads to the mean-field character of the second-order Kuramoto model (Ji et al., 2013; Strogatz, 2014; Acebrón et al., 2005; Dörfler et al., 2013)

$$\frac{d^2\theta_i}{dt^2}=-\frac{d\theta_i}{dt}+\Omega_i+\lambda kr\sin(-\theta_i), \tag{3.8}$$

where k varies from the minimal to the maximal degree.

As shown in Eq. (3.6), the main idea of the Ott-Antonsen ansatz is to expand the probability density $\rho(k;\Omega,\theta,t)$ in a Fourier series in θ. For the Kuramoto model with inertia, the probability density $\rho(k;\Omega,\theta,\dot{\theta},t)$ is also a function of the additional term $\dot{\theta}$. As $\dot{\theta}$ varies from $-\infty$ to ∞, it is not possible to follow the same procedure to derive the nonlinear evolution of the order parameter r. Due to the existence of the inertia term and the bistable area of the stability diagram (Strogatz, 2014), we rewrite Eq. (3.7) with two functions $\Lambda(\lambda k)$ and $f(\lambda k, r) \equiv a(\lambda k)^b r^c$ and get

$$\frac{dr_k}{dt} = -r_k + \Lambda(\lambda k)\frac{r(1-r_k^2)}{2} + f(\lambda k, r_k), \tag{3.9}$$

where $\Lambda(\lambda k)$ indicates the effective coupling strength and a, b and c are constant. $f(\lambda k, r)$ is a high-order term and is used to adjust the stationary solution. For the Kuramoto model without inertia, we get $\Lambda(\lambda k) = \lambda k$ and $a = 0$.

In order to solve Eq. (3.9), we first investigate the nonlinear dynamics on fully connected networks. In this case, we normalize the coupling strength from λN to λ. For the sake of convenience, we change the time scale to $\tau = \sqrt{\lambda r}t$, which yields

$$\frac{d^2\theta_i}{d\tau^2} = -\beta\frac{d\theta_i}{d\tau} + I_i + \sin(-\theta_i), \tag{3.10}$$

where $\beta \equiv 1/\sqrt{\lambda r}$ and $I_i \equiv \Omega_i/(\lambda r)$. Thus β is identical for all oscillators and the diversity of I_i is due to its natural frequency. According to the parameter space (Ji et al., 2013; Strogatz, 2014), nodes are divided into three groups. Melnikov's method (Guckenheimer and Holmes, 1983) is used to show that oscillators are within a stable fixed point area as $\beta \to 0$ and $I \leq 4\beta/\pi$; only limit-cycle oscillators exist for $I > 1$; limit cycles and stable fixed points coexist otherwise.

Let us first investigate the stationary states of phases θ and $\dot{\theta}$ in terms of the natural frequencies Ω separately. In Fig. 3.2, every single point represents the state of one oscillator at time T ($T >> 1$) using simulations with $N = 10000$ nodes and degree $\lambda = 10$. It is interesting to find that instead of three different regions mentioned above, the oscillators fall into either of the following two groups. (i) If the natural frequencies of nodes are within the boundary of the phase synchronization regime $[\Omega_{\text{lower}}, \Omega_{\text{upper}}] \equiv [-4\sqrt{\lambda r}/\pi, 4\sqrt{\lambda r}/\pi]$ which is the same as the above stable fixed points area, these nodes converge to fixed points and the stationary state of phases are functions of Ω, which are equal to $\arcsin(\Omega/(\lambda r))$. This boundary is smaller than that of the Kuramoto model, in which oscillators are in the locked state for all $|\Omega| \leq \lambda r$ (Strogatz, 2000). (ii) In contrast, the oscillators with $|\Omega| > 4\sqrt{\lambda r}/\pi$ are drift. Thus, in networks, instead of three different areas of single pendulum model, only two distinct areas could exist: fixed point and limit cycle. Nodes with the same natural frequency are either converging to single fixed points or oscillating periodically; and nodes always return to previous states even after large perturbations.

To investigate how the phase synchronization boundary changes with different coupling strengths, we project the Fig. 3.2 on the I-β parameter space and color the oscillators according to their stationary states in the parameter space. A comparison

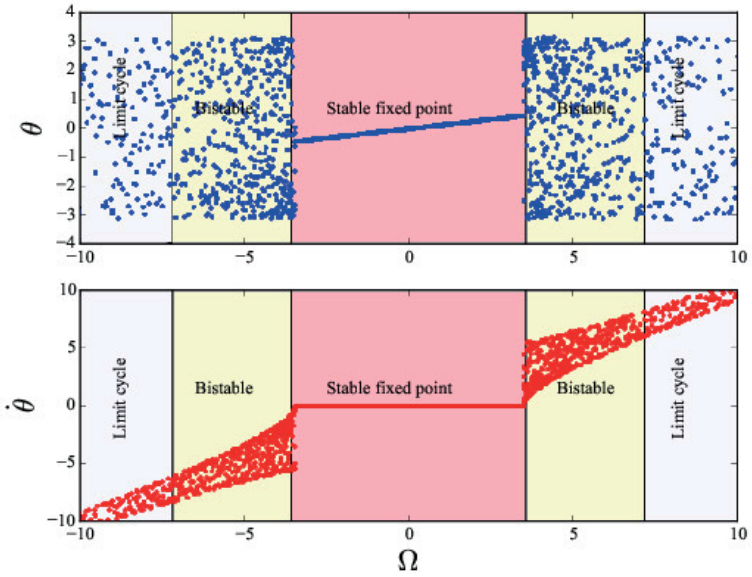

Figure 3.2: Phases θ and frequencies $\dot{\theta}$ vs natural frequencies Ω, which shows that phase-locked oscillators only exist in red area but not in the yellow area. The read area indicates parameter combination of stable fixed point. Stable fixed points and limit cycles coexist in the yellow area. The white area represents the existence of limit cycles. The stationary value of the order parameter r could be calculated by numerically integrating the second-order Kuramoto model (3.8) or Eq. (3.12). Thus nodes with natural frequencies between $[-4\sqrt{\lambda r}/\pi, 4\sqrt{\lambda r}/\pi] = [-3.57, 3.57]$ are synchronized. The boundary of bistable region are specified by $|\Omega|$ within $[4\sqrt{\lambda r}/\pi, \lambda r] = [3.57, 7.18]$.

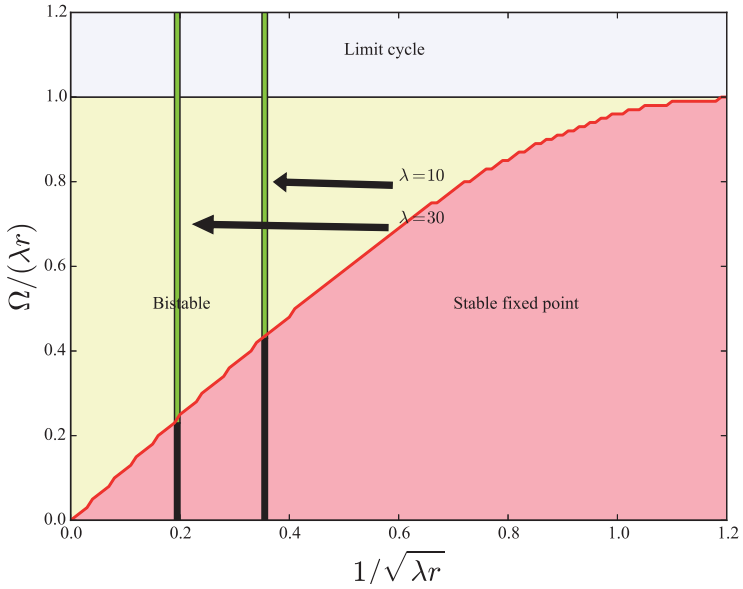

Figure 3.3: The definitions of three shaded areas are the same as that in Fig. 3.2 using the second-order Kuramoto model (3.8). Two boundaries are compared between coupling strengths 10 and 30. If oscillators are in locked state with black color and with Chartreuse color otherwise. Increasing the coupling strength λ further, the vertical line moves to the left.

between the dynamics with average degree 10 and that with 30 is shown in Fig. 3.3. We can see that oscillators with the same coupling share the same β axis and the diversity of I is due to the distribution of the natural frequencies Ω. All synchronized nodes are inside the synchronized area, which is at the right side of the line $I = 4\beta/\pi$.

Therefore, after substituting the boundaries of the synchronized natural frequencies $[\Omega_{\text{lower}}, \Omega_{\text{upper}}]$ and the Cauchy-Lorentz distribution into the definition of the order parameter r,

$$r = \int_{\Omega_{\text{lower}}}^{\Omega_{\text{upper}}} \cos(\theta_s) g(\Omega) d\Omega \,, \tag{3.11}$$

where θ_s denotes the synchronized oscillator $\sin(\theta_s) = I$. Performing some mathematical manipulations, we get

$$r = \frac{2}{\pi\lambda r}\left[\sqrt{1+(\lambda r)^2}\arctan\left(\frac{4\sqrt{\lambda r+(\lambda r)^3}}{\sqrt{(\pi\lambda r)^2-16\lambda r}}\right) - \arcsin\left(\frac{4}{\pi\sqrt{\lambda r}}\right)\right]. \tag{3.12}$$

Due to the difference of boundaries between the first-order Kuramoto model (proportional to λ) and the second-order Kuramoto model (proportional to $4\sqrt{\lambda}/\pi$),

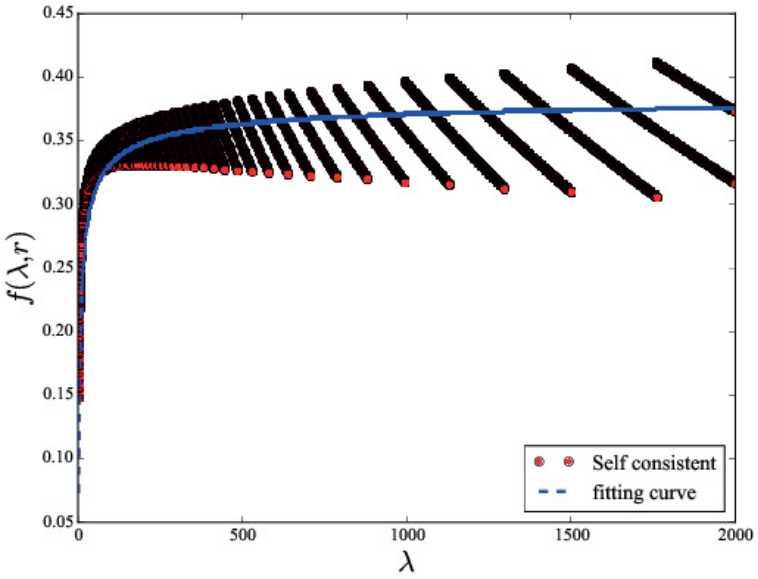

Figure 3.4: $f(\lambda, r)$ as a function of stationary solution of self-consistent equation colored in red and the fitting curve colored in blue.

we set $\Lambda(\lambda) = 4\sqrt{\lambda}/\pi$. When $\dot{r} = 0$,

$$f(\lambda, r) = r - 4\sqrt{\lambda}r(1 - r^2)/(2\pi), \tag{3.13}$$

and this stationary solution should be met by the self-consistent Eq. (3.12). Here, we use numerical methods to calculate the values of a, b and c. As shown in Fig. 3.4, after substituting the stationary solutions λ and r of Eq. (3.12) into Eq. (3.13), $f(\lambda, r)$ is colored in red and we get the values $a = 0.389$, $b = 1/4$ and $c = 3$. When r is small, $f(\lambda, r)$ is close to 0 and cannot influence the time evolution of the order parameter $r(t)$, or vary the stationary solution, otherwise.

Let us consider again the nonlinear evolution of the order parameter r in complex networks. From the above analysis, we get that $\Lambda(\lambda k) = 4\sqrt{\lambda k}/\pi$. To check the validity of this assumption, we compare the stationary solution with simulation results in Fig. 3.5. The theoretical predictions (green lines derived from Eq. (3.9) with effective coupling and $f(\lambda k, r)$) are in agreement with red lines of numerical simulations.

The nonlinear evolution of $r(t)$ is illustrated in Fig. 3.6, for a selection of coupling strengths λ. Initial values of θ_i and $\dot{\theta}_i$ are the same as in Fig. 3.5. For the order parameter formulation the initial value of r is set to a small value ($r(0) \lll 1$). The r formulation of Eq. (3.9) does not only reproduce the stationary states in Fig. 3.5, but also matches the transition to synchrony. The analytic results and simulation results are in good agreement.

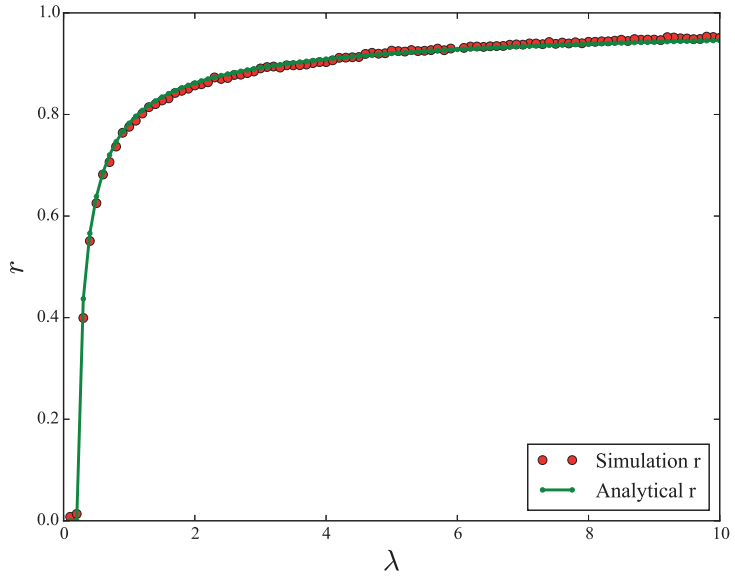

Figure 3.5: Order parameter r vs coupling strengths λ in the second-order Kuramoto model (3.8) in scale-free networks. The red curves indicate the results from simulations on the same network as in fig. 3.1. For each coupling, initial values of θ randomly select from $[-\pi, \pi]$ and we set $\dot{\theta} = 0$. The green dots shows analytic prediction of the stationary $r(t)$ based on the self-consistent Eq. (3.9).

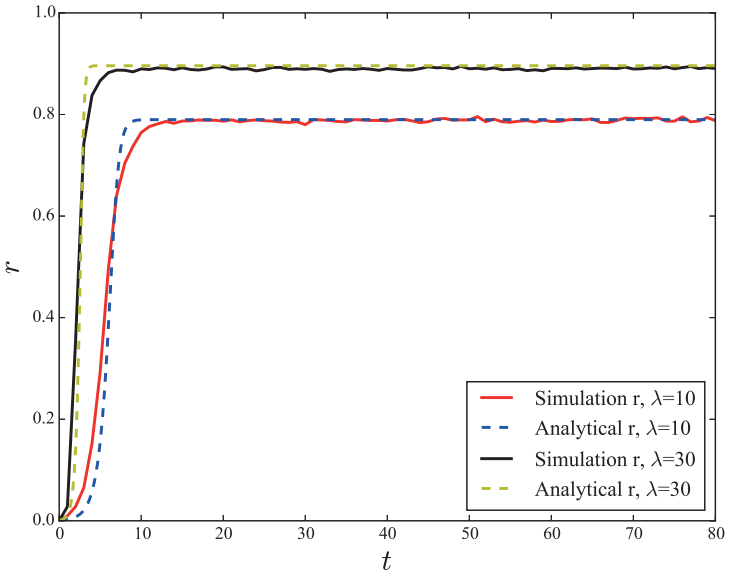

Figure 3.6: Order parameter $r(t)$ vs time t in the second-order Kuramoto model (3.8) in scale-free networks. The simulations are conducted on the same network and the coupling strength $\lambda = 1$ and $\lambda = 3$. Blue and yellow dots are analytic results got from Eq. (3.9). In simulations, initial values of θ are randomly selected from $-\pi$ to π and that of $\dot{\theta}$ close to 0.

3.4 Conclusions

In conclusion, we proposed a generalization for the Ott-Antonsen ansatz to complex networks with a Cauchy-Lorentz distribution of the natural frequency for the Kuramoto model. Compared to the ensemble approach (Barlev et al., 2011), the dimension of ordinary differential equations was reduced from N to the number of possible degrees in the network. We have investigated the collective dynamics of the Kuramoto model with inertia and found the synchronization boundary is $\left[-4\sqrt{\lambda r}/\pi, 4\sqrt{\lambda r}/\pi\right]$ instead of $[-\lambda r, \lambda r]$ as in the Kurmoto model without inertia. Based on these results, we analytically derived self-consistent equations for the order parameter and nonlinear time-dependent order parameter. The agreement between the analytical and simulation results is excellent.

Chapter 4

Cluster explosive synchronization in complex networks

4.1 Introduction

Synchronization plays a prominent role in science, nature, social life, and engineering (Pikovsky et al., 2003; Strogatz, 2004; Arenas et al., 2008). In recent years, much research has been devoted to investigate the effects of network topology on the emergence of synchronization (Arenas et al., 2008). For instance, the Kuramoto oscillators undergo a second-order phase transition to synchronization and the onset of synchronization is determined by the largest eigenvalue of the adjacency matrix (Restrepo et al., 2005).

Until 2011, only continuous synchronization transitions were known to occur in networks of first-order Kuramoto oscillators (Arenas et al., 2008). However, Gómez-Gardenez et al. (Gómez-Gardenes et al., 2011) reported the first observation of discontinuous phase synchronization transitions in scale-free networks, triggering further works on the subject (Leyva et al., 2012; Peron and Rodrigues, 2012b; Liu et al., 2013; Zhang et al., 2013; Su et al., 2013; Zou et al., 2014; Skardal et al., 2013; Skardal and Arenas, 2014; Sonnenschein et al., 2013). Gómez-Gardenez et al. (Gómez-Gardenes et al., 2011) considered a new kind of interplay between the connectivity pattern and the dynamics. More specifically, the authors considered the natural frequencies of the oscillators to be positively correlated with the degree distribution of the network by assigning to each node its own degree as its natural frequency, rather than drawing it from a given symmetric distribution independent of network structure, as performed in previous works (Arenas et al., 2008).

The phenomenon of explosive synchronization was proved to be an effect exclusively due to the microscopic correlation between the network topology and the intrinsic dynamics of each oscillator. Abrupt phase transitions were also previously observed in other dynamical processes in complex networks, such as in the context of explosive percolation in random (Achlioptas et al., 2009) and scale-free (Cho et al., 2009; Radicchi and Fortunato, 2009) networks. Similar to explosive synchronization, the explosive percolation has also a dynamical constraint related to the connectivity patterns, which is called the Achlioptas process (Achlioptas et al., 2009). However, Costa et al. (Costa et al., 2010) considered a representative model and demonstrated

that the explosive percolation transition is actually a continuous, second-order phase transition with a uniquely small critical exponent of the giant cluster size.

Relevant to model several physical systems (Rohden et al., 2012; Acebrón and Spigler, 1998; Dörfler and Bullo, 2012; Trees et al., 2005), the second-order Kuramoto model has also been investigated under the constraint of correlation between the natural frequency and the degree distribution. Recently, we studied analytically and numerically how the inclusion of an inertia term in the second-order Kuramoto model influences the network dynamics (Ji et al., 2013). We observed a discontinuous synchronization transition as in the case of the second-order Kuramoto model in a fully connected graph with unimodal symmetric frequency distributions (Acebrón and Spigler, 1998). However, differently from that observed in (Gómez-Gardenes et al., 2011), where the authors found that nodes in scale-free networks join the synchronous component abruptly at the same coupling strength, we verified that nodes perform a cascade of transitions toward the synchronous state grouped into clusters consisting of nodes with the same degree. We call this phenomenon cluster explosive synchronization (CES).

It is important to remark that different kinds of cluster-like synchronization transitions have been widely studied in the context of network theory in which patterns or sets of synchronized elements emerge (Pecora et al., 2014; Zhou and Kurths, 2006), when ensembles of coupled oscillators are nonidentical (Skardal et al., 2011) or under the influence of noise (Lai and Porter, 2013) or delay (DHuys et al., 2008). Eigenvalue decomposition can also be applied to analyze clusters of synchronized oscillators (Allefeld et al., 2007). Moreover, recent investigations on cluster synchronization have revealed the interplay of the symmetry in the synchronization patterns (Pecora et al., 2014; Nicosia et al., 2013; DHuys et al., 2008). Here, the term "cluster" is redefined and nodes with the same degree are considered to pertain to the same cluster, in contrast to the common definition of a cluster of nodes consisting of oscillators with a common phase (Skardal et al., 2011). Our definition is based on the dynamical behavior observed in the system composed of second-order Kuramoto oscillators whose natural frequency is correlated with the network structure (Ji et al., 2013).

The early works on explosive synchronization (e.g. (Coutinho et al., 2013; Leyva et al., 2012; Peron and Rodrigues, 2012a)) suggested that the correlation between frequency and degree distributions is the only condition required for the emergence of a discontinuous synchronization transition in scale-free networks. However, subsequent papers have shown that different criteria to set the frequency mismatch between the oscillators (Zhu et al., 2013), the presence of time-delay (Peron and Rodrigues, 2012b), non-vanishing degree-degree correlation (Liu et al., 2013; Zhu et al., 2013; Li et al., 2013) or the inclusion of noise (Sonnenschein and Schimansky-Geier, 2013) can dramatically change the type of the phase transitions, even in the regime of fully connected graphs (Leyva et al., 2013; Zhu et al., 2013).

In the case of degree-degree correlation, Li et al. (Li et al., 2013) verified that assortative scale-free networks no longer undergo a discontinuous transition, even if the network presents a positive correlation between structural and dynamical properties. This behavior was also observed in the synchronization of FitzHugh-

Nagumo (FHN) oscillators coupled in scale-free networks under the constraint of correlating frequencies and degrees (Chen et al., 2013). Furthermore, Zhu et al. (Zhu et al., 2013) found that discontinuous transitions only emerge in networks subjected simultaneously to negative degree-degree and frequency-frequency correlations. Effects of degree-degree correlation on general network synchronization phenomena were also analyzed in literature (cf. (Sorrentino et al., 2007; Di Bernardo et al., 2007; Chavez et al., 2006) for studies in the context of the master stability function formalism). For instance, Bernardo et al. (Di Bernardo et al., 2007) studied scale-free networks of identical Rössler oscillators and showed that disassortative mixing enhances network synchronization, when compared with uncorrelated networks (Di Bernardo et al., 2007). On the other hand, regarding the synchronization of weighted networks, assortative mixing can enhance synchronization, depending on the weighting procedure (Chavez et al., 2006).

All these works considered only the first-order Kuramoto model. The influence of network structure on the emergence of explosive synchronization in the second-order Kuramoto model proposed in (Ji et al., 2013) has not been addressed yet, since only uncorrelated networks have been considered (Ji et al., 2013; Ji et al., 2014a). Among important network properties, the degree-degree correlation is observed in several complex networks (Newman, 2003; Costa et al., 2010; Newman, 2002) and it plays a fundamental role in many dynamical processes, such as epidemic spreading and synchronization (Barrat et al., 2008). For example, the degree-degree correlation can change the type of phase transitions of the first-order Kuramoto model with a positive correlation between frequency and degree distributions (Zhu et al., 2013; Li et al., 2013). In this way, since the frequency mismatch between oscillators has been shown to play a crucial role in the emergence of abrupt transitions in the first-order Kuramoto model, it is natural to ask about the effects of degree-degree correlations on the overall dynamics in models with inertia.

Here, we extend the previous findings presented in (Gómez-Gardenes et al., 2011). More specifically, we analyze the parameter space for both branches in the hysteretic synchronization diagram, showing how the transition from a stable limit cycle to stable fixed points takes place as a function of the node degree and coupling strength. Furthermore, we also show that the critical coupling strength for the onset of synchronization, considering the adiabatic increasing of the coupling strength, decreases as a function of the minimum degree of the network. In addition, considering the same increase of the coupling strength, we show that the onset of synchronization decreases when the exponent of power-law degree distribution is increased. However, the onset of synchronization is weakly affected by the exponent of the power-law degree distribution when the coupling strength is decreased adiabatically.

Moreover, in order to compare with different topologies, we extend the results for Watts-Strogatz networks by tuning a single rewiring parameter $p \in [0, 1]$. A first-order phase transition appears for small p, while for large p, the first-order transition is not obvious. If the transition behavior to synchronization is obtained from the relaxation time, the time monotonically increases with p, which is a counter-intuitive result compared to (Hong et al., 2002).

To address the question of how robust discontinuous transitions are against degree-frequency correlations, we include an additional quenched disorder on the natural frequencies. More precisely, we show that the phase coherence decreases, contributing to greatly increasing the irreversibility of the phase transition.

Finally, we investigate the effect of assortative mixing on phase transitions. We find that the synchronization diagrams have a strong dependence on the network assortativity, but in a different fashion compared to the first-order model (Li et al., 2013). In fact, for negative and positive assortativity values, the synchronization is observed to be discontinuous, depending on the damping coefficient. Moreover, the upper branch in the synchronization diagrams associated to the case in which the coupling is decreased is barely affected by different assortativity values, again in contrast with the first-order Kuramoto model (Sendiña-Nadal et al., 2015; Chen et al., 2013; Li et al., 2013; Zhu et al., 2013; Zhang et al., 2013; Su et al., 2013; Liu et al., 2013). In other words, we show here that one is able to control the hysteretic behaviour of the second-order Kuramoto model by tuning the network properties, the phenomenon that was not investigated before. In order to compare with different choices of frequencies distributions, we also investigate the dynamics of damped Kuramoto oscillators in assortative networks using unimodal and even distributions, without being correlated with the local topology. Similarly, as in the case of frequencies proportional to degrees, we again observe very similar behavior for the onset of synchronization over networks with different degree-degree correlations.

This chapter is organized as follows: In section 4.2 we define the second-order Kuramoto model with correlation between the frequency and degree distributions in uncorrelated networks. In particular, Sec. 4.2.1 is devoted to the derivation of the self-consistent equations to calculate the order parameter as a function of the coupling strength in order to determine the synchronized boundaries in Sec. 4.2.2. In Sec. 4.2.3 and Sec. 4.2.4, we present our analytical and numerical results on scale-free networks and Watts-Strogatz networks, respectively. In Sec. 4.2.5, we investigate the influence of quenched disorder. In section 4.3, we study the second-order Kuramoto model in networks with degree-degree correlations, i.e., non-vanishing assortativity. Our final conclusions are shown in Sec. 4.4.

Some of the findings presented here have been published in (Ji et al., 2013; Ji et al., 2014a; Peron et al., 2015).

4.2 Mean-field theory

The second-order Kuramoto model consists of a population of N coupled oscillators whose dynamics are governed by phase equations of the following universal form (2.1). In order to get analytical insights on how the topology effects the dynamics, we assume that the natural frequency Ω_i of a node i is proportional to its degree according to

$$\Omega_i = D(k_i - \langle k \rangle), \tag{4.1}$$

where D is the strength of the connection between the natural frequency and degree. In analogy with power grid networks modeled by the second-order Kuramoto model, the choice of Ω_i as in Eq. (4.1) assumes that in scale-free topologies, a high number of nodes play the role of consumers (nodes with $k_i < \langle k \rangle$) and nodes with high degrees play the role of power producers (nodes with $k_i > \langle k \rangle$). Note that the relation $\sum_j \Omega_j = 0$ is satisfied, which means that the total consumed power ($\Omega_i < 0$) is equivalent to the total generated power ($\Omega_i > 0$).

Substituting Eq. (4.1) in Eq. (2.1), we have (Ji et al., 2013; Ji et al., 2014a)

$$\frac{d^2\theta_i}{dt^2} = -\alpha \frac{d\theta_i}{dt} + D(k_i - \langle k \rangle) + \lambda \sum_{j=1}^{N} A_{ij} \sin(\theta_j - \theta_i). \tag{4.2}$$

In this case, all oscillators try to rotate independently at their own natural frequencies, while the coupling λ tends to synchronize them to a common phase. The local connection between oscillators is defined by the adjacency matrix $\mathbf{A}$.

To study the system analytically in the continuum limit, we define $\rho(\theta, t; k)$ as the density of oscillators with phase θ at time t, for a given degree k, which is normalized as

$$\int_0^{2\pi} \rho(\theta, t; k) d\theta = 1. \tag{4.3}$$

In uncorrelated complex networks, the approximation $A_{ij} = k_i k_j / (N \langle k \rangle)$ is made and a randomly selected edge connects to a node with degree k and phase θ at time t with the probability $kP(k)\rho(\theta, t; k)/\langle k \rangle$, where $P(k)$ is the degree distribution and $\langle k \rangle$ is the average degree. The coupling term at the right-hand side of Eq. (4.2) is rewritten accordingly, i.e. $\sum_{j=1}^{N} A_{ij} \sin(\theta_j - \theta_i) = \sum_{j=1}^{N} k_i k_j \sin(\theta_j - \theta_i)/(N \langle k \rangle)$, which in the continuum limit takes the form $k \int\int P(k') k' \rho(\theta', t; k') \sin(\theta' - \theta) dk' d\theta' / \langle k \rangle$. Thus, the continuum version of Eq. (4.2) is given by

$$\frac{d^2\theta}{dt^2} = -\alpha \frac{d\theta}{dt} + D(k - \langle k \rangle) + \frac{\lambda k}{\langle k \rangle} \int\int k' P(k') \rho(\theta', t; k') \sin(\theta' - \theta) d\theta' dk'. \tag{4.4}$$

In order to visualize the dynamics of the phases, it is natural to follow (Restrepo et al., 2005; Ichinomiya, 2004) and define the order parameter r as $re^{i\psi(t)} = \sum_i k_i e^{i\theta_i(t)} / \sum_i k_i$, where k_i is the degree of the node i and ψ is the average phase. This order parameter is different from $re^{i\psi(t)} = \sum_i e^{i\theta_i(t)}/N$, which accounts for the mean-field in fully-connected graphs (Kuramoto, 2003).

The order parameter r quantifies the phase coherence. For instance, if the initial values of θ and $\dot{\theta}$ are randomly drawn from a uniform distribution and each oscillator rotates at its intrinsic frequency, then $r \approx 0$. On the other hand, if the oscillators act as a giant synchronous component, $r \approx 1$.

In the continuum limit, the order parameter r can be expressed as

$$re^{i\psi} = \frac{1}{\langle k \rangle} \int\int P(k) k \rho(\theta, t; k) e^{i\theta(t)} d\theta dk. \tag{4.5}$$

Seeking to rewrite the continuum version in terms of the mean-field quantities r and ψ, we multiply both sides of Eq. (4.5) by $e^{-i\theta}$, take the imaginary part, and we include it in Eq. (4.4), obtaining

$$\ddot{\theta} = -\alpha\dot{\theta} + D(k - \langle k\rangle) + k\lambda r \sin(\psi - \theta), \tag{4.6}$$

which is the same equation that describes the motion of a damped driven pendulum.

In the mean-field approach, each oscillator appears to be uncoupled from each other, and they interact with other oscillators only through the mean-field quantities r and ψ. The phase θ is pulled towards the mean-phase ψ. In the case of positive correlation between frequencies and degree, we cannot set ψ as constant, since the frequency distribution is not necessarily symmetric.

To derive sufficient conditions for synchronization, we choose the reference frame that rotates with the average phase ψ of the system, i.e., we define $\phi(t) = \theta(t) - \psi(t)$. If $\dot{\phi}(t) = 0$, the oscillator is synchronized with the mean field. Defining $C(\lambda r) \equiv (\ddot{\psi} + \alpha\dot{\psi})/D$ and substituting the new variable $\phi(t)$ in the mean-field equation (4.6), we obtain (Ji et al., 2013)

$$\ddot{\phi} = -\alpha\dot{\phi} + D[k - \langle k\rangle - C(\lambda r)] - k\lambda r \sin\phi. \tag{4.7}$$

4.2.1 Order Parameter

The solutions of Eq. (4.7) exhibit two types of long-term behavior, depending on the size of natural frequency $D(k - \langle k\rangle - C(\lambda r))$ relative to $k\lambda r$. To obtain sufficient conditions for the existence of the synchronous solution of Eq. (4.7), we derive the self-consistent equation for the order parameter r, which can be written as the sum of the contribution r_{lock} due to the oscillators that are phase-locked to the mean-field and the contribution of non-locked drift oscillators r_{drift}, i.e., $r = r_{\text{lock}} + r_{\text{drift}}$ (Tanaka et al., 1997a) (see section 2.1.3).

Locked order parameter

Let us assume that all locked oscillators have a degree k in the range $k \in [k_1, k_2]$. These oscillators are characterized by $\dot{\phi} = \ddot{\phi} = 0$ and approach a stable fixed point defined implicitly by $\phi = \arcsin\left(\frac{|D(k-\langle k\rangle - C(\lambda r))|}{k\lambda r}\right)$, which is a k-dependent constant phase. Correspondingly, $\rho(\phi, t; k)$ is a time-independent single-peaked distribution and

$$\rho(\phi; k) = \delta\left[\phi - \arcsin\left(\frac{D\left(k - \langle k\rangle - C(\lambda r)\right)}{k\lambda r}\right)\right] \text{ for } k \in [k_1, k_2]\,, \tag{4.8}$$

where δ is the Dirac delta function. Therefore, the contribution of the locked oscillators is expressed as

$$r_{\text{lock}} = \frac{1}{\langle k\rangle}\int_{k_1}^{k_2}\int_0^{2\pi} P(k) k e^{i\phi(t)}\delta\left[\phi - \arcsin\left(\frac{D(k - \langle k\rangle - C(\lambda r))}{k\lambda r}\right)\right] d\phi dk,$$

(4.9)

whose real part yields

$$r_{\text{lock}} = \frac{1}{\langle k \rangle} \int_{k_1}^{k_2} kP(k) \sqrt{1 - \left(\frac{D\left(k - \langle k \rangle - C(\lambda r)\right)}{k\lambda r} \right)^2} \, dk. \tag{4.10}$$

We consider first a scale-free network with a degree distribution given by $P(k) = A(\gamma)k^{-\gamma}$, where $A(\gamma)$ is the normalization factor and $\gamma = 3$. Substituting the degree distribution $P(k)$ and applying the variable transformation $x(k) = D(k - \langle k \rangle - C(\lambda r))/\lambda k r$, we obtain the following implicit equation for the contribution of the locked oscillators

$$\begin{aligned} r_{\text{lock}} =& \frac{A(\gamma)}{2D\langle k \rangle} \left[\left(x(k_2)\sqrt{1 - x^2(k_2)} \right) + \arcsin x(k_2) \right. \\ & \left. - \left(x(k_1)\sqrt{1 - x^2(k_1)} + \arcsin x(k_2) \right) \right]. \end{aligned} \tag{4.11}$$

Drift order parameter

We analyze the drifting oscillators for $k \in k_{\text{drift}} \equiv [k_{\min}, k_1] \cup [k_2, k_{\max}]$, where $k_{\min}$ denotes the minimal degree and $k_{\max}$ is the maximal degree. The phase of the drifting oscillators rotates with period T in the stationary state, so that their density $\rho(\phi, t; k)$ satisfies $\rho \sim |\dot{\phi}|^{-1}$ (Tanaka et al., 1997a). As $\oint \rho(\phi; k) d\phi = \int_0^T \rho(\phi; k)\dot{\phi} dt = 1$, this implies $\rho(\phi; k) = T^{-1}|\dot{\phi}|^{-1} = \frac{\Omega}{2\pi}|\dot{\phi}|^{-1}$, where Ω is the oscillating frequency of the running periodic solution of ϕ (Tanaka et al., 1997a). After substituting $\rho(\phi; k)$ into Eq. (4.5), we get

$$r_{\text{drift}} = \frac{1}{2\pi \langle k \rangle} \int_{k \in k_{\text{drift}}} \int_0^T kP(k)\Omega |\dot{\phi}|^{-1} e^{i\phi(t)} \dot{\phi} dt dk. \tag{4.12}$$

Without loss of generality, we assume that $\dot{\phi} < 0$ for $k \in [k_{\min}, k_1]$ and $\dot{\phi} > 0$ for $k \in [k_2, k_{\max}]$. Thus the real part of equation (4.12) becomes

$$r_{\text{drift}} = \frac{1}{2\pi \langle k \rangle} \left(- \int_{k_{\min}}^{k_1} + \int_{k_2}^{k_{\max}} \right) \int_0^T kP(k)\Omega \cos(\phi) dt dk. \tag{4.13}$$

A perturbation approximation of the self-consistent equations enables us to treat Eq. (4.13) analytically. After performing some manipulations motivated by (Tanaka et al., 1997a), we get

$$r_{\text{drift}} = \left(- \int_{k_{\min}}^{k_1} + \int_{k_2}^{k_{\max}} \right) \frac{-rk^2 \lambda \alpha^4 P(k)}{D^3 \left[k - \langle k \rangle - C(\lambda r)\right]^3 \langle k \rangle} dk \tag{4.14}$$

Thus, the self-consistent equation for the order parameter r is obtained by summing the contribution of locked and drifting oscillator as

$$r = r_{\text{lock}} + r_{\text{drift}}, \tag{4.15}$$

which are obtained from Eqs. (4.10) and (4.14), respectively.

4.2.2 Parameter space and synchronized boundaries

Determining C

The summation of Eq. (4.10) and Eq. (4.14) gives us the analytical solution for the order parameter r. However, there is a quantity to be determined, namely the term $C(\lambda r)$. Considering the sum of Eqs. (4.9) and (4.12) and taking its imaginary part, we get

$$\begin{aligned} 0 = & \frac{1}{\langle k \rangle} \int_{k_1}^{k_2} kP(k) \frac{D(k - \langle k \rangle - C(\lambda r))}{k\lambda r} dk \\ & + \frac{1}{2\pi \langle k \rangle} \left(- \int_{k_{\min}}^{k_1} + \int_{k_2}^{k_{\max}} \right) \int_0^T kP(k) \Omega |\dot{\phi}|^{-1} \sin \phi dt dk. \end{aligned} \tag{4.16}$$

Following a similar procedure to approximate $\int_0^T \cos\phi(t)dt$ in Eq. (4.13) (Tanaka et al., 1997a) for the integral $\int_0^T \sin\phi(t)dt$ in Eq. (4.16), we obtain

$$\begin{aligned} 0 = & \frac{1}{\langle k \rangle} \int_{k_1}^{k_2} kP(k) \frac{D(k - \langle k \rangle - C(\lambda r))}{k\lambda r} dk \\ & + \frac{1}{2 \langle k \rangle} \left(\int_{k_{\min}}^{k_1} + \int_{k_2}^{k_{\max}} \right) \frac{rk^2 \lambda \alpha^2 P(k)}{D^2 \left[k - \langle k \rangle - C(\lambda r) \right]^2} dk \end{aligned} \tag{4.17}$$

Therefore, through Eq. (4.17) we yield the evolution of $C(\lambda r)$ as a function of the coupling λ, and then, together with Eqs. (4.10) and (4.14), we have the full recipe to calculate the order parameter r.

It is known that systems governed by the equations of motion given by Eq. (4.7) present a hysteresis as λ is varied (Tanaka et al., 1997b; Tanaka et al., 1997a; Strogatz, 2014). Therefore we consider two distinct cases: (i) Increase of the coupling strength λ. In this case, the system starts without synchrony ($r \approx 0$) and, as λ is increased, approaches the synchronous state ($r \approx 1$). (ii) Decrease of the coupling strength λ. Now the system starts at the synchronous state ($r \approx 1$) and, as the λ is decreased, more and more oscillators lose synchrony, falling into the drift state.

Next, we study the following problem: why do phase transitions occur for a continuously varying coupling strength? We illustrate the phase transitions using the parameter space of the pendulum. For convenience, we non-dimensionalize Eq. (4.7) by

$\tau = \sqrt{k\lambda r}t$ (Strogatz, 2014), and set $\beta \equiv \alpha/\sqrt{k\lambda r}$ and $I \equiv D(k - \langle k\rangle - C(\lambda r))/(k\lambda r)$, yielding the dimensionless version:

$$\frac{d^2\phi}{d^2\tau} + \beta\frac{d\phi}{d\tau} + \sin\phi = I. \tag{4.18}$$

The variable β is the damping strength and I corresponds to a constant torque (cf. a damped driven pendulum). The bifurcation diagram in the $\beta - I$ parameter space of Eq. (4.18) has three types of bifurcations (Strogatz, 2014): homoclinic and infinite-period bifurcations periodic orbits, and a saddle-node bifurcation of fixed points. An analytical approximation for the homoclinic bifurcation curve for small β was derived using Melnikov's method (Strogatz, 2014; Guckenheimer and Holmes, 1983) and the curve is tangent to the line $I = 4\beta/\pi$.

The parameter space is divided into three different areas corresponding to the stable fixed point, the stable limit cycle and bistability. When $I > 1$ or $D(k - \langle k\rangle) > k\lambda r$ in Eq. (7), in the stable limit cycle area, there is no stable fixed point and the oscillators evolve to the stable limit cycle, regardless of the initial values of θ and $\dot{\theta}$. Therefore, in this case, the oscillators are drifting and contribute to r_{drift}. When $I < 1$ and I is below the homoclinic bifurcation curve, only stable fixed points exist and the oscillators converge to the stable fixed points and contribute to r_{lock}, regardless of the initial values. Otherwise, depending on the situation of the decreasing or increasing coupling strength, the oscillators within the bistable area converge to the stable fixed point (contributing to r_{lock}) or the stable limit cycle (contributing to r_{drift}), respectively.

Our change of time-scale allows us to employ Melnikov's analysis to determine the range of integration $[k_1, k_2]$ in the calculation of $r = r_{\text{lock}} + r_{\text{drift}}$.

Increasing coupling

When the coupling strength λ is increased from λ_0, the synchronous state emerges after a threshold λ_c^I has been crossed. Here we derive self-consistent equations that allow us to compute λ_c^I.

The stable fixed point and the stable limit cycle coexist in the bistable area. Whether the oscillator will converge to the fixed point or rotate periodically depends crucially on the initial values of θ and $\dot{\theta}$ for given parameter values of β and I. As the coupling strength increases, the bistable area vanishes and we only get the stable limit cycle in this region. The stability diagram for the increasing case is shown in Fig. 4.1(a). Therefore, as we can see from this figure, for $I > 1$, Eq. (4.18) has only one stable limit cycle solution. If $4\beta/\pi \leq I \leq 1$, the system is no longer bistable and only the limit cycle solution exists. If the coupling strength is increased further, the synchronized state can only exist for $I \leq 4\beta/\pi$, where Eq. (4.18) has a stable fixed point solution $\sin(\phi) = I$. Solving the inequalities

$$\frac{|D\,(k - \langle k\rangle - C(\lambda r))|}{k\lambda r} \leq 1, \tag{4.19}$$

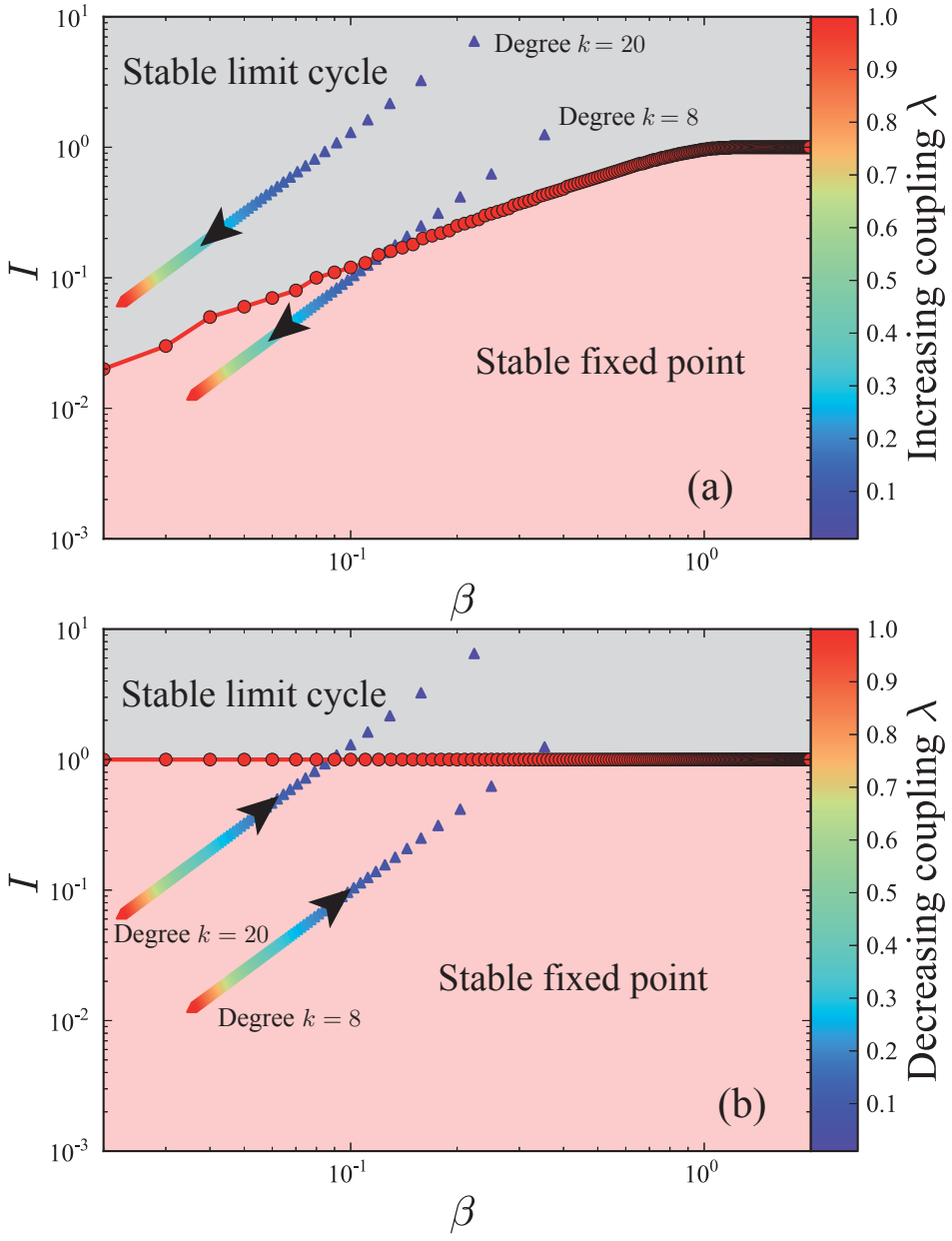

Figure 4.1: Parameter space of the pendulum [Eq. (4.18)]: (a) for increasing coupling strength and (b) decreasing coupling strength. The red (dark gray) area indicates the existence of a stable fixed point, whereas the gray area indicates the parameter combinations that give rise to a stable limit cycle. The dots in the parameter space represent oscillators with degree $k = 8$ and degree $k = 20$, which start with incoherence in (a) [coherence in (b)], and approach synchronous states (incoherence), for increasing (decreasing) coupling strength λ with $\alpha = 0.1$, $D = 0.1$, $\langle k \rangle = 10$, $C = -3$, $N = 3000$, and $P(k) \backsim k^{-\gamma}$, where $\gamma = 3$.

and

$$\frac{|D\left(k-\langle k\rangle - C(\lambda r)\right)|}{k\lambda r} \leq \frac{4\alpha}{\pi\sqrt{k\lambda r}}, \tag{4.20}$$

we get the following range of k^I for the phase-locked oscillators

$$k^I \in \left[k_1^I, k_2^I\right] = \begin{cases} \left[\frac{\langle k\rangle + C(\lambda r)}{1+\lambda r}, \frac{\langle k\rangle + C(\lambda r)}{1-\lambda r}\right] & \text{if } \lambda r < b, \\ \left[\frac{\langle k\rangle + C(\lambda r)}{1+\lambda r}, K_2^I\right] & \text{if } b < \lambda r < 1, \\ \left[K_1^I, K_2^I\right] & \text{otherwise,} \end{cases} \tag{4.21}$$

where $b = \frac{16\alpha^2}{\pi^2[\langle k\rangle + C(\lambda r)] + 16\alpha^2}$ and

$$\left[K_1^I, K_2^I\right] \equiv \left[\frac{B - \sqrt{B^2 - 4D^4\left(\langle k\rangle + C(\lambda r)\right)^2}}{2D^2}, \frac{B + \sqrt{B^2 - 4D^4\left(\langle k\rangle + C(\lambda r)\right)^2}}{2D^2}\right], \tag{4.22}$$

where

$$B = 2D^2(\langle k\rangle + C(\lambda r)) + \frac{16\alpha^2\lambda r}{\pi^2}. \tag{4.23}$$

Since λr is present in all equations, we define a new variable $y = \lambda r$ and analyze the self-consistent equations computing $r = y/\lambda$.

In order to visualize the dynamics and deepen the understanding of phase transitions, we sketch in Fig. 4.1(a) the phase trajectories of two randomly selected oscillators with degree $k = 8$ and 20. When the coupling strength is close to 0, the oscillators are in the stable limit cycle area and each node oscillates with their own natural frequency. One can see that the critical coupling for the onset of synchronization of the oscillator with degree $k = 8$ is lower and thus the small degree oscillator converges to the fixed point at lower coupling strength.

Decreasing coupling

With a decreasing coupling strength λ, the oscillators start from the phase-locked synchronous state and reach the asynchronous state at a critical coupling λ_c^D. In order to calculate this threshold, we again investigate the range of degree k^D of the phase-locked oscillators. Imposing the phase locked solution in Eq. (4.7), we obtain $\sin\phi = \frac{|D(k-\langle k\rangle - C(\lambda r))|}{k\lambda r} \leq 1$ and find that the locked oscillators are the nodes with

degree k in the following range as a function of λr:

$$k^D \in [k_1^D, k_2^D] \equiv \left[\frac{\langle k \rangle + C(\lambda r)}{1 + \frac{\lambda r}{D}}, \frac{\langle k \rangle + C(\lambda r)}{1 - \frac{\lambda r}{D}} \right], \tag{4.24}$$

when $\lambda r < D$, or $k_1^D = \frac{\langle k \rangle + C(\lambda r)}{1 + \frac{\lambda r}{D}}$ and $k_2^D \to k_{\max}$ otherwise. This allows us to calculate r^D and λ_c^D from the self-consistent Eqs. (4.10) and (4.14).

Following the same procedure for increasing coupling strength, we also sketch phase trajectories of two oscillators with degree $k = 8$ and 20, respectively, in the parameter space as shown in Fig. 4.1(b). For high coupling strength, the population acts like a giant node and $r \simeq 1$. If $I < 1$, only a stable fixed point exists, whereas the oscillators converge to fixed points. The oscillators with degrees $k \geq 20$ are dragged out of synchronization more easily. For $I > 1$ the oscillators with degree $k = 20$ are easier to be out of synchronization compared to the ones with degree $k = 8$. In this way, the order parameter r would first slightly decrease and then abruptly drop to lower values.

4.2.3 Simulations on scale-free networks

We demonstrate the validity of our mean-field analysis by conducting numerical simulations of the second-order Kuramoto model with $\alpha = 0.1$ and $D = 0.1$ on Barabási-Albert scale-free networks characterized by $N = 3000$, $\langle k \rangle = 10$, $k_{\min} = 5$ and the degree distribution $P(k) \sim k^{-\gamma}$, with $\gamma = 3$. Again, due to hysteresis, we have to distinguish two cases. First, we increase the coupling strength λ from λ_0 by amounts of $\delta\lambda = 0.1$, and compute the order parameter r^I for $\lambda = \lambda_0, \lambda_0 + \delta\lambda, ..., \lambda_0 + n\delta\lambda$. Second, we gradually decrease λ from $\lambda_0 + n\delta\lambda$ to λ_0 in steps of $\delta\lambda$. Before each $\delta\lambda$-step, we integrate the system long enough (10^5 time steps) to arrive at stationary states, using a 4^{th} order Runge-Kutta method with time step $dt = 0.01$.

Figure 4.2(a) shows the synchronization diagrams for the model defined in Eq. (4.2). The system exhibits the expected hysteretic synchrony depending on initial conditions. In the case of an increasing coupling strength λ, the initial drifting oscillators can be entertained to locked oscillators after certain transience. The order parameter r remains at a low value until the onset of synchronization, λ_c^I, at which a first-order synchronization transition occurs, and r increases continuously after that. In the case of decreasing λ, initially locked oscillators are desynchronized and fall into drift states once λ crosses λ_c^D. For a high coupling strength, all oscillators are synchronized and $r = 1$. As the coupling strength is decreased, the synchronized oscillators fall into unsynchronized states. As the two discontinuous transitions take place at different coupling thresholds, the order parameter exhibits hysteresis.

To validate our mean-field analysis with simulation results, we simultaneously solve Eqs. (4.11), (4.14), (4.17), and (4.21) [(4.11), (4.14), (4.17), and (4.24)] for increasing (decreasing) coupling strength. Note that the distribution of the natural frequencies is proportional to the degree distribution, and ψ can not be set to a constant as has been done in previous works (Strogatz, 2000). Recalling that $C(\lambda r)$ depends on $\dot{\psi}$

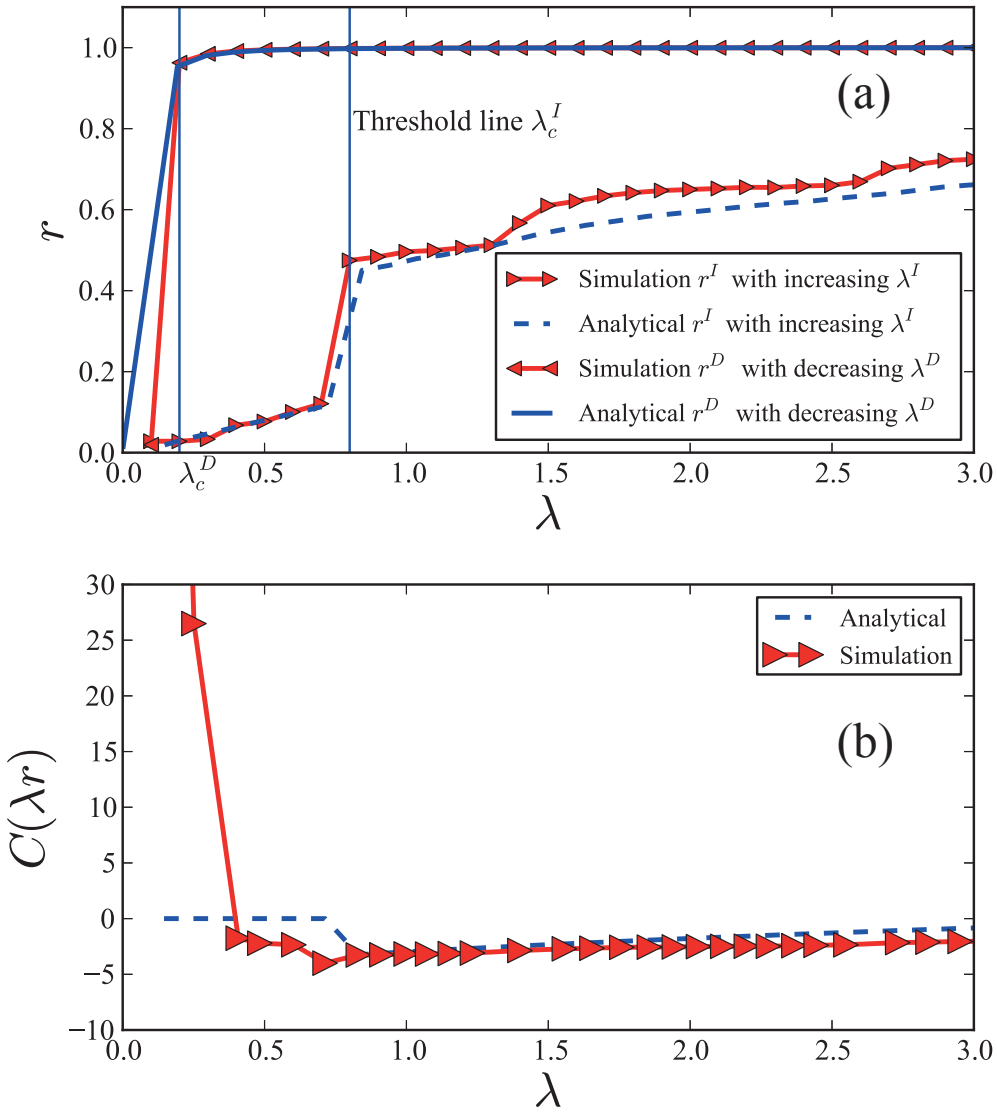

Figure 4.2: Analytical (in blue) and numerical (in red) analysis of the order parameter r (a) and $C(\lambda r)$ with increasing coupling strength (b) for synchronization diagrams. We set the value $C(\lambda r)$ to be 0 if $\lambda < \lambda_c^I$. The analytical plots are calculated from Eqs. (4.11), (4.14), and (4.17) with the synchronized boundary Eq. (4.21) for increasing coupling and for decreasing coupling (4.24). Here the simulations are conducted with $\alpha = 0.1$, $D = 0.1$, and Barabási-Albert scale-free networks characterized by $N = 3000$, $\langle k \rangle = 10$, and $k_{\min} = 5$.

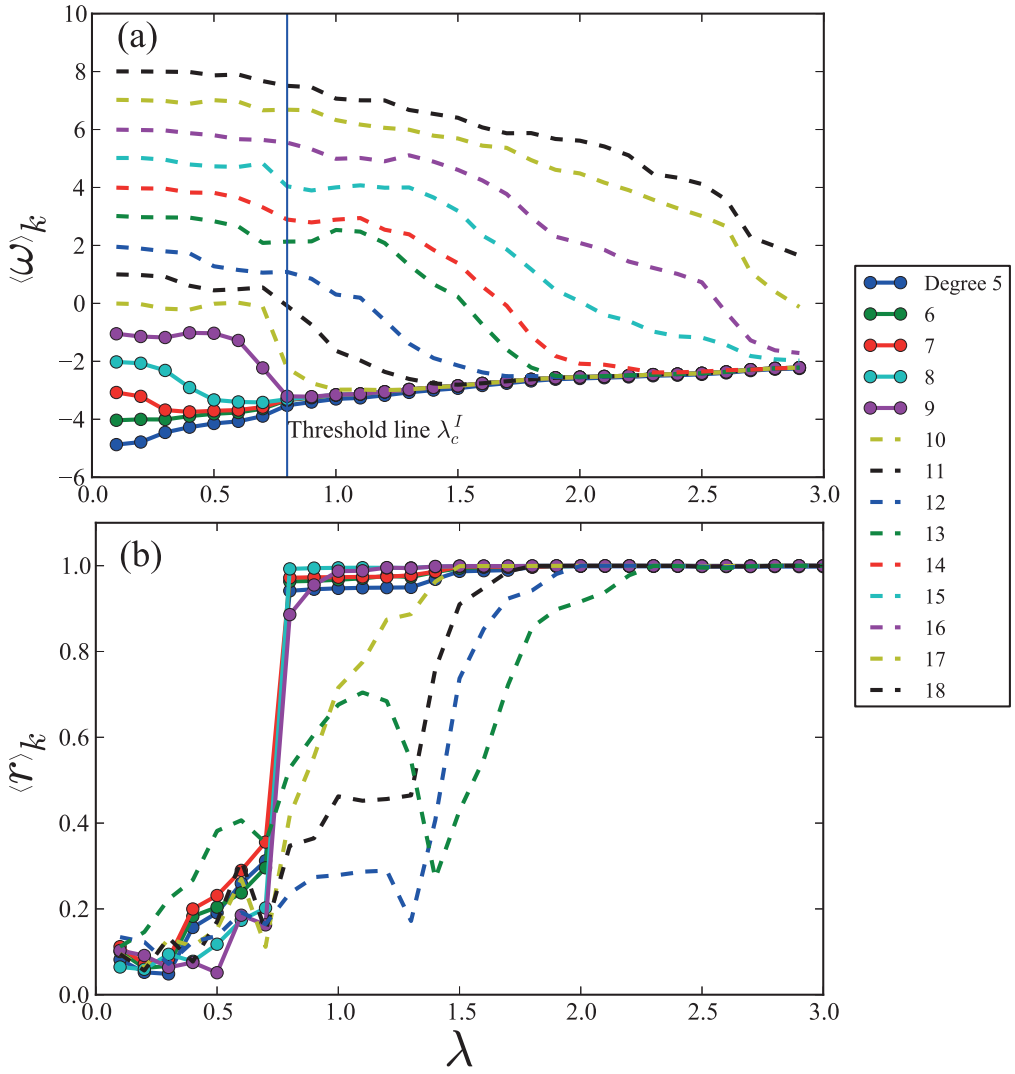

Figure 4.3: (a) Average frequency $\langle\omega\rangle_k$ and (b) order parameter $\langle r\rangle_k$ of each cluster from simulations with $\langle k\rangle = 10$. Solid lines denote synchronized clusters at the onset of synchronization. Dashed lines denote clusters composed of large degree nodes. The simulation parameters are the same as in Fig. 4.2.

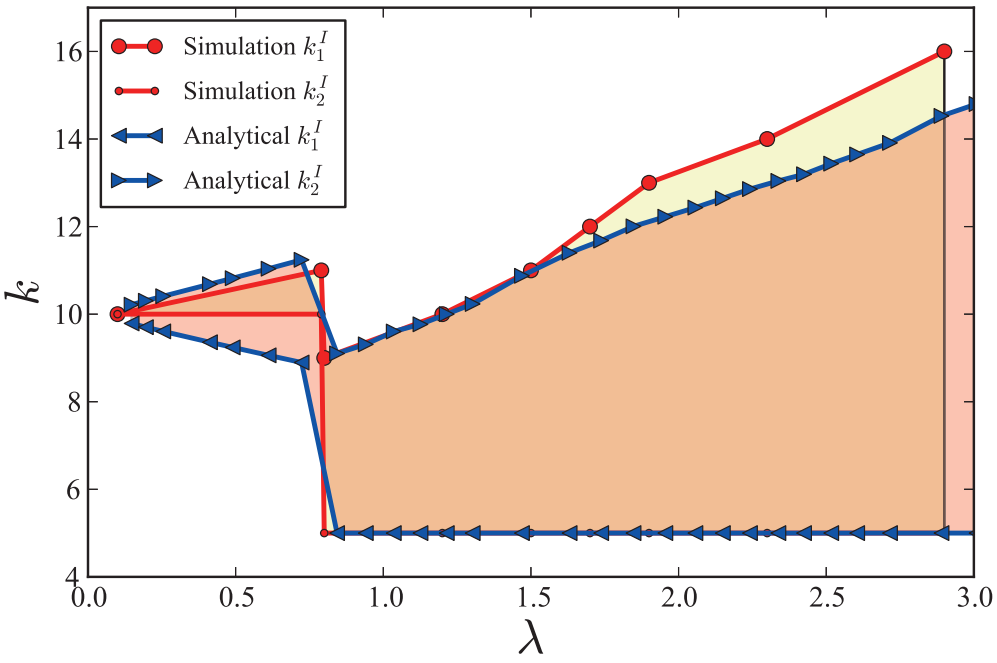

Figure 4.4: Synchronized degrees from analytical and simulation results with increasing coupling strength. The yellow (light gray) shading shows the range of synchronized degrees from the simulations and the red (dark gray) shading shows the range from the analytical results.

and $\ddot{\psi}$, we assume that $C(\lambda r) \approx 0$ when $\lambda < \lambda_c^I$, as each node oscillates at its own natural frequency. The oscillators with small degree synchronize first as shown in Fig. 4.3, and being in high percentage in a scale-free network, they dominate the mean field. The mean field rotates with a constant frequency $\dot{\psi}$. As before, it is convenient to analyze the system with $y \equiv \lambda r$ and $r = y/\lambda$. As we can see, the analytical results are in good agreement with the simulations.

To deepen the understanding of the transition to synchrony, we calculate the average frequency of all oscillators of degree k (Ji et al., 2014a), $\langle\omega\rangle_k = \sum_{[i|k_i=k]} \omega_i/(NP(k))$, where $\omega_i = \int_t^{t+T} \dot{\phi}_i(\tau)dt/T$ and t is large enough to let all oscillators reach stationary states. Figure 4.3(a) shows that each cluster, an ensemble of oscillators with same degree, oscillates independently before the onset of synchronization. Oscillators with small degree, denoted by a solid line, join the synchronous component simultaneously at λ_c^I. For further increasing coupling strength λ, more clusters, denoted by dashed lines, join the synchronized component successively according to their degrees, starting from smaller ones, and correspondingly $C(\lambda r)$ increases.

What happens inside each cluster at the onset of synchronization? We define the order parameter of each cluster denoted by $\langle r\rangle_k$, $\langle r\rangle_k = \int_t^{t+T} r_k dt/T$, where

$r_k e^{i\psi_k} = \sum_{[i|k_i=k]} e^{i\theta_k}/(NP(k))$. When $\lambda < \lambda_c^I$ and initial values of θ are selected at random from $[-\pi, \pi]$, the oscillators of each cluster follow the same dynamics. Therefore, the oscillators are uniformly distributed over the limit cycle and $\langle r \rangle_k \approx 0$ as shown in Fig. 4.3(b). The order parameter of the synchronized clusters denoted by a solid line in Fig. 4.3 jumps to 1 at the onset of synchronization. After that, other clusters join the synchronized component and $\langle r \rangle_k$ approaches 1 as denoted by the dashed lines.

In Fig. 4.4, we show the synchronized boundary $k^I \in [k_1^I, k_2^I]$ as a function of the coupling strength λ calculated from analytical expressions and extensive simulations for increasing λ. The analytical and simulation results are in good agreement. Note that the discontinuity of evolution of the synchronized boundary gives rise to a first-order phase transition in Fig. 4.2(a). After the transition to synchrony, the low boundary k_1^I stays constant at the minimal degree $k_{\min} = 5$, and, as more clusters join the synchronized component, the upper boundary k_2^I increases with λ.

The above results are based on scale-free networks with the average degree $\langle k \rangle = 10$. To show more details, following the above process, we analyze the increasing coupling case with an average degree $\langle k \rangle = 12$ with minimum degree $k_{\min} = 6$ as shown in Fig. 4.5. We integrate the equations (4.11), (4.14), (4.17) with (4.21) and get the evolution of the $C(\lambda r)$ and the order parameter r as a function of the coupling strength λ. We observe that the critical coupling strength in this case is smaller than that of scale-free networks with an average degree $\langle k \rangle = 10$.

We follow the above process again and investigate the synchronization inside each cluster. As expected, initially oscillators for each cluster oscillate around its natural frequency and the order parameter r for each cluster remains at a low value (Fig. 4.6). Increasing the coupling strength further, a first-order transition to synchronization occurs at the threshold $\lambda_c^I = 0.6$. Clusters of nodes with a degree from $k = 6$ to $k = 10$ join the synchronization component simultaneously. More clusters join the synchronized component successively starting from low to high degrees.

We also evaluate the influence of the average degree on the critical coupling threshold. Figure 4.7 shows the mean values of the critical coupling strength $\left\langle \lambda_c^I \right\rangle$ for increasing λ with different minimal degrees $k_{\min}$ varying from $k_{\min} = 2$ to $k_{\min} = 20$. In simulations, we define a transition to synchrony if the difference between $r(\lambda)$ and $r(\lambda - \delta\lambda)$ is larger than, for example, 0.1. Due to the limitation of networks size, fluctuations of $\left\langle \lambda_c^I \right\rangle$ are unavoidable. The plots have been obtained with the same parameter values as above except minimal degrees $k_{\min}$. One can observe that the threshold values decrease with increasing minimal degrees initially and become almost constant afterwards.

To investigate the system's dynamical behavior in networks with different levels of heterogeneity, in Fig. 4.8 we present the synchronization diagrams for the forward and backward continuation of the coupling λ for networks with degree distribution $P(k) \sim k^{-\gamma}$ considering different exponents γ. As expected, the onset of synchronization decreases for the forward propagation of the coupling strength λ, similarly to that observed in the first-order model (Gómez-Gardenes et al., 2011). Interestingly, the

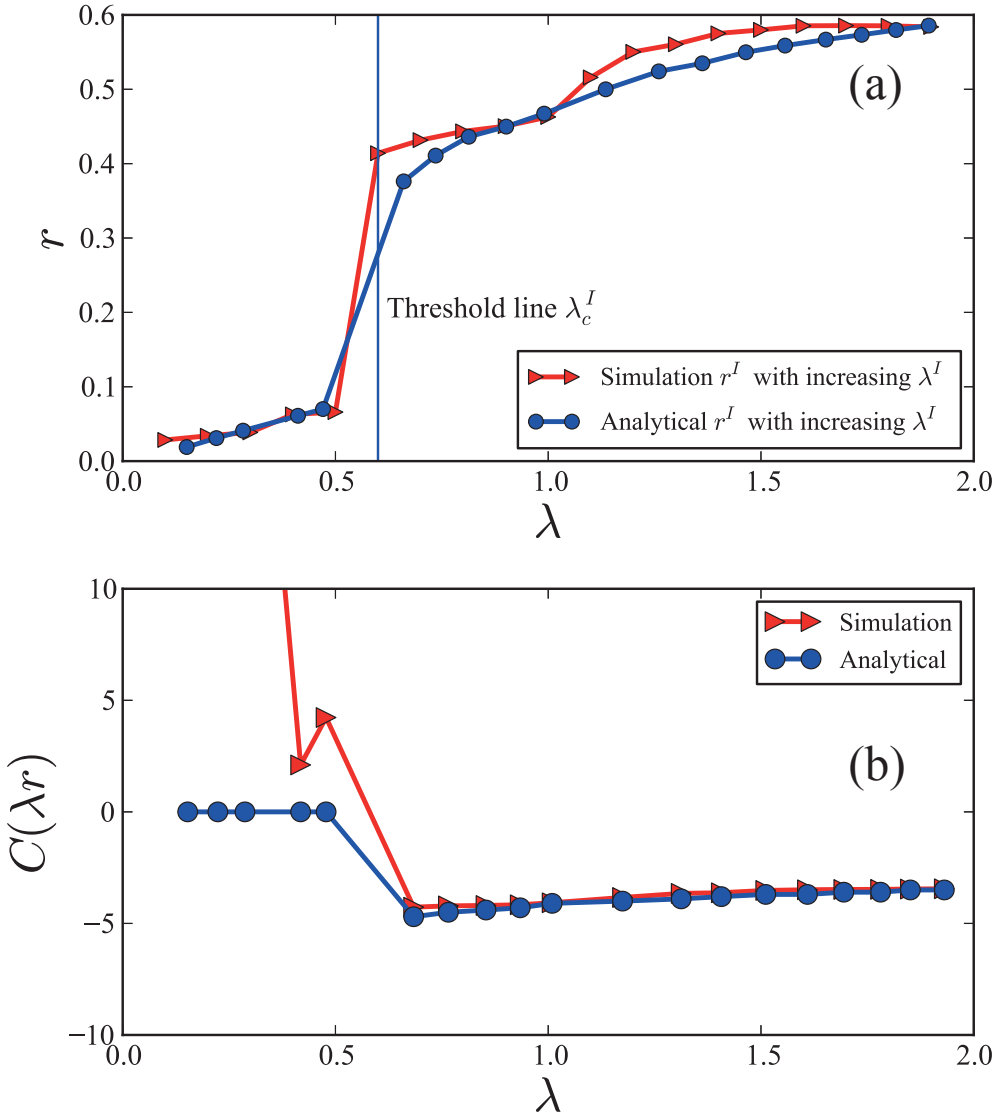

Figure 4.5: Results with increasing coupling strength λ. Part (a) shows the order parameter r vs. λ. The red (blue) curve denotes the simulations (analytical) results. Part (b) shows the $C(\lambda r)$ vs. λ. The critical coupling is 0.6. As in Fig. 4.2(b), we take the value from solid lines. The analytical results are obtained from Eqs. (4.11), (4.14), (4.17), and (4.21). Here the simulations are conducted with $\alpha = 0.1$, $D = 0.1$ and Barabási-Albert scale-free networks characterized by $N = 3000$, $\langle k \rangle = 12$, and $k_{\min} = 6$.

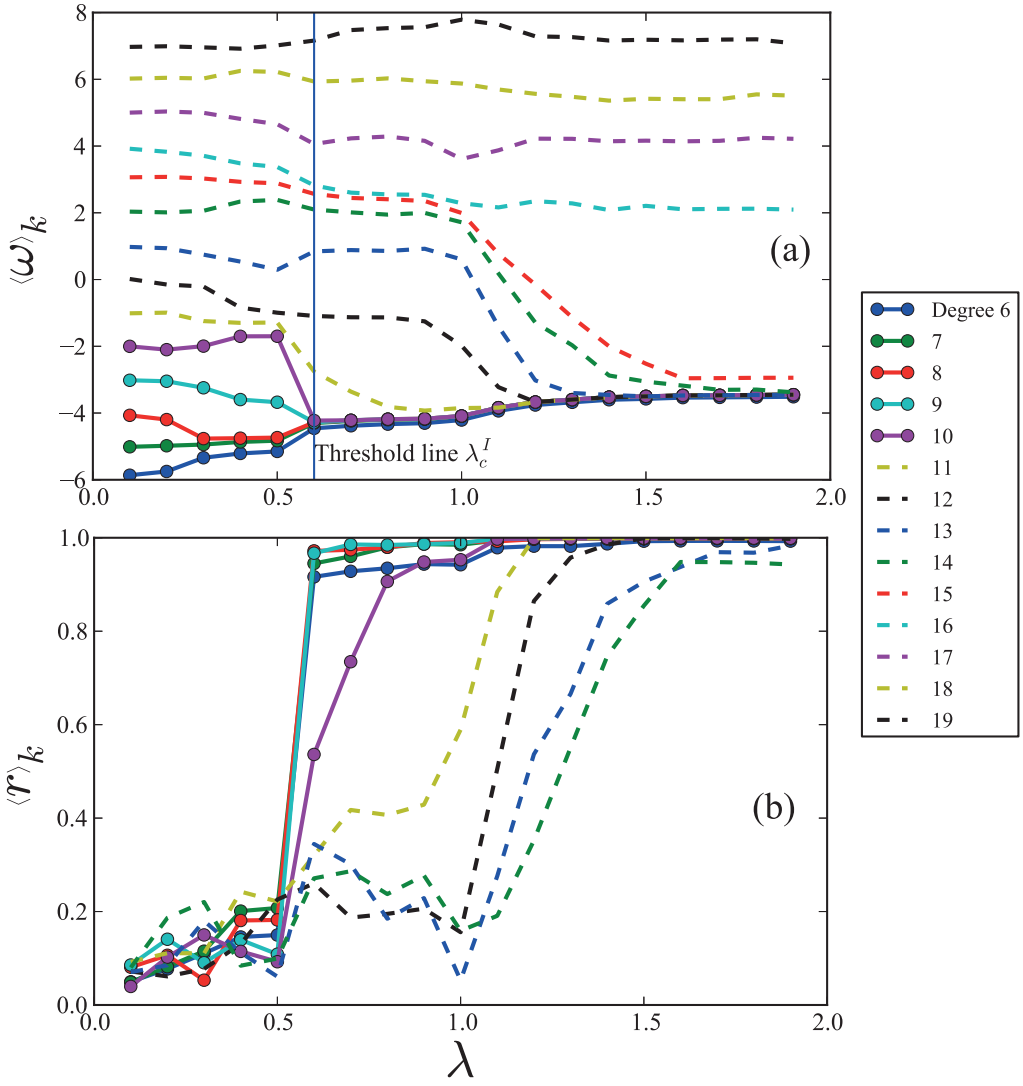

Figure 4.6: Results are obtained with the same parameter values as in Fig. 4.5. Part (a) shows the evolution of the average frequency of each cluster $\langle\omega\rangle_k$ as a function of λ, and (b) indicates the evolution of the order parameter of each cluster $\langle r\rangle_k$ of λ. Solid lines indicate the clusters synchronized at the critical threshold. The simulation parameters are the same as in Fig. 4.5.

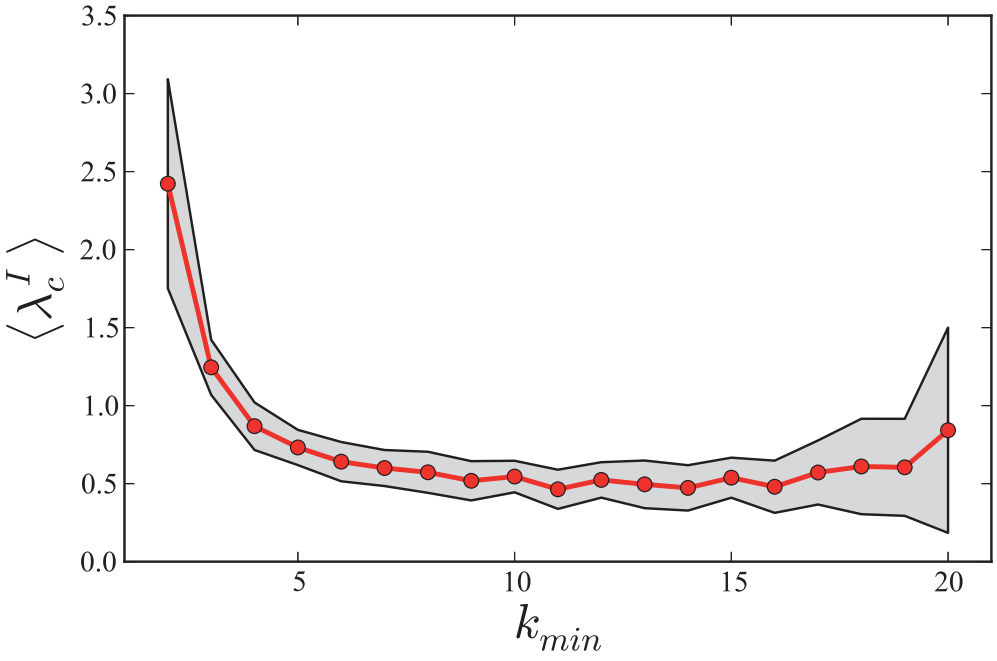

Figure 4.7: Mean values of critical coupling strength $\langle \lambda_c^I \rangle$ for increasing coupling with different minimal degrees $k_{\min}$. The gray shading indicates the standard deviation. Simulations at each minimal degree are conducted as in Fig. 4.2. All networks have $N = 3000$.

branch associated to the backward propagation of the coupling λ is barely affected by the changes of γ. A similar effect was recently reported in (Olmi et al., 2014), where the authors observed a weak dependence of the critical coupling λ_c^D on the network size N.

4.2.4 Simulations on Watts-Strogatz networks

Previous studies of first-order transitions to synchronization with natural frequency correlated with degree are based on scale-free networks. Next, we also simulate the model in Eq. (4.2) on Watts-Strogatz networks by tuning the rewiring parameter $p \in [0, 1]$.

Synchronization appears when a tiny fraction of shortcuts comes into the system, moreover, the synchronizability increases with p as shown in (Hong et al., 2002). Compared to these results, in Fig. 4.9, we observe counter-intuitive results that the synchronizability decreases with the increasing of p. Synchronization exhibits strong dependence on the rewiring probability p. For small p, the system has a tiny fraction of short-cuts and most oscillators have a degree close to the average degree. Therefore, a high percentage of oscillators have a small natural frequency $D(k - \langle k \rangle)$ and tend to synchronize to the mean-field quantities already for a small coupling strength. For

large p, due to the divergence of oscillators and large natural frequencies, the system needs a large coupling strength to recruit most oscillators into the synchronized component.

Fig. 4.10 shows the order parameter $\langle r \rangle_k$ of each cluster k with increasing coupling strength λ. The solid lines denote fist-order transitions of clusters which join the synchronized component at the threshold. For small p, these clusters being in a high percentage produce fist-order transitions as shown in Fig. 4.9.

Correspondingly, one can see in Fig. 4.11(a) for $p = 0.1$, clusters with degrees from 8 to 10 synchronize to the zero mean-field value and other clusters join the synchronized component successively. Compared to small p, in Fig. 4.11(b), clusters join the synchronized component continuously.

4.2.5 Quenched disorder

In the preceding section, we showed that abrupt transitions occur in scale-free networks of second-order Kuramoto oscillators, but the dependence of such discontinuous transitions on perturbations in the correlation between natural frequencies and

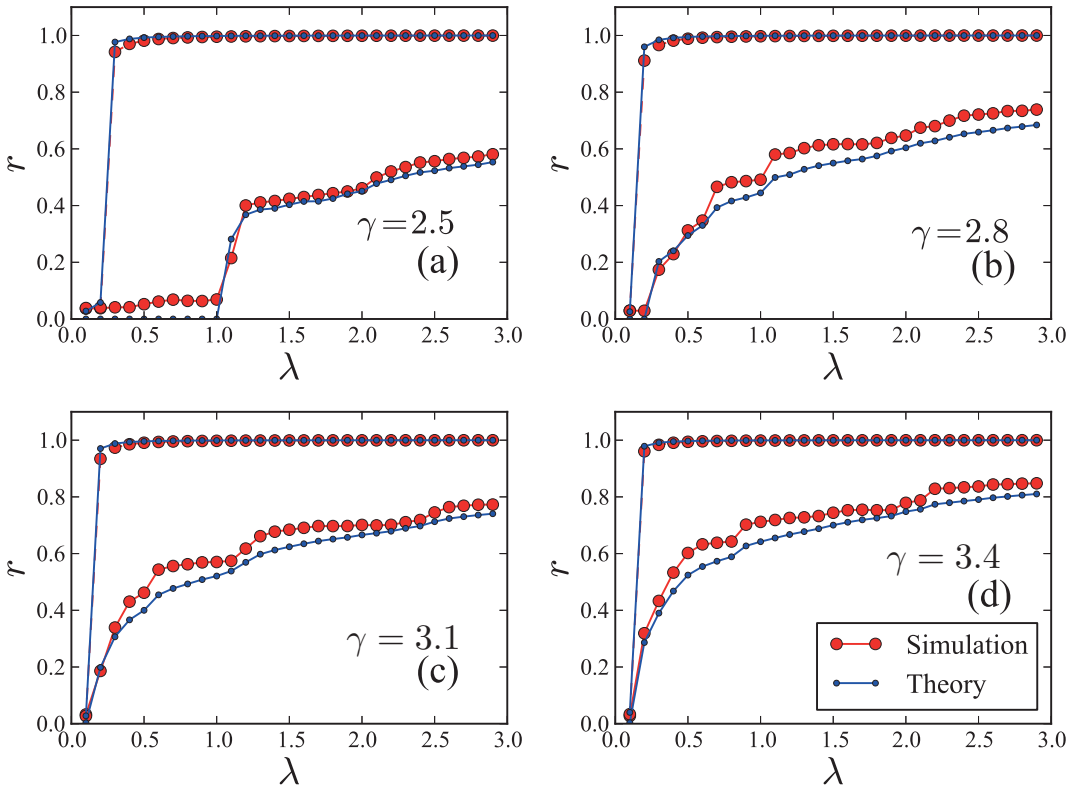

Figure 4.8: Synchronization diagrams for networks with the degree-distribution $P(k) \sim k^{-\gamma}$ for different exponents γ. The analytical plots are calculated from the summation of Eqs. (4.10) and (4.13). All networks have $N = 3000$ and $\langle k \rangle = 10$.

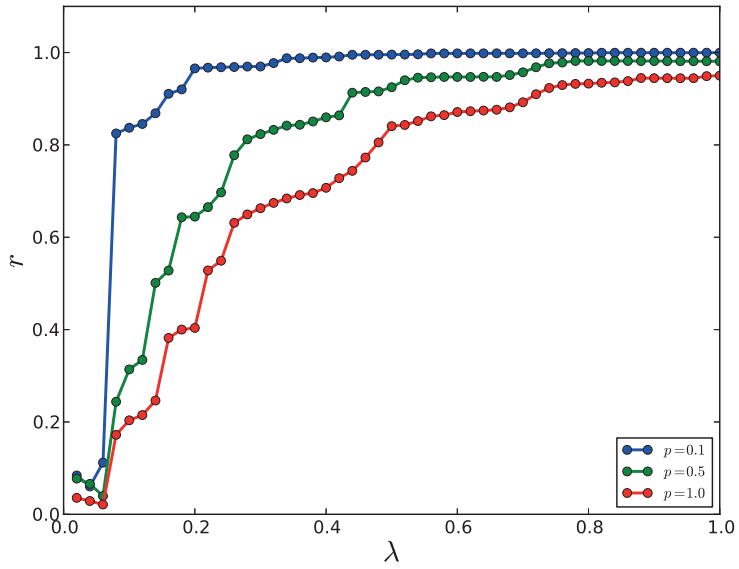

Figure 4.9: Order parameter r vs. coupling strengths λ for different p. Synchronizability decreases with p's increase. A first-order phase transition is obvious for $p = 0.1$.

topological properties is unknown. To address this question, here we consider the inclusion of quenched disorder on the natural frequencies in order to disturb such correlations (Skardal and Arenas, 2014; Zou et al., 2014). More precisely, to check the robustness of cluster explosive synchronization, we set $\Omega_i = D(k_i - \langle k \rangle) + \varepsilon_i$, where $\varepsilon \in [-q, q]$ is randomly drawn from a uniform distribution $g(\varepsilon)$. Therefore, the equations of motion in the continuum limit are given by

$$\ddot{\phi} = -\alpha\dot{\phi} + D\left[k - \langle k \rangle - C(\lambda r)\right] + \varepsilon - k\lambda r \sin\phi. \tag{4.25}$$

As we increase the width of the distribution $g(\varepsilon)$, the topological influence on the natural frequency is decreased.

We can calculate the contribution of locked oscillators $r^{\mathrm{q}}_{\mathrm{lock}}$ through

$$r^{\mathrm{q}}_{\mathrm{lock}} = \frac{1}{\langle k \rangle} \int_{-q}^{q} \int_{k_1^{\mathrm{q}}(\varepsilon)}^{k_2^{\mathrm{q}}(\varepsilon)} kP(k)g(\varepsilon) \times \sqrt{1 - \left[\frac{D(k - \langle k \rangle - C(\lambda r)) + \varepsilon}{k\lambda r}\right]^2} dk d\varepsilon, \tag{4.26}$$

where the degree range of the synchronous oscillators $k^{\mathrm{q}} \in [k_1^{\mathrm{q}}(\varepsilon), k_2^{\mathrm{q}}(\varepsilon)]$ in the presence of quenched disorder is determined by the conditions

$$\frac{\left|D\left[k - \langle k \rangle - C(\lambda r)\right] + \varepsilon\right|}{k\lambda r} \leq 1, \tag{4.27}$$

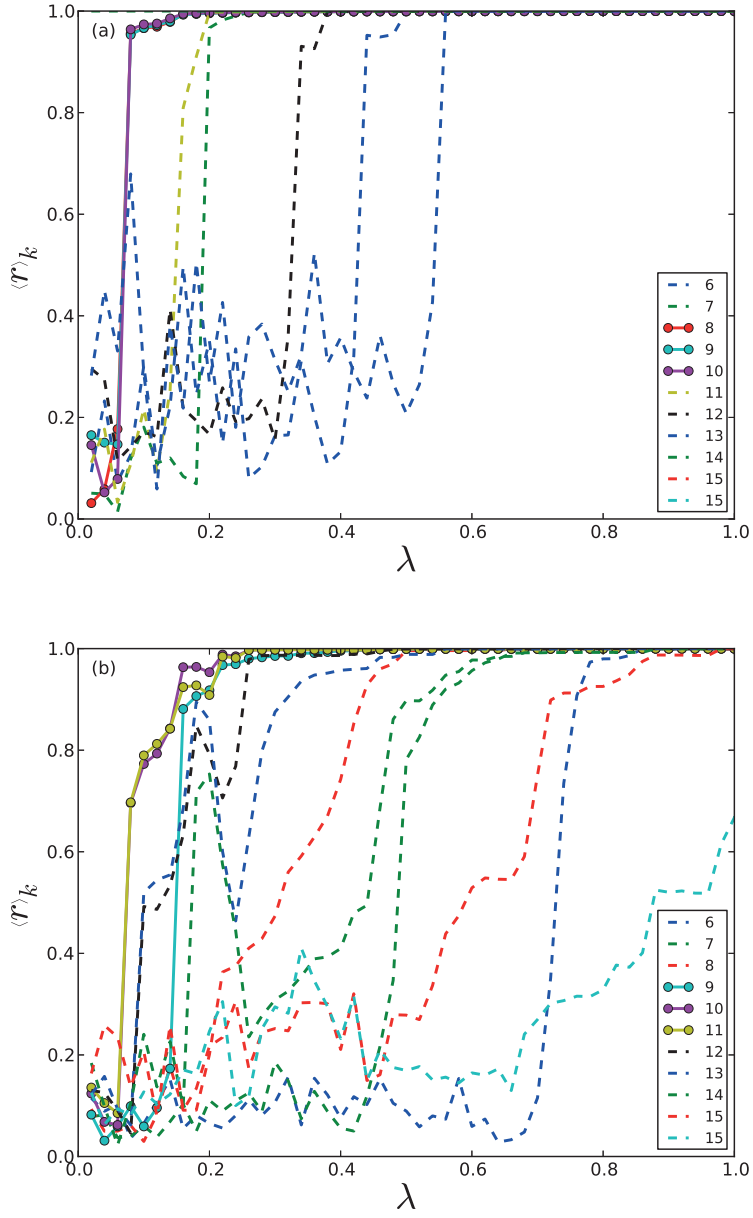

Figure 4.10: Order parameter of each cluster vs. coupling strengths λ for $p = 0.1$ and $p = 1$. Clusters with natural frequencies close to o tend to synchronize to the mean-field quantities at the threshold and first-order transitions of these clusters are represented by solid lines.

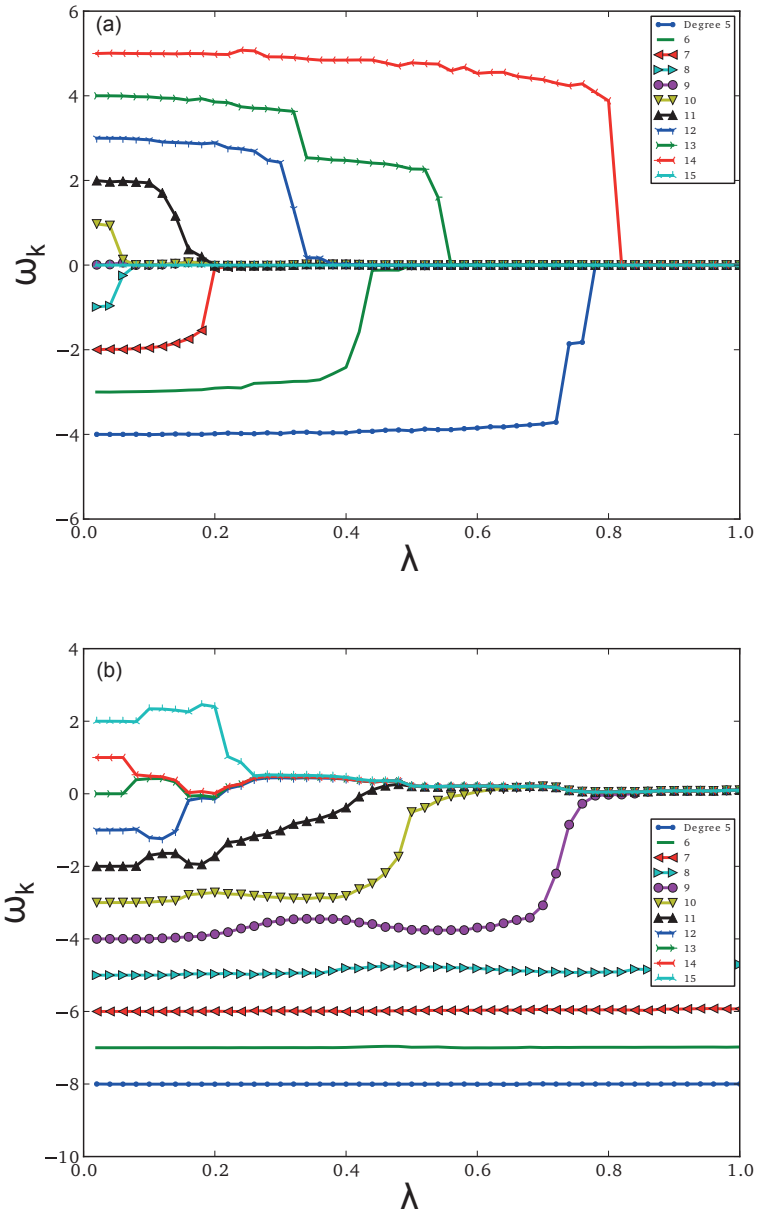

Figure 4.11: Average frequency of each cluster $\langle\omega\rangle_k$ vs. coupling strengths λ. In (a), for $p = 0.1$, clusters being in high percentage join in the synchronized component at the threshold and determine the 0 mean frequency. Other clusters join to the 0 mean-field afterwards according to the degree difference to the average degree. In (b), clusters join the synchronized component continuously.

and

$$\frac{|D\left[k-\langle k\rangle - C(\lambda r)\right]+\varepsilon|}{k\lambda r} \leq \frac{4\alpha}{\sqrt{k\lambda r}}. \tag{4.28}$$

Similarly, one can also get the contribution of drift oscillators denoted by $r^{\mathrm{q}}_{\mathrm{drift}}$ as follows

$$\begin{aligned} r^{\mathrm{q}}_{\mathrm{drift}} = & \\ & -\int d\varepsilon \left(\int_{k_{\min}}^{k_1^{\mathrm{q}}(\varepsilon)} dk + \int_{k_2^{\mathrm{q}}(\varepsilon)}^{k_{\max}} dk\right) \frac{-rk^2\lambda\alpha^4 P(k) g(\varepsilon)\Theta\left(D\left[\langle k\rangle + C(\lambda r) - k\right]-\varepsilon\right)}{\left[D(k-\langle k\rangle - C(\lambda r))+\varepsilon\right]^3 \langle k\rangle} \\ & +\int d\varepsilon \left(\int_{k_{\min}}^{k_1^{\mathrm{q}}(\varepsilon)} dk + \int_{k_2^{\mathrm{q}}(\varepsilon)}^{k_{\max}} dk\right) \frac{-rk^2\lambda\alpha^4 P(k) g(\varepsilon)\Theta\left(D\left[k-\langle k\rangle - C(\lambda r)\right]+\varepsilon\right)}{\left[D(k-\langle k\rangle - C(\lambda r))+\varepsilon\right]^3 \langle k\rangle}, \end{aligned}$$

where $\Theta(\cdot)$ is the Heaviside function. Figure 4.12 shows the synchronization diagrams considering the same network configuration as in Fig. 4.2, but taking into account different values for the quenched disorder. As we can see, the phase coherence of the lower branches decreases, enlarging the hysteresis area with increasing q. Interestingly, the upper branches decrease as the strength of the quenched disorder is increased and the onset of the transition increases accordingly. Therefore, the additional quenched disorder decreases the phase coherence and diminishes the abrupt transitions.

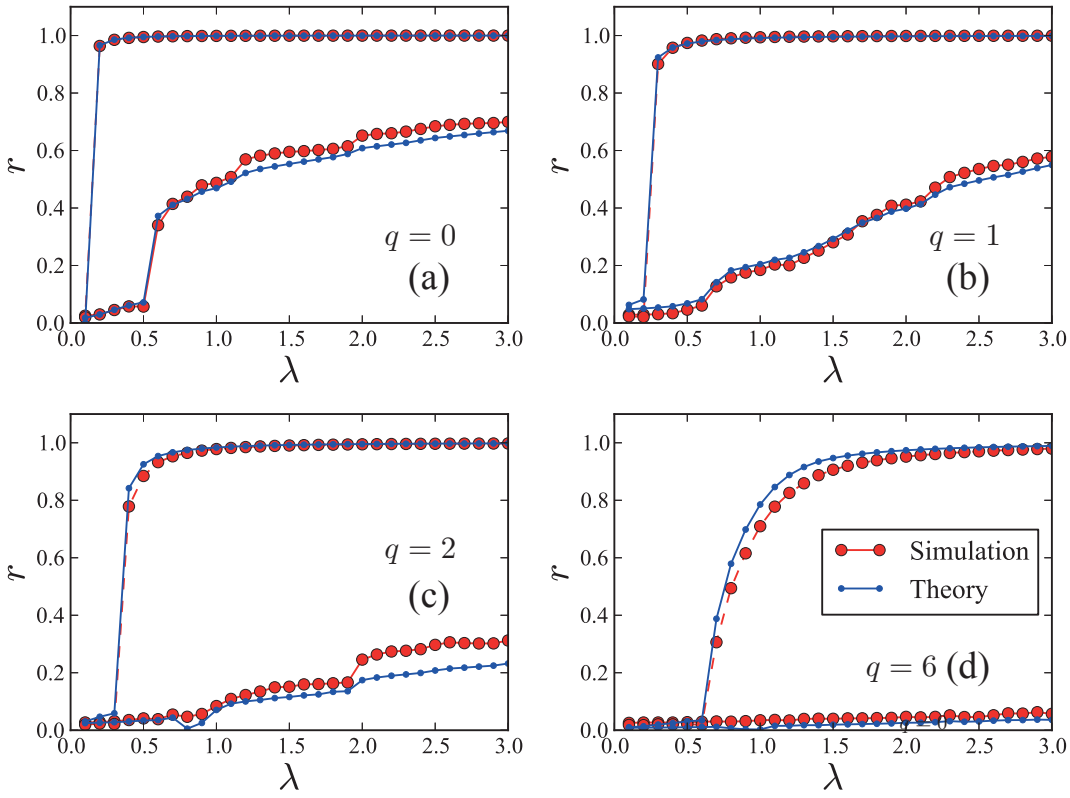

Figure 4.12: Synchronization diagrams with respect to different probabilities q with $q = 0$ (a), $q = 1$ (b), $q = 2$ (c), and $q = 6$(d). Analytical results are obtained from the summation of $r^{\mathrm{q}}_{\mathsf{lock}}$ and $r^{\mathrm{q}}_{\mathsf{drift}}$. Here, we use the same network topology as in Fig. 4.2 with $N = 3000$, $\alpha = 0.1$, $D = 0.1$, and set $g(\varepsilon) = 1/2q$ with $\varepsilon \in [-q, q]$.

4.3 Effects of assortative mixing

4.3.1 Synchronization in correlated networks

We consider networks where each node is a phase oscillator evolving according to the second-order Kuramoto model (2.1) (Arenas et al., 2008; Acebrón et al., 2005). The collective dynamics of the oscillators is measured by the macroscopic order parameter, defined as $r(t)e^{i\psi(t)} = \frac{1}{N}\sum_{j=1}^{N} e^{i\theta_j(t)}$, where the modulus $0 \leq r(t) \leq 1$ and $\psi(t)$ is the average phase of the oscillators. The system governed by Eq. (2.1) exhibits hysteretic synchrony (Tanaka et al., 1997b; Tanaka et al., 1997a). The onset of synchronization ($r > 0$) is characterized by a critical coupling λ_c^{I} when the coupling strength is progressively increased from a given λ_0. On the other hand, starting at synchronouos state and decreasing progressively the coupling strength, the oscillators fall into an incoherent state ($r \approx 0$) at coupling $\lambda_c^{\mathrm{D}} \leq \lambda_c^{\mathrm{I}}$ (Tanaka et al., 1997b; Tanaka et al., 1997a) (see section 2.1.3).

Here we study the second-order Kuramoto model [see Eq. (2.1)] in which the natural frequency distribution $g(\Omega)$ is correlated with the degree distribution $P(k)$ as $\Omega_i = k_i - \langle k \rangle$ (Ji et al., 2013) instead of Eq. (4.1), where k_i is the degree of the oscillator i and $\langle k \rangle$ is the average degree of the network. At first glance that particular choice for the frequency assignment could sound odd; however, it is not difficult to find physical scenarios where this configuration is plausible. For example, such correlation between dynamics and network topology can arise as a consequence of a limited amount of resources or energy supply for the oscillators. In fact, studies on optimization of synchronization in complex networks (Skardal et al., 2014; Buzna et al., 2009; Brede, 2008) have shown that, for a given fixed set of allowed frequencies $\{\Omega_1, \Omega_2, ..., \Omega_N\}$, the configuration that maximizes the network synchronization is reached for cases in which frequencies are positively correlated with degrees. Therefore, this correlation between frequencies and local topology can be seen as an optimal scenario for the emergence of collective behavior in complex networks.

We study networks presenting nonvanishing degree-degree correlation. Such a correlation is quantified by a measure known as assortativity coefficient, $\mathcal{A}$, which is the Pearson coefficient between degrees at the end of each link (Newman, 2002), i.e.

$$\mathcal{A} = \frac{M^{-1}\sum_i j_i k_i - \left[M^{-1}\sum_i \frac{1}{2}(j_i + k_i)\right]^2}{M^{-1}\sum_i \frac{1}{2}(j_i^2 + k_i^2) - \left[M^{-1}\sum_i \frac{1}{2}(j_i + k_i)\right]^2}, \tag{4.29}$$

where $-1 \leq \mathcal{A} \leq 1$, j_i and k_i are the degrees associated to the two ends of the edge i ($i = 1, ..., M$), and M is the total number of edges in the network. In order to tune the degree of assortativity of each network, we use the method proposed in (Xulvi-Brunet and Sokolov, 2004). The algorithm allows us to obtain networks with a desired value of assortativity without changing the degree of each node. At each step, two edges are selected at random and the four nodes associated to these edges are ordered from the lowest to the highest degree. In order to produce assortative mixing ($\mathcal{A} > 0$), with a

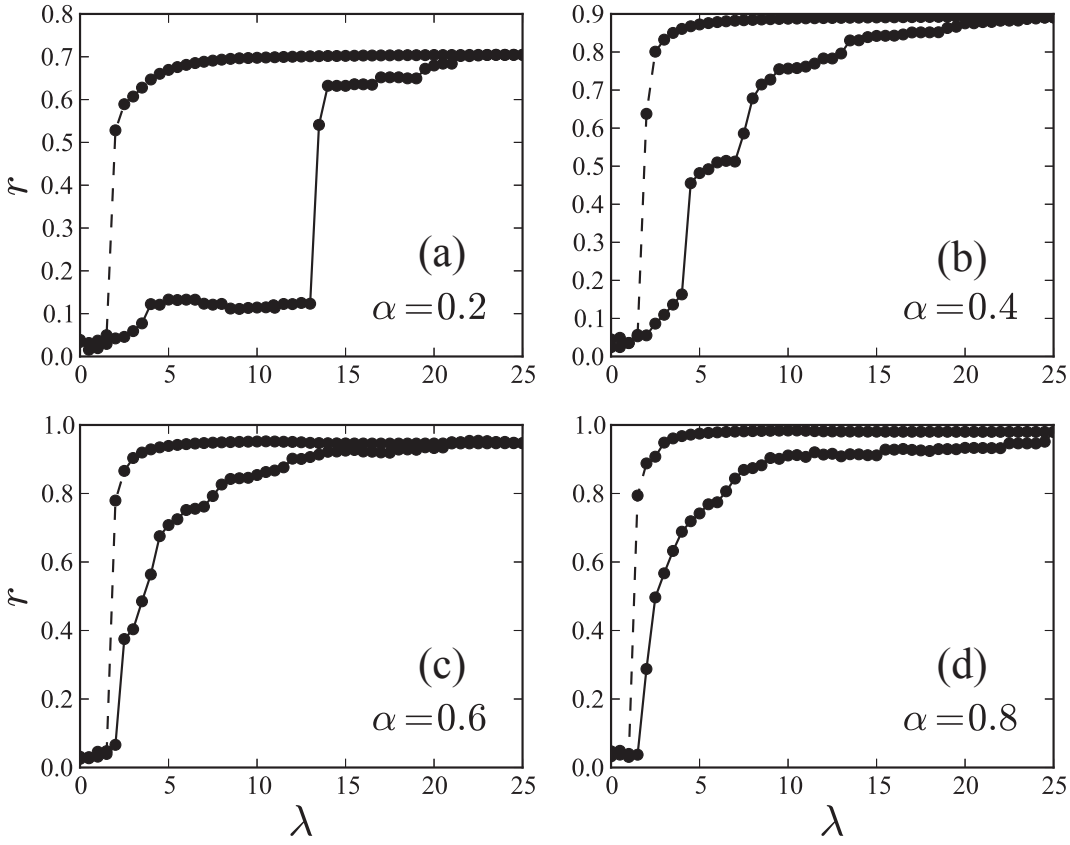

Figure 4.13: Synchronization diagram $r(\lambda)$ with (a) $\alpha = 0.2$, (b) $\alpha = 0.4$, (c) $\alpha = 0.6$ and (d) $\alpha = 0.8$ for assortativity $\mathcal{A} = -0.3$. With increasing α, onset of synchronization and hysteresis decrease. The natural frequency of each oscillator is $\Omega_i = k_i - \langle k \rangle$ and the networks have $N = 10^3$ and $\langle k \rangle = 6$. The degree distribution follows a power-law $P(k) \sim k^{-\gamma}$, where $\gamma = 3$. Curves in which points are connected by solid lines (resp. dashed lines) correspond to the forward (resp. backward) continuations of the coupling strength λ.

probability p, one new edge connects the first and the second node and another new edge links the third and fourth nodes. In the case when one of the two new edges already exists, the step is discarded and a new pair of edges is chosen. This same heuristic can also generate disassortative networks ($\mathcal{A} < 0$) with only a slight change in the algorithm. After selecting the four nodes and sorting them with respect to their degrees, one must rewire, with probability p, the highest degree node with the lowest one and, likewise, the second and third nodes. After rewiring the network, if the degree of assortativity is higher or smaller than the designed $\mathcal{A}$, p is decreased or increased respectively and the network is rewired following the procedures described above. In order to avoid dead loops, the increasing and decreasing steps of p should not be equally spaced.

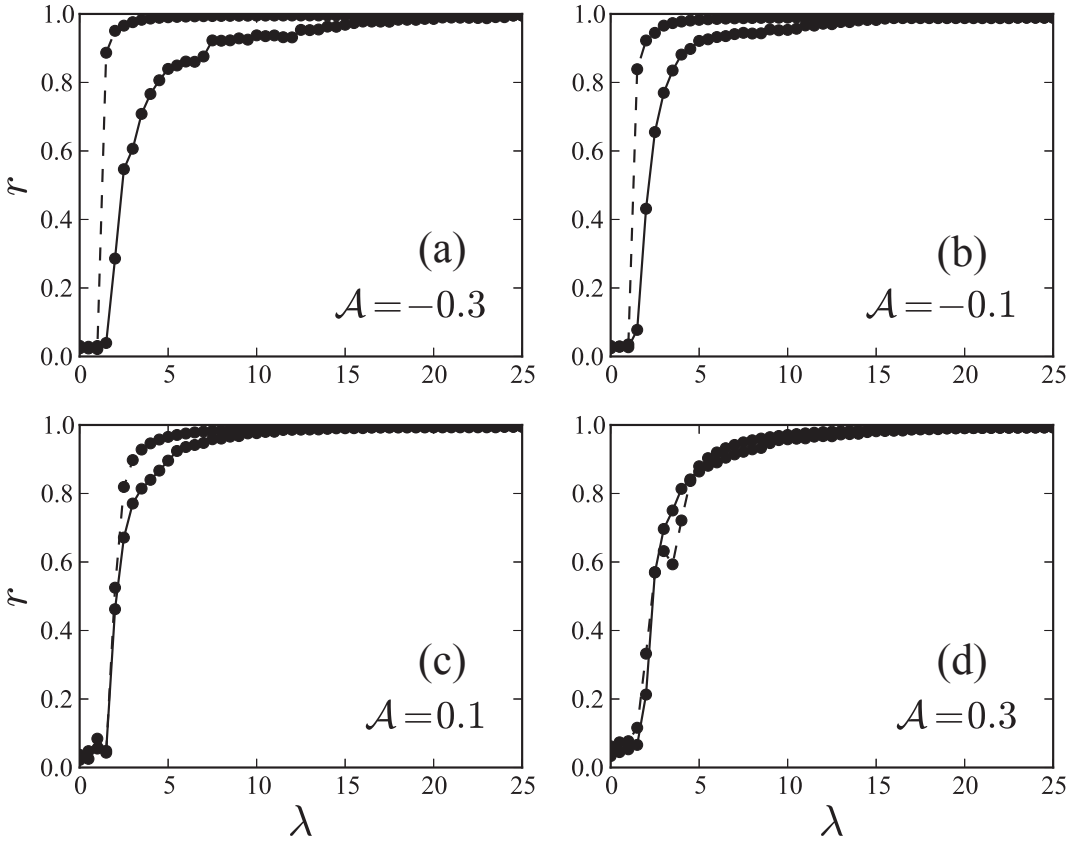

Figure 4.14: Synchronization diagram $r(\lambda)$ for (a) $\mathcal{A} = -0.3$, (b) $\mathcal{A} = -0.1$, (c) $\mathcal{A} = 0.1$ and (d) $\mathcal{A} = 0.3$. The dissipation coefficient is fixed at $\alpha = 1$ with natural frequencies given by $\Omega_i = k_i - \langle k \rangle$, as in Fig. 4.13. All networks considered have $N = 10^3$, $\langle k \rangle = 6$ and $P(k) \sim k^{-\gamma}$, where $\gamma = 3$.

4.3.2 Numerical Results

In this section we present the results obtained by numerically evolving the equations of motions considering Eq. (2.1) in assortative networks constructed according to the model described in the previous section. In all simulations the initial networks are constructed through the Barabási-Albert (BA) model with $\langle k \rangle = 6$ and $N = 1 \times 10^3$.

The order parameter r is calculated with forward and backward continuations of the coupling strength λ. More specifically, by increasing the value of λ adiabatically, we integrate the system long enough and calculate the stationary value of r at each coupling $\lambda_0, \lambda_0 + \delta\lambda, ..., \lambda_0 + n\delta\lambda$. Similarly, for the backward continuation, we start at the value $\lambda = n\delta\lambda + \lambda_0$ and decrease λ by amounts of $\delta\lambda$ until $\lambda = \lambda_0$. In both processes we use $\delta\lambda = 0.5$.

We investigate the dependency of the hysteresis on the dissipation parameter α. Fig. 4.13 shows the forward and backward synchronization diagrams $r(\lambda)$ for networks with assortativity $\mathcal{A} = -0.3$, but different values of α within the interval

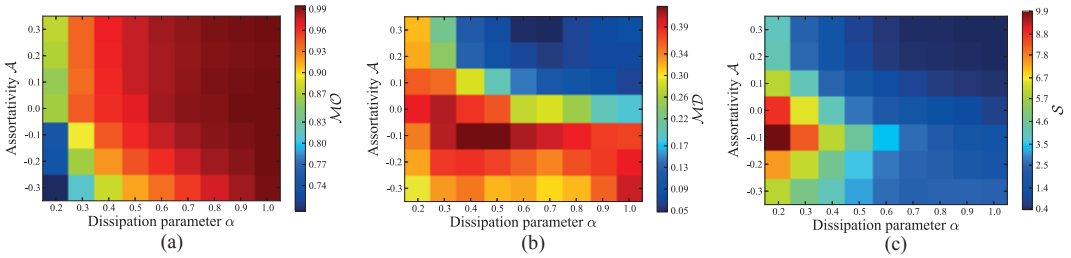

Figure 4.15: Contour plot on α-$\mathcal{A}$ plane colored according to (a) the maximal order parameter $\mathcal{MO}$, (b) the maximal order parameter difference $\mathcal{MD}$ and (c) the hysteresis area $\mathcal{S}$. $\mathcal{A}$ and α are varied within the interval $[-0.3, 0.3]$ and $[0.2, 1]$, respectively. For each pair $(\alpha, \mathcal{A})$, 40 times simulations are performed with the coupling strength in the interval as in Fig. 4.13, i.e, $\lambda \in [0, 25]$.

$[0.2, 1]$. As we can see, the area of hysteresis and the critical coupling for the onset of synchronization in the increasing branch tends to decrease as α is increased, which also contributes to increase the maximal value of the order parameter.

Next, we fix the dissipation coefficient $\alpha = 1$ and vary the network assortativity in the interval $[-0.3, 0.3]$. Fig. 4.14 shows the synchronization diagram $r(\lambda)$ for networks with different values of assortativity. As $\mathcal{A}$ increases, the hysteresis becomes less clear and the onset of synchronization in the decreasing branch tends to increase. Surprisingly, the critical coupling of the increasing branch for the second-order Kuramoto model is weakly affected, which is in sharp contrast with results concerning models without inertia (Liu et al., 2013; Li et al., 2013). More precisely, in the first-order Kuramoto model with frequencies correlated with degrees, the critical coupling for the onset of synchronization in scale-free networks increases as the network becomes more assortative (Li et al., 2013; Liu et al., 2013). The same phenomenon was observed in the synchronization of FHN oscillators (Chen et al., 2013).

In order to evaluate more accurately the dependency of the synchronization transitions on the level of assortativity and the dissipation parameter, we introduce the maximal order parameter $\mathcal{MO}$, the maximal order parameter difference $\mathcal{MD}$, and the hysteresis area $\mathcal{S}$ in the synchronization diagrams as a function of $\mathcal{A}$ and α, respectively, as follows:

$$\mathcal{MO} = \langle \max\left(r(\lambda)\right) \rangle \,, \tag{4.30}$$

$$\mathcal{MD} = \left\langle \max |r^{\mathrm{I}}(\lambda) - r^{\mathrm{D}}(\lambda)| \right\rangle , \tag{4.31}$$

$$\mathcal{S} = \left\langle \int |r^{\mathrm{I}}(\lambda) - r^{\mathrm{D}}(\lambda)| d\lambda \right\rangle , \tag{4.32}$$

where $\lambda \in [\lambda_0, \lambda_0 + n\delta\lambda]$, $\langle . \rangle$ denotes the average of different realizations, and $|\,.\,|$ the absolute value. $r^{\mathrm{I}}(\lambda)$ and $r^{\mathrm{D}}(\lambda)$ are the order parameters for increasing and decreasing coupling strength λ, respectively. If $r(\lambda)$ increases as λ grows, then $\mathcal{MO}$ is usually obtained at the maximal coupling strength $\lambda_0 + n\delta\lambda$, i.e., $\mathcal{MO} = r(\lambda_0 + n\delta\lambda)$. $\mathcal{MD} \in [0, 1]$ quantifies the hysteresis difference. If the system shows a continuous phase transition with a perfect match between increasing and decreasing coupling strength diagrams, then $\mathcal{S} \simeq 0$. In this way, S is a quantitative index to evaluate the hysteretic behavior related to the emergence of synchronization.

Comparing Figs. 4.13 and 4.14 we observe a clear dependence of the synchronization diagrams on the assortativity $\mathcal{A}$ and on the dissipation parameter α. Moreover, note that it is also possible to obtain similar dependencies of r on λ by selecting different values of α and $\mathcal{A}$. In order to better grasp this apparent equivalence in the dynamical behavior of the system for different choices of the parameters $\mathcal{A}$ and α, we show in Fig. 4.15 the quantities defined in Eqs. (4.30), (4.31) and (4.32) as a function of α and $\mathcal{A}$. As we can see in Fig. 4.15(a), similar values for the maximal order parameter $\mathcal{MO}$ are obtained according to the initial setup of the model. More specifically, the

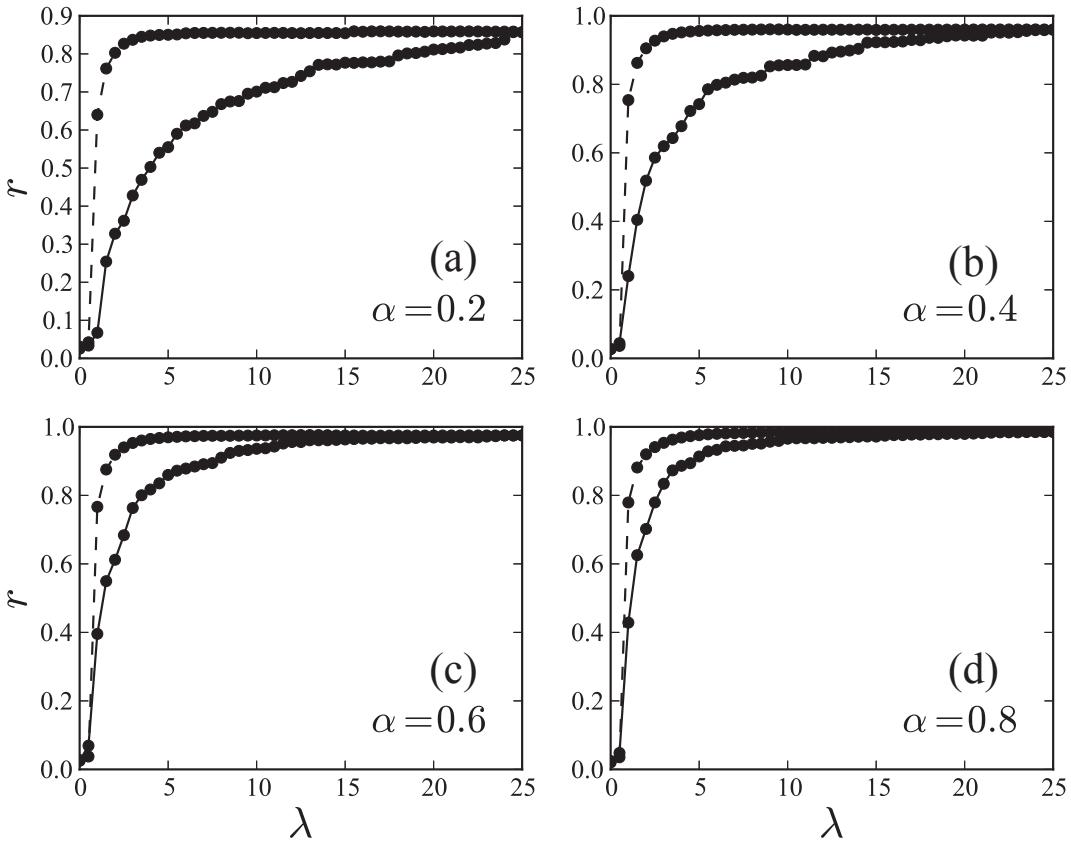

Figure 4.16: Parameters are the same as in Fig. 4.13, except that the natural frequencies are randomly selected from a Lorentzian distribution $g(\Omega) = 1/(\pi(1 + \Omega^2))$.

level of synchronization of the network can be chosen by tuning the assortativity or the dissipation parameter in the dynamical model. Therefore, for the second-order Kuramoto model in the case of frequencies positively correlated with degree, high levels of coherent behavior are obtained by either strongly assortative or disassortative networks, once the dissipation parameter α is properly selected. Interestingly, the maximal gap between the increasing and decreasing branches quantified by $\mathcal{MD}$ (Fig. 4.15(b)) has a maximum around $\mathcal{A} \simeq -0.1$ and $\alpha \in [0.4, 0.5]$, showing that the area of metastability in the stability diagram of the model (Ji et al., 2013) is maximized for this set of parameters.

A similar effect can also be observed for the hysteresis area $\mathcal{S}$ in Fig. 4.15(c). The maximal $\mathcal{S}$ in the synchronization diagram is reached for networks with $\mathcal{A} = -0.1$ and $\alpha = 0.2$. Furthermore, similar values of $\mathcal{S}$ are obtained by different sets of α and $\mathcal{A}$, which shows an interesting interplay between the topological parameter (assortativity) and the dynamical one (dissipation). More precisely, topological properties related to degree-degree correlations can be counterbalanced by the dissipation parameter in the dynamical model. This property could have interesting applications in the

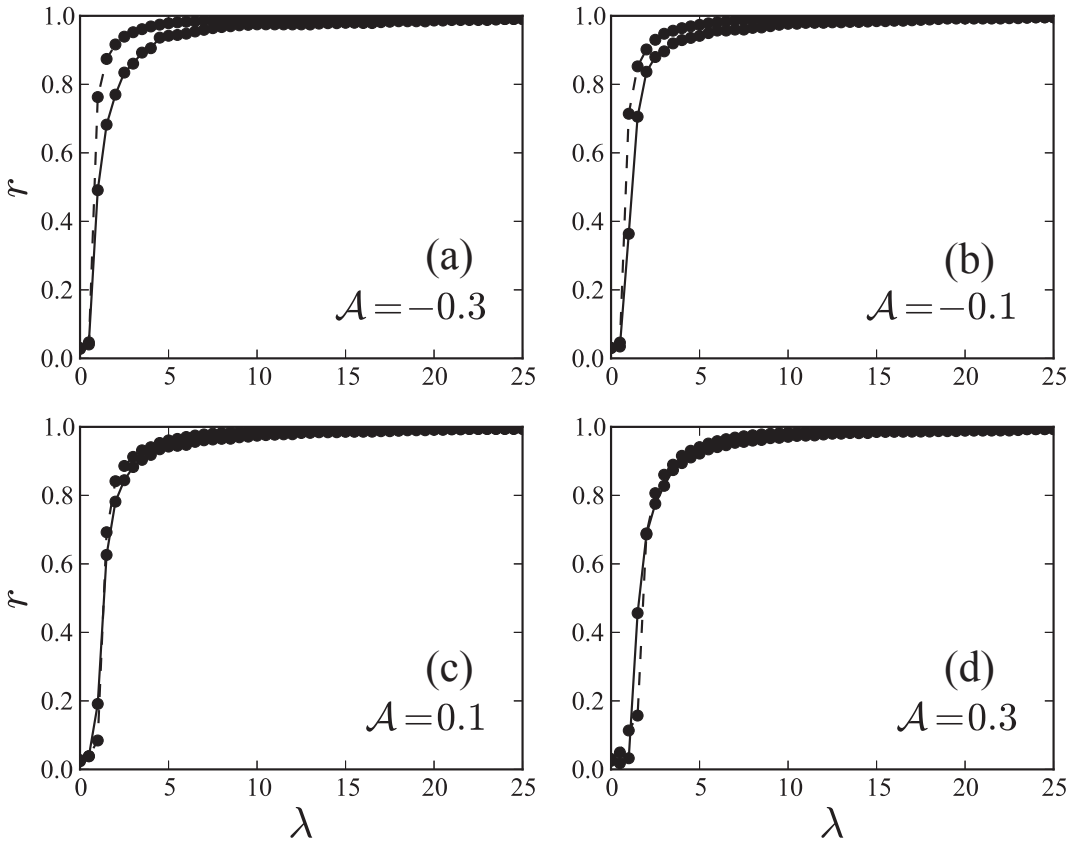

Figure 4.17: Parameters are the same as in Fig. 4.14, except that natural frequencies are randomly selected from a Lorentzian distribution $g(\Omega) = 1/(\pi(1 + \Omega^2))$.

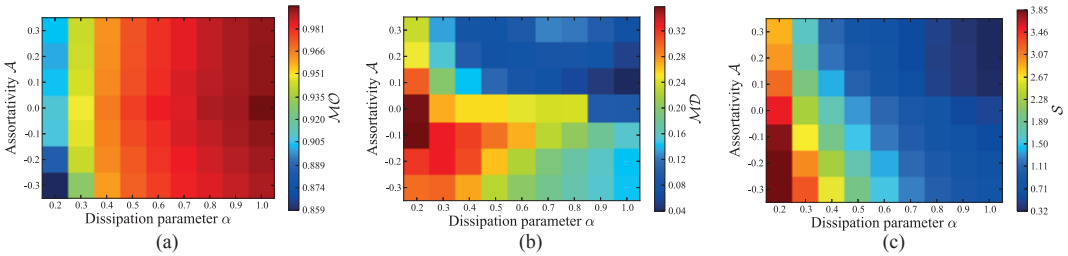

Figure 4.18: Contour plots similar as in Fig. 4.15 for networks with a natural frequency distribution given by $g(\Omega) = 1/(\pi(1+\Omega^2))$.

control of synchronization in networks modeled by the second-order Kuramoto model. In particular, if one is interested to reduce hysteresis in a system, such task can be accomplished by either increasing the dissipation or the degree mixing in the network. Therefore, the question usually addressed in studies regarding the first-order Kuramoto model that is whether assortativity could enhance synchronization or not (Zhu et al., 2013; Li et al., 2013) turns out to be harder to answer for the damped version of the model. The reason for that is that the asymptotic behavior of the system strongly depends on the combination of parameters $\mathcal{A}$ and α, which allows at the same time much more options to control the system by tuning such parameters.

In order to analyze how assortative mixing influences the dynamics of networks of damped Kuramoto oscillators without the constraint of having $\Omega_i \propto k_i$, we also compute the same forward and backward synchronization diagrams considering a Lorentzian distribution $g(\Omega) = \frac{1}{\pi(1+\Omega^2)}$ for different values of degree assortativity $\mathcal{A}$. Similarly as before, as a first experiment, we fix the assortativity at $\mathcal{A} = -0.3$ and vary the dissipation parameter α as indicated in Fig. 4.16. Again, as we increase α the hysteresis area tends to decrease. The same effect is observed for a fixed α with varying $\mathcal{A}$, as depicted in Fig. 4.17.

Calculating $\mathcal{MO}$ as a function of α and $\mathcal{A}$ we note, however, a slightly different dependence compared to the case where frequencies are proportional to degree. As we can see in Fig. 4.18(a), for a fixed value of α, $\mathcal{MO}$ is weakly affected by the change of the degree mixing, except for the case $\alpha = 0.2$. Nonetheless, the model with frequencies correlated with degrees presents larger fluctuations for the maximum value of coherent behavior, comparing Figs. 4.15(a) and 4.18(a). Furthermore, the maximum value of $\mathcal{MD}$ [Fig. 4.18(b)] for Lorentzian frequency distributions is obtained for slightly disassortative networks with low values of the dissipation parameter α. We also note that, for large α, the maximum gap $\mathcal{MD}$ starts to decrease, in contrast to the case with frequencies correlated with degree (Fig. 4.15(b)), where $\mathcal{MD}$ is close to zero for almost the entire range considered of α for which $\mathcal{A} > 0$. Finally, analyzing $\mathcal{S}$ in Fig. 4.18(c) we note the same interplay between topological perturbations in the networks, accounted for by changes in assortative mixing, and dynamical features in the oscillator model characterized by the dissipation parameter α. As shown in this figure, similar values of S are achieved by controlling the parameters α and $\mathcal{A}$, and

highly and poorly hysteretic synchronization diagrams can be obtained by different strategies, i.e., changing the network structure ($\mathcal{A}$) or the dynamical nature of the oscillators (α).

4.4 Conclusions

First-order synchronization transitions for the Kuramoto model in complex networks have been known as a consequence of positive correlation between network structure, represented by the degree distribution, and the intrinsic oscillatory dynamics, represented by the natural frequency distribution of the oscillators (Coutinho et al., 2013; Leyva et al., 2012; Peron and Rodrigues, 2012a; Gómez-Gardenes et al., 2011).

We have shown that the cluster explosive synchronization happens in the second-order Kuramoto model presenting a correlation between natural frequency and degree, as verified for the first-order Kuramoto model (Gómez-Gardenes et al., 2011). The synchronization diagram exhibits a strong hysteresis due to the different critical coupling strengths for increasing and decreasing coupling strength. As a function of the coupling strength, we have derived self-consistent equations for the order parameter. Furthermore, the projection of the phase transition on the parameter space of a pendulum has enabled the derivation of the analytical expression of the synchronized boundaries for increasing and decreasing coupling strength. We have solved the self-consistent equation and the synchronized boundaries simultaneously, and the analytical results have been compared to the simulations and both show a good agreement. Moreover, following the same process, numerically and analytically, we have shown that the onset of synchronization for increasing coupling strength decreases with increasing scaling exponents but the onset of synchronization for decreasing coupling strength keeps constant.

Following the previous processes, we have simulated the model on Watts-Strogatz networks and found a counter-intuitive phenomenon in which phase coherence decreases with the rewiring probability p. The order parameter and average frequency of each cluster have also been investigated for small and large p respectively.

To evaluate the robustness of abrupt transitions against the degree-correlated natural frequency, an additional quenched disorder is included. Numerically and analytically, we have shown that phase coherence and abrupt transitions decrease with the increasing of the strength of the quenched disorder. The hysteresis in scale-free networks with different scaling exponents has also been investigated here, but the underlying mechanism for the occurrence of hysteresis in scale-free networks remains open.

Additionally, we have numerically shown that such transitions for the second-order Kuramoto model also depend on the degree mixing in the network connection. More precisely, discontinuous transitions of networks of second-order Kuramoto oscillators can take place not only in disassortative ones but also in assortative ones, in contrast to what have been observed for the first-order Kuramoto model in which the correlation between topology and dynamics is also present (Li et al., 2013).

The reason behind this phenomenon can be regarded as an effect of the dynamical equivalence of changes in the network structure, played by assortative mixing, and changes in the oscillator model (dissipation parameter). In other words, a given final configuration of a network of second-order Kuramoto oscillators can be achieved by tuning the network structure or by adjusting the dissipation related to the phases' movement. As previously mentioned, this finding can have important applications on controlling network synchronization where, for instance, there are costs associated to lead the system to a given desirable state, allowing the adoption of different strategies to accomplish such a task.

Our results show that the hysteretic behavior of the order parameter vanishes for some assortativities, suggesting that the transition might become continuous. However, to properly determine the nature of the phase transition, a more detailed study should be addressed. Moreover, the theoretical description of sychronization in correlated networks is still an open problem and mean-field theories that account for degree-degree correlations should also be developed.

What we learn from the emergence of cluster explosive synchronization is that inertia affects the onset of synchronization of different clusters and, to enhance synchronization, one could increase the coupling strength, vary the value of the dissipation parameter, or tune the degree mixing in the network connection. As a future study, it would be interesting to further analyze the present model relating the recent approaches on mean-field approximation of first-order Kuramoto oscillators in assortative networks (Restrepo and Ott, 2014) and the low-dimensional behavior of the second-order model (Ji et al., 2014b). The impact of topology on dynamics with more sophisticated correlation patterns between local structure and natural frequencies as well as the formulation of the model considering networks of stochastic oscillators (Sonnenschein and Schimansky-Geier, 2012) are subjects for further work.

Chapter 5

Basin stability on complex networks

5.1 Introduction

Phase transition towards synchronization, as an important emergence of collective behaviors, has been widely studied in the last two decades taking advantage of the recent theory of complex networks (Arenas et al., 2008; Boccaletti et al., 2006). More recently, abrupt transitions have attracted much attention, since the discovery of a discontinuous percolation was reported in random (Achlioptas et al., 2009) and scale-free networks (Cho et al., 2009; Radicchi and Fortunato, 2009), even the explosive percolation transition was proven to actually be continuous (Riordan and Warnke, 2011; Costa et al., 2010).

In the context of abrupt transitions, hysteresis was presented in terms of initial conditions (Gómez-Gardenes et al., 2011; Leyva et al., 2012; Peron and Rodrigues, 2012b; Ji et al., 2013). Therefore, depending on the strength of perturbations being suffered, the system will either regain an equilibrium state or diverge. Linear stability analysis has been applied to characterize local stability using Lyapunov exponents (Pikovsky et al., 2003), but this is only valid for small perturbations. By considering also large perturbations, Menck et al. (Menck et al., 2013; Menck et al., 2014) proposed basin stability ($\mathcal{BS}$), which is a non-local and nonlinear concept and easily applicable to high-dimensional systems, based on the basin of attraction (Ott, 2006). $\mathcal{BS}$ is quantified as the ability to regain an equilibrium state after being subjected to perturbations and so regarded as a stability metric of the stable equilibrium. However, an analytical study of $\mathcal{BS}$ is very hard because the boundary of the basin of attraction of a general nonlinear dynamical system is usually too difficult to be discerned.

In this chapter, we start by investigating $\mathcal{BS}$ of a single oscillator (Chiang, 2011; Strogatz, 2014) derived in Sec. 5.2.1 and analytically approximate $\mathcal{BS}$ in Sec. 5.2.2. In Sec. 5.2.3, we substantially investigate $\mathcal{BS}$ of the synchronization of a second-order Kuramoto model in complex networks. We demonstrate a novel phenomenon that there are two first-order transitions occurring successively: an *onset transition* from instability to local stability and a *suffusing transition* from local to global stability. We call this sequence *onset-suffusing transitions*. By combining a mean-field approach with a basin stability derivation, we provide an analytical treatment. The analytical results are in good agreement with the simulations.

In terms of small networks, in section 5.3.1, we attempt to explain the basic dynamics using the classical model of the single oscillator. We investigate its parameter space using basin stability. A stable fixed point and a stable limit cycle coexist in the bistable area. Basin stability is used to characterize the parameter space not only in one oscillator but also in a two-node and a four-node topology as shown in section 5.3.2 and 5.3.3 respectively. The coexistence could also be found in a four-node topology using basin stability. Finally, conclusions are shown in section 5.4.

Some of the findings presented here have been published in (Ji and Kurths, 2014a; Ji and Kurths, 2014b; Ji et al., 2015)

5.2 Onset and suffusing transitions towards synchronization

5.2.1 Mean-field theory

We start with the second-order Kuramoto model in the following general form (2.1) (Ji et al., 2013; Rohden et al., 2012; Tanaka et al., 1997a; Acebrón and Spigler, 1998; Tanaka et al., 1997a; Menck et al., 2014). Although, the following mean-field approximation is similar to that of section 4.2, we will show the full analytical process to avoid misunderstanding.

Following the random graph model proposed in (Chung and Lu, 2002), under the assumption that the degrees of vertices are uncorrelated, given the degree sequence $\{k_i\}$ with expectation degree of vertex i as k_i, the probability of the edge between nodes i and j is $A_{ij} = k_i k_j / \sum_j k_j$ (Sonnenschein and Schimansky-Geier, 2012; Ichinomiya, 2004; Chung and Lu, 2002), which implies that the degree of oscillator i is equal to the expected number of adjacent oscillators, i.e. $k_i = \sum_j A_{ij}$. Substituting this approximation into Eq. (2.1), the coupling term becomes $\lambda k_i \sum_j k_j \frac{\sin(\theta_j - \theta_i)}{N\langle k\rangle}$, where $\langle k\rangle$ denotes the average degree. Following (Ichinomiya, 2004), the order parameter is defined

$$re^{\mathbf{i}\psi} = \sum_j \frac{k_j e^{\mathbf{i}\theta_j}}{N\langle k\rangle}, \tag{5.1}$$

where r is the magnitude, ψ the average phase and $\mathbf{i}$ is the imaginary unit. Its continuum limit version is shown before as Eq. (4.5). $r \in [0, 1]$ is qualified to measure the phase coherence of the network. In particular, $r \approx 0$ and $r = 1$ correspond with fully incoherent and fully synchronous state respectively. Multiplying both sides of Eq. (5.1) by $e^{-i\theta_i}$ and substituting the imaginary part into Eq. (2.1), we rewrite Eq. (2.1) in terms of the mean-field quantities (r, ψ) as follows:

$$\ddot{\theta}_i = -\alpha\dot{\theta}_i + \Omega_i + \lambda k_i r \sin(\psi - \theta_i). \tag{5.2}$$

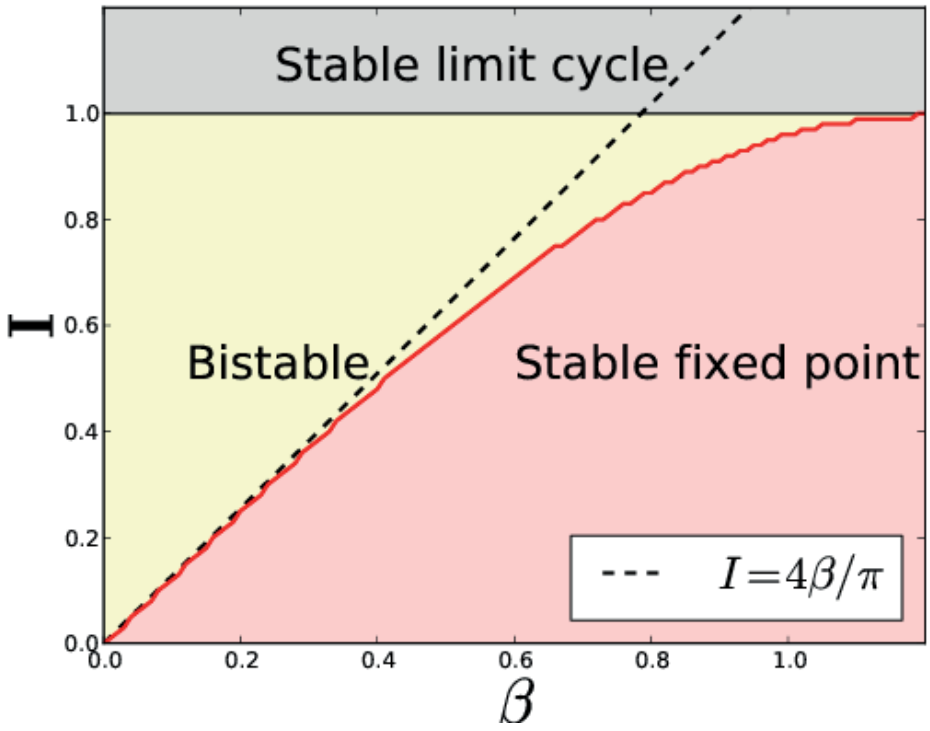

Figure 5.1: The stability diagram of a single oscillator with three regions: the limit cycle (grey), the stable equilibrium (red), and bistability (both limit cycle and stable equilibrium coexist) (yellow). The homoclinic bifurcation curve is tangent to the line $I = 4\beta/\pi$, as $\beta \to 0$.

5.2.2 Basin stability on a single oscillator

Towards understanding of the stability of the mean field Eq. (5.2), we start with a single oscillator (Chiang, 2011; Strogatz, 2014) with:

$$\ddot{\theta} = -\alpha\dot{\theta} + \Omega - \lambda \sin(\theta), \tag{5.3}$$

where λ is a parameter. It can be seen that when $\lambda = \lambda k_i r$, $\Omega = \Omega_i$ and $\psi = 0$, Eq. (5.3) becomes Eq. (5.2). For convenience, we set $\omega \equiv \dot{\theta}$. Eq. (5.3) is topologically invariant. Nodes with the same λ and Ω belong to the same set, but its stationary state might vary depending crucially on initial condition if within the region of bistability. We consider $\Omega > 0$. When $\Omega < \lambda$ and $\alpha > 0$, Eq. (5.3) possesses two equilibria: a stable equilibrium $(\theta_1^*, \omega_1^*) = (\arcsin(\Omega/\lambda), 0)$ and an unstable saddle $(\theta_2^*, \omega_2^*) = (\pi - \arcsin(\Omega/\lambda), 0)$, restricted within the range of $\theta \in [-\pi, \pi]$.

The stability diagram of the single oscillator with a unit coupling strength was fully investigated (Strogatz, 2014). Hence, we change the time scale of Eq. (5.3) to $\tau = \sqrt{\lambda}t$ (Strogatz, 2014), which yields

$$\frac{d^2\theta(\tau)}{d^2\tau} = -\beta\frac{d\theta(\tau)}{d\tau} + I - \sin(\theta(\tau)), \tag{5.4}$$

where $\beta = \alpha/\sqrt{\lambda}$ and $I = \Omega/\lambda$. The stability diagram is shown in Fig. 5.1 in terms of the parameter pair (β, I). A time-independent Melnikov function (Guckenheimer and Holmes, 1983) depending on the parameters (β, I) follows

$$M(\beta, I) = 2\pi I - 8\beta. \tag{5.5}$$

A homoclinic bifurcation occurs at $M(\beta, I) = 0$ (Guckenheimer and Holmes, 1983) with the homoclinic bifurcation line tangent to the line of $I = 4\beta/\pi$ when β is close to 0 (Guckenheimer and Holmes, 1983; Strogatz, 2014). This implies that the system is bistable with the stable fixed point (θ_1^*, ω_1^*) and a limit cycle when $4\beta < \pi I$; Otherwise, if $4\beta > \pi I$, (5.4) converges to the stable equilibrium under any large perturbation, i.e. the stable equilibrium is globally stable. In the grey region, the oscillator attracts to the stable limit cycle.

It is sufficient and convenient to investigate Eq. (5.3) instead of Eq. (5.2) without loss of generality. The following energy function for the system (Strogatz, 2014; Chiang, 2011)

$$E(\theta, \omega) = F(\omega) + U(\theta), \tag{5.6}$$

which is the same as in Eq. (2.10) (see section 2.1.3) and where $F(\omega) = (1/2)\omega^2$ is the kinetic energy function and $U(\theta) = -\Omega\theta - \lambda\cos(\theta)$ is the potential energy function. It can be seen that $U(\theta)$ reaches its local minimum and maximum at $\theta = \theta_1^*$ and θ_2^* respectively. Also, $\frac{dE}{dt} = -\alpha\omega^2$ indicates that it decreases strictly, except at the two fixed points when $\alpha > 0$. Therefore, the system is indeed dissipative when $\alpha > 0$.

In the absence of dissipation, i.e., $\alpha = 0$, the total energy is static due to $\frac{dE(\theta,\omega)}{dt} = 0$, namely, a conserved quantity (Strogatz, 2014). The system either oscillates around the stable fixed point $(\theta_1^*, \omega_1^*) = (\arcsin(\Omega/\lambda), 0)$, named librations, or diverges to infinity (Strogatz, 2014) as shown in Fig. 5.2. The heteroclinic trajectories that link (θ_0^*, ω_0^*) to the saddle $(\theta_2^*, \omega_2^*) = (\pi - \arcsin(\Omega/\lambda), 0)$ depict the basin boundary of the stable equilibrium when $\alpha \approx 0$. We denote the point at the left boundary of this heteroclimic trajectory as (θ_0^*, ω_0^*), which can be calculated by the energy function. The local minimal energy lies at the stable equilibrium (θ_1^*, ω_1^*) with

$$E(\theta_1^*, \omega_1^*) = -\Omega \arcsin(\Omega/\lambda) - \lambda\sqrt{1 - \Omega^2/\lambda^2} \tag{5.7}$$

and the local maximal energy lies at the saddle (θ_2^*, ω_2^*) with

$$E(\theta_2^*, \omega_2^*) = -\Omega(\pi - \arcsin(\Omega/\lambda)) + \lambda\sqrt{1 - \Omega^2/\lambda^2}. \tag{5.8}$$

In comparison, for a dissipative system, i.e., $\alpha > 0$, since a trajectory of (5.3) starting from any initial state eventually converges to the stable equilibrium or diverges, all trajectories that converge to the stable equilibrium comprise of the basin of attraction of this stable equilibrium (Ott, 2006; Strogatz, 2014).

Based on the volume of the basin of attraction, Menck et al. (Menck et al., 2013; Menck et al., 2014) proposed the concept of basin stability ($\mathcal{BS}$) as the proportion of trajectories that converge to the stable equilibrium under suffering large perturbations(Menck et al., 2014):

$$\mathcal{BS} = \int_{-B}^{B}\int_{-\pi}^{\pi} \chi(\theta,\omega)\rho(\theta,\omega)d\theta d\omega, \tag{5.9}$$

where $\chi(\theta,\omega)$ indicates the synchronized state, $\chi(\theta,\omega) = 1$ if (θ,ω) belongs to the basin of attraction of the equilibrium or $\chi(\theta,\omega) = 0$, otherwise. $\rho(\theta,\omega)$ is the density distribution of the perturbation of (θ,ω) from $(-\pi,\pi)\times(-B,B)$, with $\int\int \rho(\theta,\omega)d\theta d\omega = 1$. $\mathcal{BS} \in [0,1]$ measures how stable the stationary state is. If $\mathcal{BS} = 0$, the equilibrium is unstable, i.e. any small perturbation can cause a permanent drift from the stationary state; on the other hand, if the stationary state is globally stable, $\mathcal{BS} = 1$ can be derived.

In what follows, we are to estimate $\mathcal{BS}$ of the equilibrium (θ_1^*, ω_1^*) by considering two extreme situations. As demonstrated in Fig. 5.3(a), its $\mathcal{BS}$ linearly grows with respect to α in the interval (α_0, α_c).

First, we treat the case that the system is weakly dissipative in terms of $\alpha \approx 0$ denoted by α_0. At a weak dissipation within the region of bistability, as shown in Fig. 5.4, the oscillator could converge to the stable fixed point if the initial conditions belong to the grey region, otherwise it attracts to the stable limit cycle. In this case, the heteroclinic trajectory can approximate the boundary of the attraction basin of the stable equilibrium. That means the basin of attraction of the stable

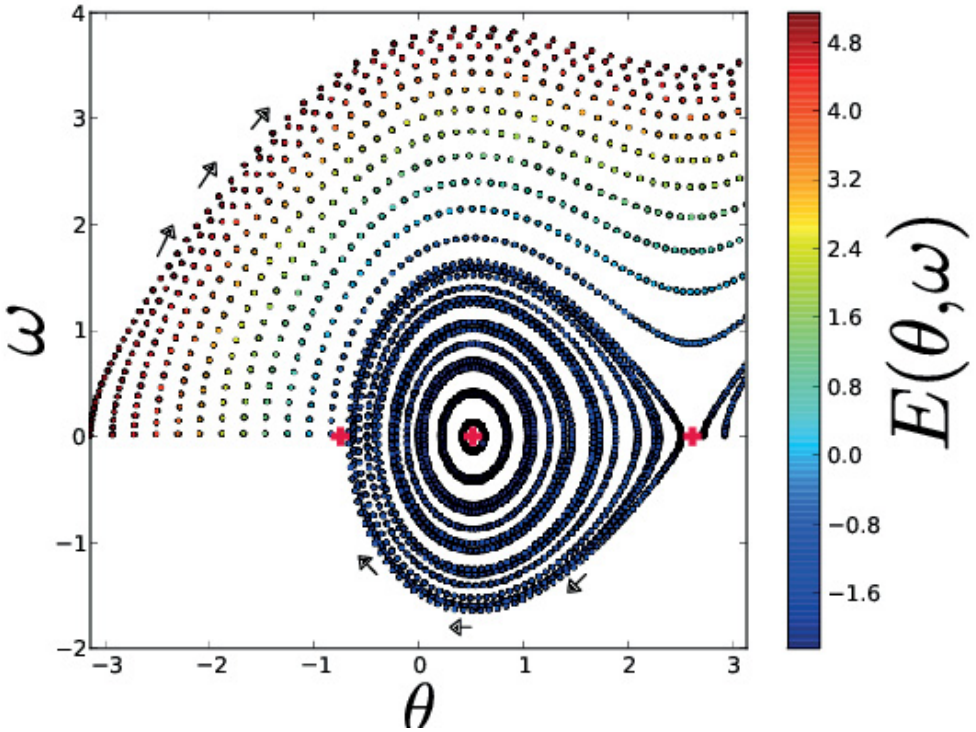

Figure 5.2: Isoenergetic curves of the single oscillator in the phase plane without dissipation with respect to the energy function (5.6). From left to right, three red cross points stands for (θ_0^*, ω_0^*), (θ_1^*, ω_1^*) and (θ_2^*, ω_2^*).

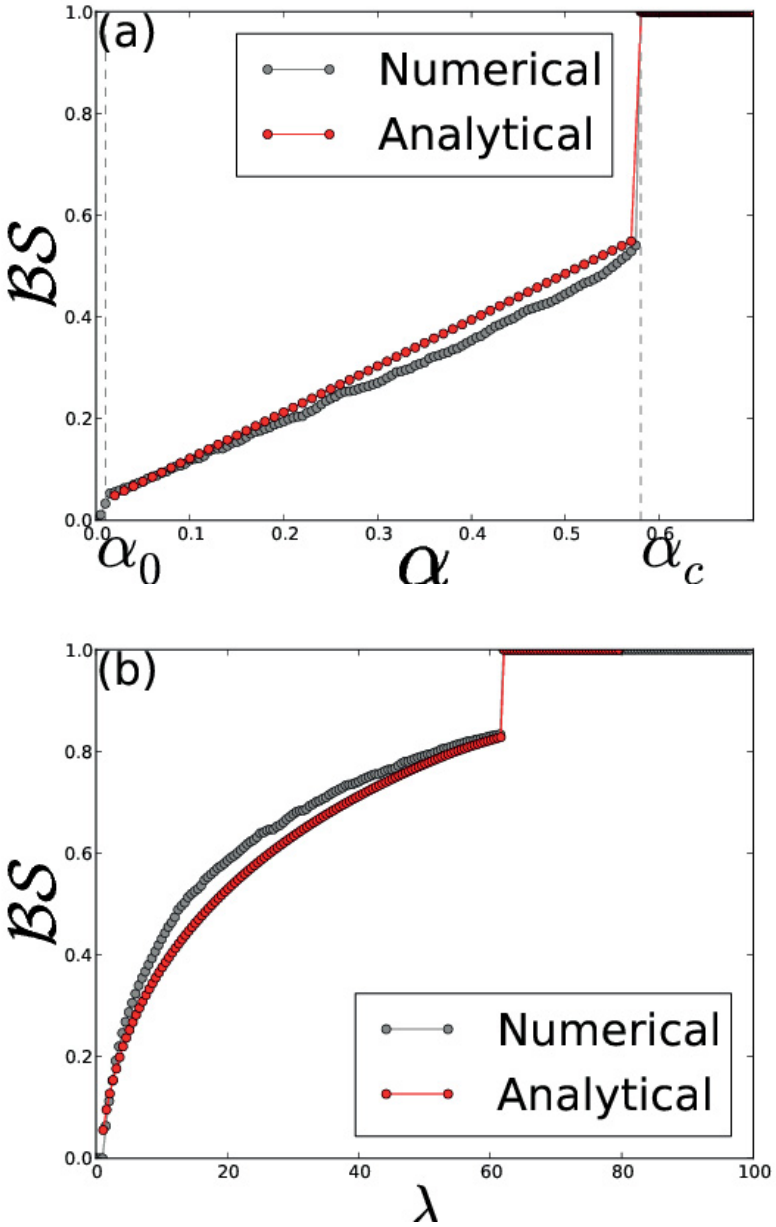

Figure 5.3: Basin stability $\mathcal{BS}$ as a function of dissipation α with $\lambda = 2$ (a) and the coupling strength λ with $\alpha = 0.1$(b). The red analytical curves are obtained from Eq. (5.14). For each pair of parameters (α, λ), the numerical values of $\mathcal{BS}$ are calculated by counting the proportion of trajectories that converge to the stable equilibrium, among the total 10^4 trajectories with initial values of (θ, ω) randomly drawn within the range $[-\pi, \pi] \times [-15, 15]$, following a uniform distribution. Each trajectory is obtained by integrating the system sufficiently long for the system to reach the stationary states. Here, we take $\Omega = 1$.

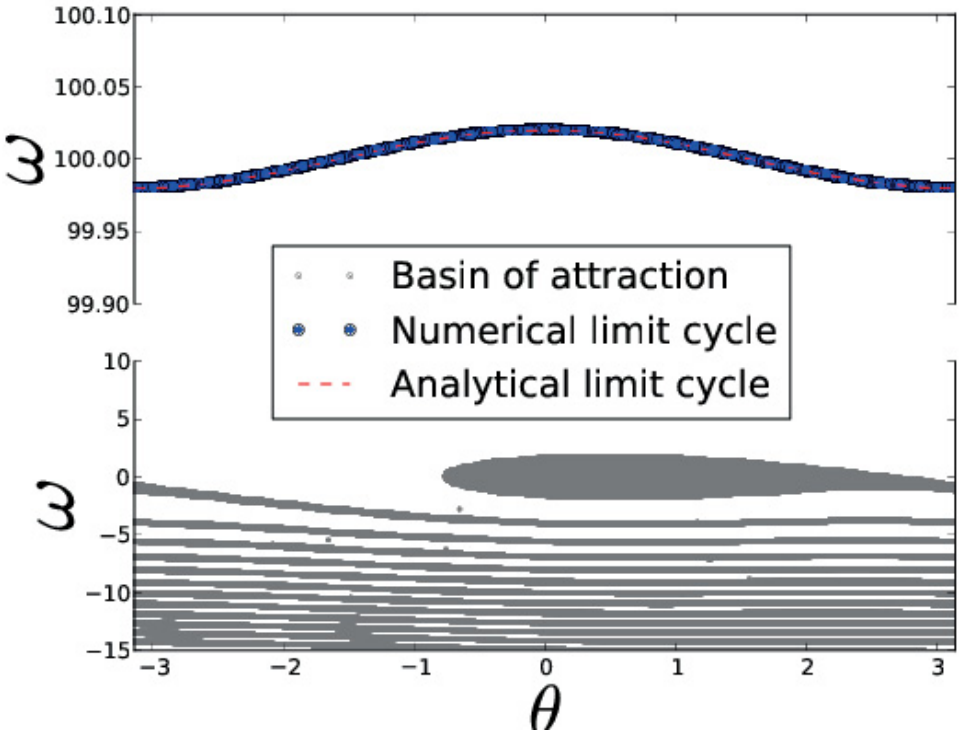

Figure 5.4: The basins of attraction of the stable equilibrium at the weak dissipation ($\alpha = 0.01$) with $\Omega = 1$ and $\lambda = 2$. The analytical solution follows Eq. (5.12).

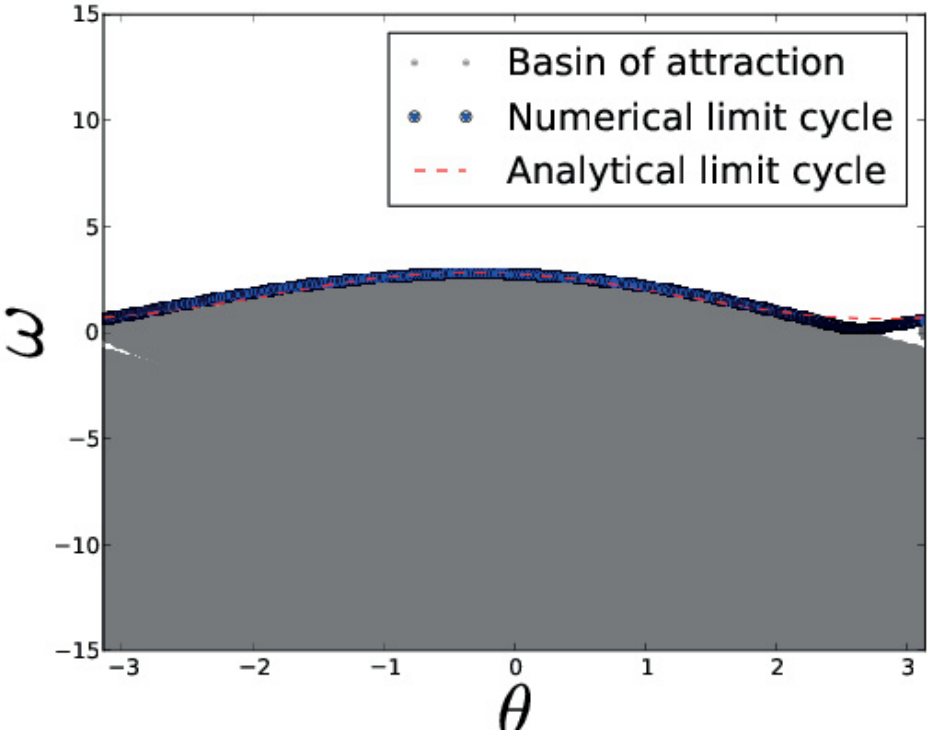

Figure 5.5: The basins of attraction of the stable fixed point at the threshold value $\alpha = 0.575$ of strong dissipation with $\Omega = 1$ and $\lambda = 2$. The analytical solution follows Eq. (5.12).

equilibrium is an ensemble of all the librations in the absence of dissipation. It has been shown that the boundary of the basin of attraction is the stable manifold of the saddle (θ_2^*, ω_2^*) (Chiang, 2011) and the energy along the trajectory is nearly static and close to that of the saddle, because $\frac{dE}{dt} = -\alpha_0\omega^2 \approx 0$. Thus, each point on the stable manifold of the saddle (θ_2^*, ω_2^*) has approximately the same energy as this saddle. Therefore, we can approximate the coordinate (θ, ω) of the basin boundary of (θ_1^*, ω_1^*) by the curve with $E(\theta, \omega) = E(\theta_2^*, \omega_2^*)$, which is composed of two parts: $\omega_\pm(\theta) = \pm\sqrt{2(\Omega\theta + \lambda\cos(\theta) + E(\theta_2^*, \omega_2^*))}$ respectively and symmetrically. If we take the perturbation (θ, ω) following the uniform distribution in the box $[-\pi, \pi]\times[-B, B]$, for $\alpha_0 \ll 1$, $\mathcal{BS}$ could be approximately calculated by the area between $\omega_\pm(\theta)$ as

$$\mathcal{BS}(\alpha_0, \Omega, \lambda) = \int_{\theta_0}^{\theta_2^*} [\omega_+(\theta) - \omega_-(\theta)]d\theta/(4B\pi), \tag{5.10}$$

where θ_0 is the solution of $\sqrt{2(\Omega\theta_0 + \lambda\cos(\theta_0) + E(\theta_2^*, \omega_2^*))} = 0$ with $\theta_0 \neq \theta_2^*$.

Second, the stability diagram of Eq. (5.3) depends on the parameter pair (β, I) with $\beta = \alpha/\sqrt{\lambda}$ and $I = \Omega/\lambda$, so that the homoclinic bifurcation occurs at $4\beta = \pi I$. This implies that a small value of $\alpha/\sqrt{\lambda}$ allows the system in a region of bistability when $4\beta < \pi I$, namely, $\alpha < \alpha_c \equiv \pi\Omega/(4\sqrt{\lambda})$ (Guckenheimer and Holmes, 1983; Strogatz, 2014); Otherwise, if $4\beta > \pi I$, namely, $\alpha > \alpha_c$, (5.3) converges to the stable equilibrium under any large perturbation, i.e. the stable equilibrium is globally stable $(\mathcal{BS} = 1)$.

As α increases so that the parameter pair (β, I) is close to the homoclinic bifurcation curve, as shown in Fig. 5.5, the limit cycle approaches the saddle and coincides with the basin boundary of attracting the stable equilibrium. In this case, the upper boundary of the basin of the stable fixed point can be approximated by the curve of the stable limit cycle. Furthermore, if α increases further, the system always globally converges to the stable equilibrium.

Hereby, we consider the scenario of near this threshold α_c. When a oscillator is in the state of limit cycle, numerical simulations show that the mean frequency $\langle\omega\rangle \simeq \Omega/\alpha$, which implies that the phase dynamics of this limit cycle can be approximated as $\theta(t) \simeq \Omega t/\alpha + \theta(0)$. Let $\omega = \Omega/\alpha + f(t)$, where $f(t)$ is the residual term to be solved. Inserting this approximation into the governing Eq. (5.3) for a single oscillator yields

$$\dot{f} + \alpha f + \lambda\sin\theta = 0. \tag{5.11}$$

The specific solution to Eq. (5.11) is

$$f(t) = \frac{\lambda\alpha^2}{\alpha^4 + \Omega^2}\left(\frac{\Omega}{\alpha}\cos\theta - \alpha\sin\theta\right). \tag{5.12}$$

For convenience, we write f as $f(\theta, \alpha, \Omega, \lambda)$. To validate the approximation, simulations are conducted in Figs. 5.4 and 5.5 and the analytical solutions and the simulations match well to each other.

Interestingly, it can be seen that this limit cycle is close to the boundary of the basin of attraction of the stable equilibrium at $\alpha = \alpha_c$. Thanks to Eq. (5.12), $\mathcal{BS}(\alpha_c, \Omega, \lambda)$ can be calculated as

$$\mathcal{BS}(\alpha_c, \Omega, \lambda) = \int_{-\pi}^{\pi} \frac{\Omega/\alpha_c + f(\theta, \alpha_c, \Omega, \lambda) + B}{4B\pi} d\theta. \tag{5.13}$$

Therefore, combining Eq. (5.10) at the weak dissipation and Eq. (5.13) at the threshold, $\mathcal{BS}$ is approximated as follows

$$\mathcal{BS}(\alpha, \Omega, \lambda) = \frac{\mathcal{BS}(\alpha_0, \Omega, \lambda) - \mathcal{BS}(\alpha_c, \Omega, \lambda)}{\alpha_0 - \alpha_c}(\alpha - \alpha_0) + \mathcal{BS}(\alpha_0, \Omega, \lambda), \tag{5.14}$$

for $\alpha \in (\alpha_0, \alpha_c)$; $\mathcal{BS}(\alpha, \Omega, \lambda) = 1$ for $\alpha > \alpha_c$. The analytical curves in the panel Fig. 5.3 (a) vs. α and the panel Fig. 5.3 (b) vs. λ are in good agreement with the simulations.

5.2.3 Transitions in complex networks

In complex networks, the oscillators interact with each other via the mean-field properties (r, ψ), as formulated by Eq. (5.2). With $\lambda = \lambda k_i r$, each oscillator can be treated as a single oscillator as Eq. (5.3). Given all other parameters, the order magnitude r can be regarded as a function with respect to λ, denoted by $r(\lambda)$, as illustrated in Fig. 5.6. The low-dimensional behaviors of the first-order (Ott and Antonsen, 2008) and the second-order Kuramoto model (Ji et al., 2014b) were found to be Lorentzian. For simplicity, we take $\alpha = 1$ and the distribution of the natural frequency as the Cauchy-Lorentz distribution with the density $g(\Omega) = 1/[\pi(1 + \Omega^2)]$. In this case, oscillators with a natural frequency within the interval $[-4\sqrt{\lambda k_i r}/\pi, 4\sqrt{\lambda k_i r}/\pi]$ that imposes $1 = \alpha > \pi|\Omega_i|/(4\sqrt{\lambda})$ are in a phase synchronization regime (Ji et al., 2014b). Therefore, the self-consistent order parameter r_{k_i} of oscillators with the same degree k_i following (Ji et al., 2014b) can be derived.

With the increasing of the coupling strength, a first-order transition occurs at the onset of synchronization K_c (Risken, 1984); when $\lambda < \lambda_c$, the coupled oscillators are totally desynchronizing with $r \simeq 0$; however, when $\lambda > \lambda_c$, the order parameter r starts to monotonically increase. Given the stationary solution for r vs. λ, we find that when $\lambda < \lambda_c$, $\mathcal{BS}$ at each node is also close to 0, as illustrated in Fig. 5.6.

At $\lambda = \lambda_c$, if $|\Omega_i| < \lambda_c k_i r(\lambda_c)$, $\mathcal{BS}$ indicates that nodes with degree k_i and the natural frequency Ω_i undergo a first-order transition accordingly. This sort of first-order transition is named *onset transition*, which means a transition from an unstable ($\mathcal{BS} = 0$) to a stable synchronous state ($\mathcal{BS} > 0$). In particular, if the parameter pair (β, I) with $\beta = \alpha/\sqrt{\lambda_c k_i r(\lambda_c)}$ and $I = |\Omega_i|/(\lambda_c k_i r(\lambda_c))$ is located in the region of stable equilibrium in the stability diagram ($4\beta > \pi I$), then $\mathcal{BS}$ jumps from 0 to 1

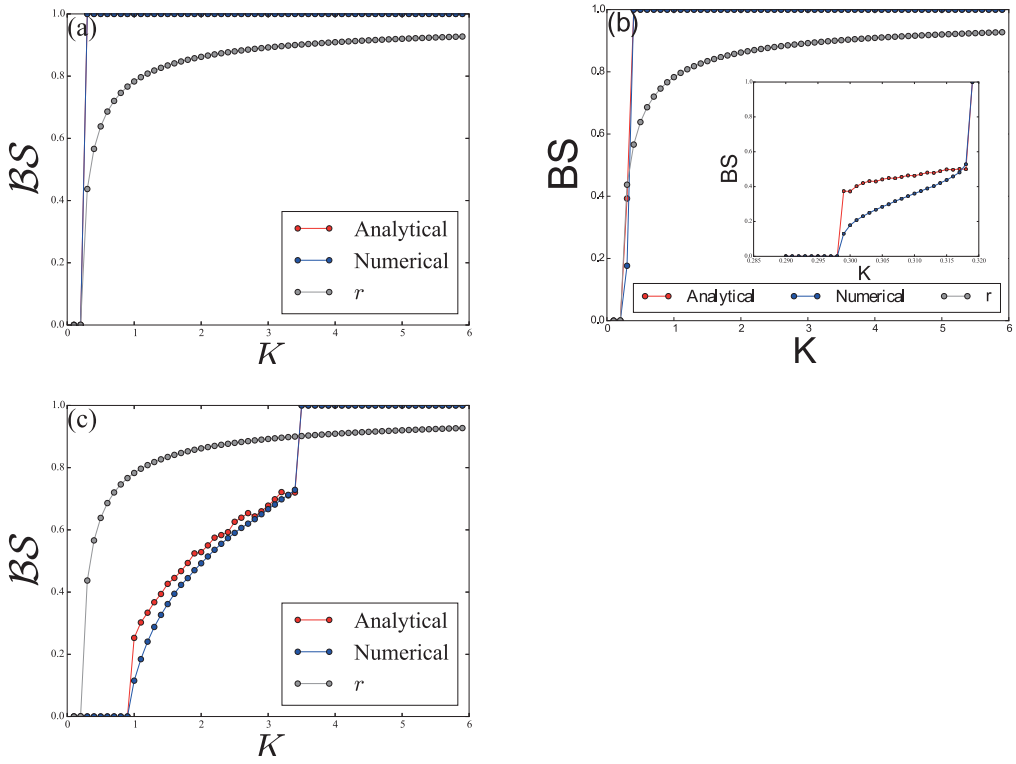

Figure 5.6: $\mathcal{BS}$ against the coupling strength λ with $\Omega_i = 0.2$ (a), $\Omega_i = 1.3$ (b) and $\Omega_i = 7.0$ (c). The simulations are implemented on scale-free networks with $N = 10000$, $P(k) \propto k^{-3}$ and $k > 4$. Numerical values of $\mathcal{BS}$ are calculated by counting the proportion of trajectories that converge to the stable equilibrium, among the total 10^4 trajectories with initial values of (θ, ω) randomly drawn within the range $[-\pi, \pi] \times [-15, 15]$. Analytical solutions are obtained from Eq. (5.14). Here, we consider nodes with degree 10.

directly, as illustrated in Fig. 5.6(a). With higher $r(\lambda_c)$, more nodes have the onset transition at λ_c.

In comparison, if the parameter pair (β, I) with $\beta = \alpha/\sqrt{\lambda_c k_i r(\lambda_c)}$ and $I = |\Omega_i|/(\lambda_c k_i r(\lambda_c))$ with degree k_i is located in the bistable region ($4\beta < \pi I$), the onset transition occurs with $\mathcal{BS}$ jumping from 0 to $\mathcal{BS}(\alpha, |\Omega_i|, \lambda_c k_i r(\lambda_c))$, which is less than 1. Then, increasing λ will trigger the other first-order transition when $\lambda = \lambda_c'$ for the other critical value. In this case, $\mathcal{BS}$ jumps to 1, as shown in Fig. 5.6(b), when the parameter pair $(\alpha/\sqrt{\lambda k_i r}, |\Omega_i|/(\lambda k_i r))$ crosses the homoclinic bifurcation curve. In the case of $\alpha/\sqrt{\lambda k_i r} \ll 1$, this critical value $\lambda_c' = \frac{|\Omega_i|^2\pi^2}{16\alpha^2 k_i r}$ can be calculated by the Melnikov's analysis (Guckenheimer and Holmes, 1983). This sort of first-order transition is named *suffusing transition*, which means a transition from a locally ($0 < \mathcal{BS} < 1$) to globally stable state ($\mathcal{BS} = 1$), which is in fact a homoclinic bifurcation of the system (5.2). Here, we observe the novel phenomenon that the *onset* and *suffusing transitions* occur successively with respect to the increasing coupling strength. We call this sequence *onset-suffusing transitions*.

With a large natural frequency $|\Omega_i| > \lambda_c k_i r(\lambda_c)$, $\mathcal{BS}$ of nodes with degree k_i increases with increasing coupling strength. When $|\Omega_i| \leq \lambda k_i r$, the nodes become stable. When the coupling strength is further increased, the suffusing transition occurs at $(\alpha/\sqrt{\lambda k_i r}, |\Omega_i|/(\lambda k_i r))$ crossing the homoclinic bifurcation curve with $\mathcal{BS}$ jumping to 1, as shown in Fig. 5.6(c). When $\lambda k_i r$ is higher than but close to $|\Omega_i|$, as shown in Fig. 5.6(b-c), the analytical results are slightly larger than the simulations, because in this case $\mathcal{BS}$ is concave upward with positive slopes instead of linearly increasing within (α_0, α_c).

When $|\Omega_i| < \lambda_c k_i r(\lambda_c)$, the order parameter r can identify the onset transition as shown in Fig. 5.6(a)-(b), which coincides with the basin stability. However, since r is a global index that is dominated by the nodes with low natural frequencies, r cannot reflect the synchronization transition characteristic of these nodes with high natural frequency. As shown by Fig. 5.6(c), the onset transition of node with $|\Omega_i| > \lambda_c k_i r(\lambda_c)$ does not coincide with that of r. Moreover, the suffusion transition cannot be disclosed by r, either.

The simulations are conducted with the increment step equal to 0.1 of the coupling strength λ. For each λ, we overlap 10^4 times of random perturbations of the initial values of (θ, ω) within the range of $(\theta, \omega) \in [-\pi, \pi] \times [-15, 15]$ following a uniform distribution. For each overlap of perturbation, we integrate the system, for a sufficiently long duration, for example, 10^5, so that the distribution of the state of the oscillator approaches a stationary distribution. Combining with the self-consistent equation as in (Ji et al., 2014b), we can analytically estimate $\mathcal{BS}$ by Eq. (5.14), regarded as a function with respect to the coupling strength and the natural frequency. As Fig. 5.6 shows, analytical and numerical results are in a good agreement.

5.3 Basin stability on small networks

5.3.1 Projection on the parameter space

Defining the relative size of the volume of basin of attraction as basin stability $\mathcal{BS} \in [0, 1]$, a new non-local and nonlinear measure was recently proposed to quantify how stable the synchronous sate is against even large perturbations (Menck et al., 2013; Menck et al., 2014). To estimate the basin stability of a stable fixed point in case of single machine infinite bus system, we randomly select 25000 initial values of $(\theta, \dot{\theta})$ from $[-\pi, \pi] \times [-10, 10]$, integrate the system long enough and then count the percentage of initial values reaching a stable fixed point.

According to the stability diagram of a single oscillator as shown in figure 5.1 (Ji et al., 2014b; Ji et al., 2013; Strogatz, 2014; Ji et al., 2015), a stable fixed point and a stable limit cycle coexist in the bistable area. Whether the system will evolve to the fixed point or to the limit cycle depends crucially on the initial conditions. When parameter values are located in the limit cycle area (resp. stable fixed point area) $\mathcal{BS}$ is 0 (resp. 1). Shown in figure 5.4 is the phase space for a set of parameter values corresponding to the bistable area in fig. 5.1. The system has one stable fixed point $\theta_f = \arcsin(\Omega/\lambda)$ for $0 < \Omega < \lambda$, and one saddle $\theta_s = \pi - \theta_f$. The basin of attraction of the stable fixed point θ_f is colored gray and that of the stable limit cycle is colored white. The saddle is located on the right side of the stable fixed point at the intersection between the basin of attraction of θ_f and $\dot{\theta} = 0$ line.

In figure 5.7, we project the basin stability $\mathcal{BS}$ over the parameter space of the single oscillator for $\lambda = 1$. As can be observed from figure 5.3, basin stability increases with α in the bistable area, and then jumps to unity when α crosses the homoclinic bifurcation line $\alpha = \frac{\Omega\pi}{4\sqrt{\lambda}}$ (Strogatz, 2014). It is also evident that one can use basin stability to locate the homoclinic bifurcation line as the locus of the points where basin stability $\mathcal{BS}$ becomes unity for the first time when α is incremented gradually from 0 to 1.

5.3.2 Two oscillators

What happens if the network is a set of two or more nodes? Consider first two oscillators, out of which one is a generator with $\Omega_g = +\Omega$ and one consumer with $\Omega_c = -\Omega$, the dynamics is governed by

$$\ddot{\theta}_g = -\alpha\dot{\theta}_g + \Omega + \lambda \sin(\theta_c - \theta_g), \tag{5.15}$$

$$\ddot{\theta}_c = -\alpha\dot{\theta}_c - \Omega + \lambda \sin(\theta_g - \theta_c). \tag{5.16}$$

The phase difference $\delta\theta = \theta_g - \theta_c$ satisfies

$$\delta\ddot{\theta} = -\alpha\delta\dot{\theta} + 2\Omega + 2\lambda \sin(-\delta\theta), \tag{5.17}$$

which is the same as the equation of motion of the single oscillator. Following the same process as in section 5.3.1, we investigate the dynamics of the two oscillators.

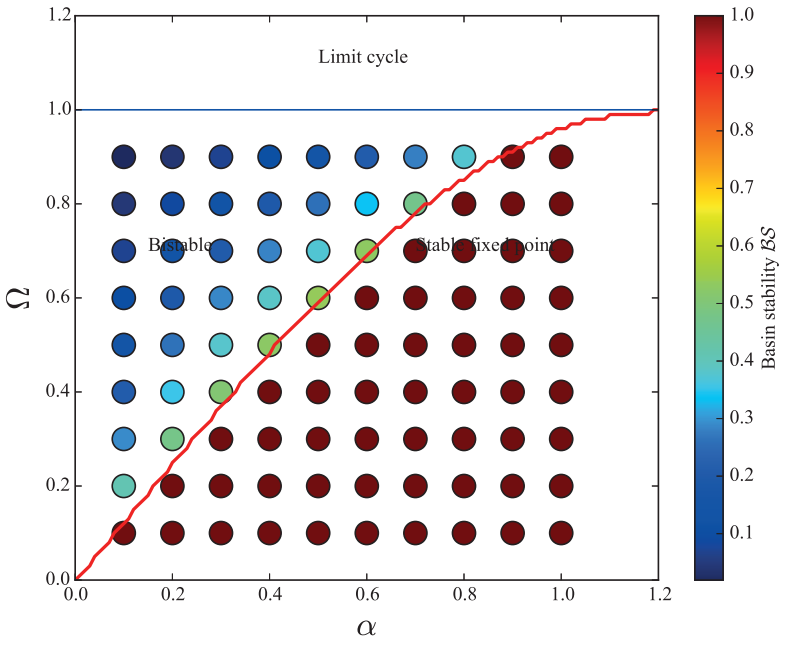

Figure 5.7: Basin stability over parameter space of the single oscillator. The different areas same as shown the figure 5.1 are separated by the two lines: $\Omega/\lambda = 1$ and the homoclinic bifurcation line. When $\alpha \to 0$, the bifurcation line is tangent to the line $\alpha = \Omega\pi/(4\sqrt{\lambda})$. For fixed coupling strength $\lambda = 1$, basin stability $\mathcal{BS}$ is calculated over the parameter space by varying the value of α and Ω from 0 to 1 separately.

For $\Omega > \lambda$, the oscillators converge to one stable limit cycle which oscillates around Ω/α. For $\frac{4\alpha\sqrt{\lambda}}{\pi} < \Omega < \lambda$, there could be one stable limit cycle and one stable fixed point at

$$\delta\theta = \arcsin(\Omega/\lambda), \tag{5.18}$$

which depends on initial conditions of $\delta\theta$ and $\delta\dot{\theta}$. Fig. 5.1 illustrates the coexistence of the stable limit cycle and the stable fixed point. Also basin stability $\mathcal{BS}$ decreases with increasing λ from $\frac{4\alpha\sqrt{\lambda}}{\pi}$ to λ for fixed α and λ. For $\lambda < \frac{4\alpha\sqrt{\lambda}}{\pi}$, only one stable fixed point exists with basin stability $S = 1$.

5.3.3 Four oscillators

In section 5.3.1 and section 5.3.2, we have shown the coexistence of a stable limit cycle and a stable fixed point in a single oscillator and in the two-oscillators topology respectively. Further, basin stability has been used to quantify how stable the fixed point is. What happens when the number of the nodes is increased by 2? Here we focus on the nonlinear stability of four-node topology ranging from a basic ring network with two generators separated by two consumers of fig. 5.8(a) to the network of globally-coupled phase oscillators of fig. 5.8(d).

The 4-nodes model takes the following form in the simplest case:

$$\ddot{\theta}_i = -\alpha\dot{\theta}_i + \Omega_i + \lambda\sum_{j=1}^{4} A_{ij}\sin(\theta_j - \theta_i). \tag{5.19}$$

In order to compare the parameter space of a medium-dimensional dynamical system with that of the single oscillator, we vary the values of α and Ω for fixed coupling strength $\lambda = 1$. In figure 5.9, we show basin stability over the parameter space of α and Ω for the networks combining two generators with $\Omega_{G1} = \Omega_{G2} = \Omega$ and two consumers with $\Omega_{C1} = \Omega_{C2} = -\Omega$ as shown in fig. 5.8.

Instead of perturbing only one oscillator (Menck et al., 2013), in this paper, we perturb all oscillators and then calculate basin stability. In order to assess basin stability, we randomly select for each pair of α and p initial values of $(\theta,\dot{\theta})$ from $[-\pi, \pi] \times [-15, 15]$, integrate the system long enough and then find the percentage of initial values reaching the synchronized state. For every pair of α varying from 0 to 2 with 0.05 interval and Ω varying from 0 to 2 with the same gap, we repeat the same process to calculate the basin stability and then sketch the parameter space as shown in fig. 5.9. This way we find that there are three different regions namely a stable limit cycle, bistability and a stable fixed point. Comparing the parameter space of fig. 5.9(a) and (d), we see that the volume of the bistable area decreases as the network becomes more connected.

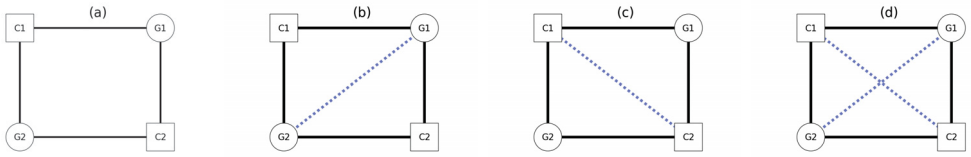

Figure 5.8: Connection of 2 generators ($G1$ and $G2$) and 2 consumers ($C1$ and $C2$). Squares denote consumers and circles represent generators. (a) Two generators fully connect to 2 consumers, but the two generators or the two consumers are not connected directly. In configuration (b) (resp. (c)), the two generators (resp. consumers) are also connected with one additional dashed blue diagonal line. (d) Both generators and consumers are fully connected with two additional dashed diagonal lines.

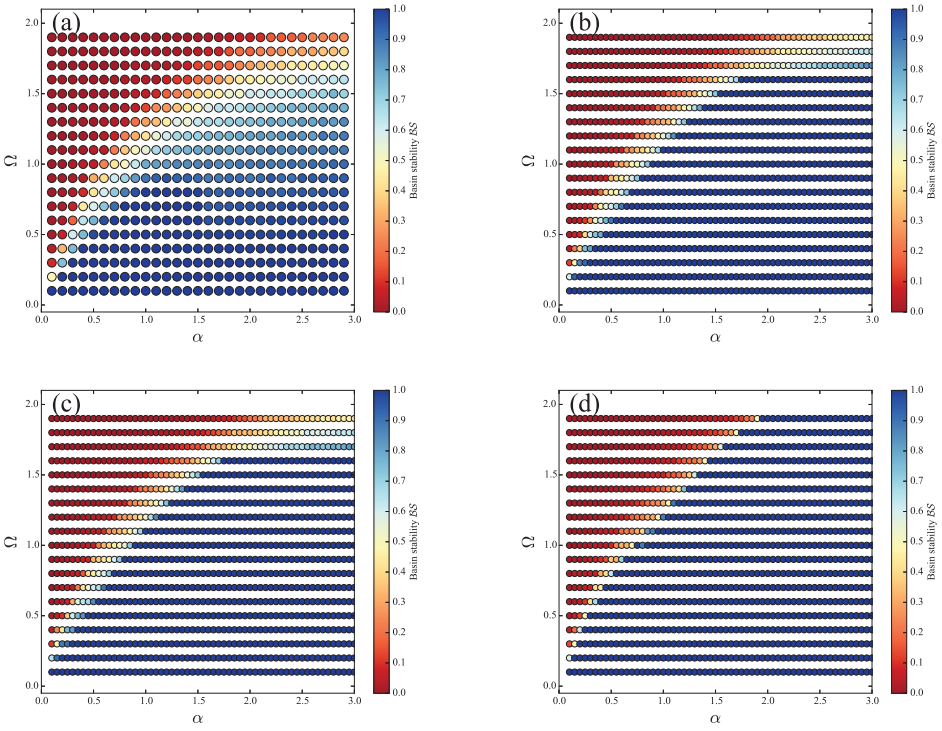

Figure 5.9: The panels show basin stability over the parameter space of α and Ω for $\lambda = 1$ for the networks corresponding to fig. 5.8. Comparing the parameter space of (a) and (d), we can see that the volume of the bistable area decreases as the network becomes more connected.

5.4 Conclusions

In term of the volume of the basin of attraction, basin stability is quantified to measure the system's ability to regain an equilibrium state subjected to perturbations. We have demonstrated the novel phenomenon uncovered by the basin stability that two first-order transitions occur successively in a second-order Kuramoto model in complex networks: *an onset transition* from instability to local stability and *a suffusing transition* from local to global stability; we call this sequence *onset and suffusing transitions*. We have presented analytical analysis of this phenomenon by a mean-field approach and the theoretical results show a good agreement with the simulations. Our findings enhance the understanding of the stability of microscopic mechanisms towards synchronization and its application complement the stability theory of complex network dynamical systems. Moreover, the transitions uncovered by the basin stability can be applied to, e.g. 'heal' dead ends to enhance power grid stability (Menck et al., 2014), any dynamical system with hysteresis loop and elsewhere (Rohden et al., 2012; Acebrón and Spigler, 1998; Tanaka et al., 1997b; Tanaka et al., 1997a).

Parameter values and the size of a disturbance are two crucial factors to determine the stability of nonlinear power systems. Motivated by the question of how stable a state is, basin stability was proposed based on the volume of the basin of attraction. We have evaluated the basin stability for a one-node system and a four-node network. Basin stability has been projected over the parameter space not only for the 2 dimensional system but also for medium dimensional dynamical system. This study illustrates a new way of investigating the stability even for high dimensional systems.

Chapter 6

Partial basin stability and its applications

6.1 Introduction

Complex networked systems, such as the human brain, power grids, in general exhibit mulstability and have more than one attractor. For each attractor, its basin of attraction, an ensemble of initial conditions that approach to this attractor as time increases, plays an important role in understanding its corresponding stability (Nusse and Yorke, 1996). In realistic situations in networks, a certain degree of perturbations are largely unavailable. Depending on which basin of attraction the system lies in after being perturbed, the qualitative behavior of the system could be fundamentally different varying from one desired state to unpredicted ones.

Stability analysis is a crucial point and is of highest actual importance from various aspects (economy, future society, sustainability, etc.) (Machowski et al., 2011; Buldyrev et al., 2010). Many previous efforts were devoted to evaluate the stability given small and large perturbations. With a small perturbation, master-stability function (Pecora and Carroll, 1998) could be used to identify the coupling-parameter region for identical oscillators with linear coupling terms. To complement such linear-stability paradigm, basin stability, a non-local and nonlinear method, was profound in Refs (Menck et al., 2013; Menck et al., 2014) based on the volume of the basin of attraction and it indicates the likelihood that *the whole system* returns to a stationary state under large perturbations. The method therein is proposed especially for global synchronization.

Besides global synchronization, partial (cluster) synchronization is playing a more important role in the understanding of dynamics of complex systems (Pecora et al., 2014), e.g. it is momentous in brain networks (Schnitzler and Gross, 2005). At each cluster, knowledge of the attracting basins can not account for the functional role of the cluster as shown in Fig. 6.1. It is of paramount importance that perturbations to one cluster can affect other clusters, potentially inducing all clusters change behavior. Therefore, in order to account for the specific characteristics of partial synchronization, we here introduce the concept of *partial basin stability*, and we focus on the single but fundamental property: the stability influence between clusters. The stability influence interprets how likely the cluster m returns to the desired state after any perturbation on the cluster a. To the best of our knowledge, the concept has not

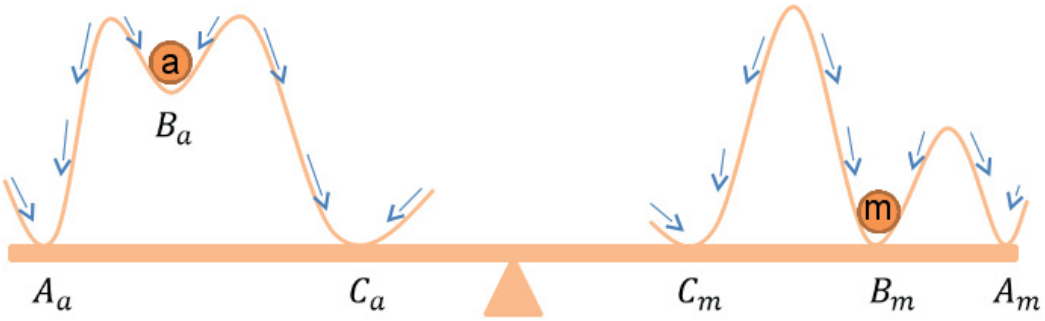

Figure 6.1: Thought experiment: Balls on the seansaw. Two tracks with balls a and m are located on the two sides of the seesaw. Each track has 3 stable fixed points labeled A_a, B_a and C_a (or A_m, B_m and C_m). The location of one ball perturbs the other one, potentially causing it to change the stationary state. Arrows indicates the direction of balls after perturbations. If a is perturbed from B_a to A_a, m would roll from B_m to C_m to keep the balance on the seesaw.

yet been employed. We denote partial basin stability from cluster a to cluster m by $\mathcal{PBS}_{a\to m}$.

We will start in Section 6.2 by formulating the general form of the new concept of partial basin stability. We substantially implement the new concept on neural networks in section 6.3 and power grids in section 6.4. In section 6.5, we conclude our results.

All sections are novel contributions of this thesis.

6.2 Partial basin stability: general formulation

Consider a general nonlinear dynamical system that is formulated by the following ordinary differential equation

$$\dot{x} = f(x), \tag{6.1}$$

where $x \in \mathbb{R}^n$ is the state vector and $f : \mathbb{R}^n \to \mathbb{R}^n$ stands for the evolution law. The state vector x is partitioned into several component vectors $x^a \in \mathbb{R}^{n_a}$, $a = 1, \cdots, N$, with $\sum_{a=1}^{N} n_a = n$. Then, system (6.1) can be rewritten as

$$\dot{x}^a = f_a(x^1, \cdots, x^N),\ a = 1, \cdots, N \tag{6.2}$$

where $f_a : \mathbb{R}^n \to \mathbb{R}^{n_a}$ is the evolution law at component a with $f = [f_1^\top, \cdots, f_N^\top]$. The interaction from components a to m can be described as $\partial f_m / \partial x^a$: if it equals to zero, then we say that there is no interaction from a to m. For simplicity, we denote by $x^{\mathscr{I}} = [{x^1}^\top, \cdots, {x^{a-1}}^\top, {x^{a+1}}^\top, \cdots, {x^N}^\top]^\top$ the vector composed of the components excluding x^a.

Towards depicting the interaction from a perturbation of component x^a to the dynamics of x^m, in the present paper, we propose a novel definition named *partial attractor*, which describes the attraction of component a towards m. In detail, let $\mathscr{A}_m$ be a subset in $\mathbb{R}^{n_m}$. Given the initial values of $x^{\mathscr{J}}(0) = x_0^{\mathscr{J}}$, if $\mathscr{A}^m$ attracts $x^m(t)$ under the perturbation of x^a, namely,

$$\lim_{t\to\infty} dist(x^m(t), \mathscr{A}_m) = 0$$

for initial values $x(0) = x_0$ with $x_0^{\mathscr{J}}$ fixed but x_0^a perturbed, where $dist(\cdot,\cdot)$ denotes the Hausdorff distance in $\mathbb{R}^{n_m}$, then we call $\mathscr{A}_m$ *partial attracting set* (of x^m) of the perturbation of x^a given the initial values $x_0^{\mathscr{J}}$. We denote it as $\mathscr{A}_m|x_0^{\mathscr{J}}$. The attraction can be defined in diverse senses, for instance, in the sense of Lyapunov, Milnor and SBR (Alexander et al., 1992). If this partial attracting set is forward invariant under the perturbation of x_0^a and minimum (among all these invariant and attracting sets), then we call it a *partial attractor* from components a to m given initial values $x_0^{\mathscr{J}}$.

Consider a partial attractor $\mathscr{A}_m|x_0^{\mathscr{J}}$. Now we extend the concept of basin stability proposed in (Menck et al., 2013; Menck et al., 2014) to *partial basin stability* that quantifies the probability that a component vector $x^m(t)$ returns to the attracting set $\mathscr{A}_m$ under the perturbation of the initial value of x_0^a and given the initial values of others, i.e. $x_0^{\mathscr{J}}$. Hereby, we define the partial basin stability $\mathcal{PBS}_{a\to m}(\mathscr{A}_m|x_0^{\mathscr{J}})$ as follows

$$\mathcal{PBS}_{a\to m}(\mathscr{A}_m|x_0^{\mathscr{J}}) = \int 1_{\mathscr{A}_m}(x_0)\rho_a(x_0^a)\delta_{x_0^{\mathscr{J}}}(x^{\mathscr{J}})dx_0, \tag{6.3}$$

where $1_{\mathscr{A}_m}(x_0)$ is an indicator function of the asymptotic dynamics of $x(t)$ such that $1_{\mathscr{A}_m}(x) = 1$ if $x^m(t)$ converges to $\mathscr{A}_m$ as $t \to \infty$ with given initial values x_0 and $1_{\mathscr{A}_m}(x_0) = 0$, otherwise; $\rho_a(x_0^a)$ is the density of the initial value of x^a in the state subspace $\mathbb{R}^{n_a}$; $\delta_\cdot(\cdot)$ stands for the Dirac-Delta.

It can be seen that partial basin stability measures the likelihood that a component x^m returns to the desired state $\mathscr{A}_m$ under the perturbation of component x^a, which follows the density $\rho_a(\cdot)$, but, given all other initial values. So, $\mathcal{PBS}_{a\to m} = 1$ indicates that the component m is global stable at $\mathscr{A}_m$ with respect to perturbations on x^a; $\mathcal{PBS}_{a\to m} = 0$ means that the component m is relatively unstable, i.e., even a very small perturbation on x^a can trigger x^m to depart from $\mathscr{A}_m$.

In the scenarios of networked systems, partial basin stability can serve to quantitatively evaluate the local influence in terms of stability between nodes or between communities (or clusters). We should highlight that there is an essential difference between partial basin stability and the concept arising in (Menck et al., 2013; Menck et al., 2014). In (Menck et al., 2013; Menck et al., 2014), the authors quantified the influence of node dynamics to the dynamics of the whole network which can be regarded as a projection of basin stability on the subspace of one node. However, we focus here on the local interaction between nodes (groups) and disregard the dynamics of other components $x^{\mathscr{J}}$ except x^m, towards understanding the directed

interacting influence of dynamics between two nodes/groups.

Partial basin stability $\mathcal{PBS}_{a\to m}(\mathscr{A}_m|x_0^{\mathscr{J}})$ is calculated by numerical integration using Monte Carlo methods. Given initial values of $x_0^{\mathscr{J}}$, choose M_a times of initial values x_0^a independently and randomly following the density $\rho_a(\cdot)$; then, generate M_a realizations of the trajectory of $x(t)$, denoted by $X_k(t)$, $k = 1, \cdots, M_a$ up to a sufficiently long time T; count the number of $X_m(t)$, of which the m-th component converges to the desired state $\mathscr{A}_m$, denoted by $S_{a\to m}$; finally, partial basin stability can be numerically approximated by:

$$\mathcal{PBS}_{a\to m}(\mathscr{A}_m|x_0^{\mathscr{J}}) \approx S_{a\to m}/M_a.$$

In particular, when $a = m$, $\mathcal{PBS}_{a\to a}$ is termed as *self-loop stability* of the node a.

In what follows, we implement the concept of partial basin stability on two significant applications: neural networks and power grids.

6.3 Neural networks

6.3.1 Kuramoto model with synaptic plasticity

The human brain, as a typical example of cluster synchronization, is an assemble of functionally specialized clusters, and its remarkable processing capabilities rest on local communications within and long-range communication between clusters (Schnitzler and Gross, 2005). Therefore, it would be particularly useful to the directed interaction influence between neural clusters in terms of the probability that the desired state of a cluster is preserved under perturbations on other subnetworks.

We mimic oscillations of the brain network by the first-order Kuramoto model with synaptic plasticity (Maistrenko et al., 2007). This network comprises of $N = \sum_{a=1}^{M} 5 \times N_a$ nodes, which is divided into M subnetworks, named *regions*. Each region a has $5 \times N_a$ oscillators. Among them, $4N_a$ oscillators are excitatory, described as:

$$\begin{aligned}\dot{\theta}_i^a = \omega_i^a &+ \sum_{m=1}^{M} \frac{\lambda^{a,m}}{4N_m} \sum_{j}^{5N_m} \Delta(j) K_{ij}^{a,m} \sin(\theta_j^m - \theta_i^a) \\ &- \frac{1}{N_a} \sum_{j}^{5N_a} (1 - \Delta(j)) K_{ij}^{a,a} \sin(\theta_j^a - \theta_i^a),\end{aligned} \tag{6.4}$$

and N_a are inhibitory oscillators, described as:

$$\begin{aligned}\dot{\theta}_i^a = \omega_i^a &+ \frac{1}{4N_a} \sum_{j}^{5N_a} \Delta(j) K_{ij}^{a,a} \sin(\theta_j^a - \theta_i^a) \\ &- \frac{1}{N_a} \sum_{j}^{5N_a} (1 - \Delta(j)) K_{ij}^{a,a} \sin(\theta_j^a - \theta_i^a),\end{aligned} \tag{6.5}$$

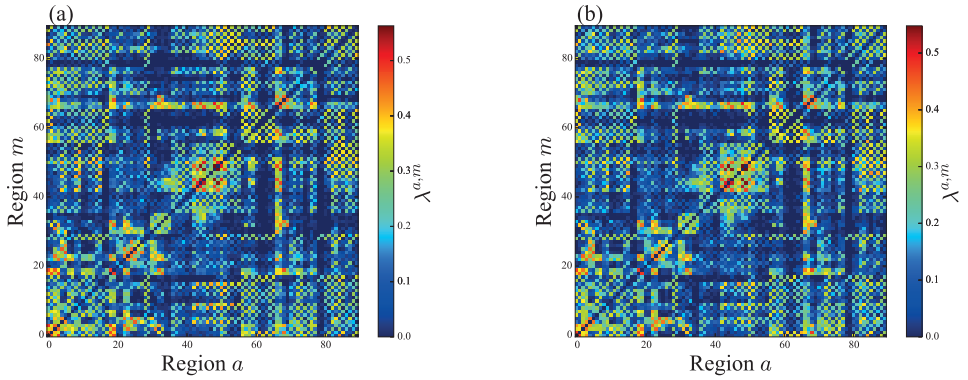

Figure 6.2: Average fiber link densities $\lambda^{a,m}$ by DTI between regions a and m in groups of (a) healthy control and (b) schizophrenia.

where ω_i^a indicates the intrinsic frequency of the oscillator i in the region a, $K_{i,j}^{a,m}$ indicates the coupling between the oscillators i and j, respectively, within the regions a and m, and $\lambda^{a,m}$ indicates the coupling strength between a and m. The excitation and inhibition of oscillators are identified by the indicator $\Delta(\cdot)$: if j is excitatory, $\Delta(j) = 1$ and $\Delta(j) = 0$, otherwise. This implies that excitatory oscillators always have positive influences to other oscillators, within the same region and between regions but the influences of inhibitory oscillators are negative and restricted within the region where it is located.

The coupling strengths between oscillators subjected to the spiking time-dependent plasticity (STDP) induce the coexistence of a desynchronized and a synchronized state (Tass and Majtanik, 2006), which can be formulated as follows (Maistrenko et al., 2007):

$$\dot{K}_{i,j}^{a,m} = \begin{cases} \varepsilon(\alpha - K_{i,j}^{a,m})e^{(\theta_i-\theta_j)/\tau_p}, & : \theta_i - \theta_j \in [-\pi, 0] \\ \varepsilon(-K_{i,j}^{a,m})e^{-(\theta_i-\theta_j)/\tau_d}, & : \theta_i - \theta_j \in [0, \pi]. \end{cases} \tag{6.6}$$

It can be seen that the coupling strength $K_{i,j}^{a,m}$ is nonnegative and its upper-bound is α. Multi-stability including synchronization exists when $\tau_p \neq \tau_d$ (Maistrenko et al., 2007). Among these states, in the present paper, we investigate partial basin stability of the synchronous state.

The inter-regional connections $\lambda^{a,m}$ are defined by the mean linking density of fibers between region m and region a, measured from the magnetic resonance imaging (MRI). The brain regions follow the automated anatomical labeling (AAL) atlas (Tzourio-Mazoyer et al., 2002) and are used to parcellate the brain into 90 regions of interest (ROIs), with 45 in each hemisphere. The neuroanatomical matrix was obtained by the Diffusion Tensor Imaging (DTI) technique (Le Bihan et al., 2001). Here, we focus on two groups of subjects: schizophrenia patients, recruited from the community based mental health teams in Nottinghamshire and Leicestershire, UK, matched

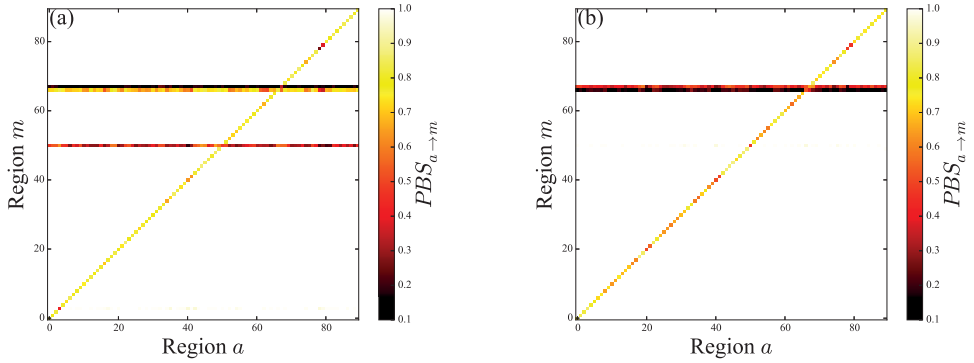

Figure 6.3: Regional pair-wise $\mathcal{PBS}$ in healthy control (a) and schizophrenia (b) with $M_a = 100$. $\mathcal{PBS}_{a\to m}$ is projected on the space of regions a and m and indicate how likely m returns to the synchronous states after m being subjected after any perturbation.

with a number of healthy controls, also recruited from the local community via advertisements. We average structural matrices from both groups respectively, which are shown in Figure 6.2. The self-coupling is set as $\lambda^{a,a} = 1$. This way, we obtain global brain structural networks, corresponding both groups of subjects (healthy control and schizophrenia) respectively. Each network contains 90 regions/subnetworks. Thus, we name $\Lambda = [\lambda_{a,m}]$ *structural connectivity matrix* for the schizophrenia and healthy control respectively. As shown in Fig. 6.2, the two structural connectivity matrices look very similar.

The inter-regional connections $\lambda^{a,m}$ are defined by the mean linking density of fibers between region m and region a, measured from the magnetic resonance imaging. Here, we focus on the group of schizophrenia patients in comparison with healthy controls. we model neural networks such that each contains 90 regions and each region comprises of nodes of the first-order Kuramoto model with synaptic plasticity.

Thus, we simulate the Kuramoto oscillators (6.5) with the STDP rule (6.6) and the two structural connectivity matrices respectively. The parameters are set as $\omega_i^a = 2 - i/(5N_a - 1)$, $N_a = 1$, $M = 90$, $\alpha = 10.0$, $\epsilon = 0.5$, $\tau_p = 0.15$ and $\tau_d = 0.3$. Ordinary differential equations are solved by a 4-th order Runge-Kutta method. Synchronous behaviors are measured by the oscillating dynamics of excitatory nodes: If $\dot{\theta}_i^a$ of the excitatory oscillators within the same region a are synchronized, we say that a is at a synchronous state. That is, $\dot{\theta}_i^a = \dot{\theta}_j^a$, $\forall i, j$ in the region a with $\Delta(i) = \Delta(j) = 1$.

To measure the stability influence in terms of partial basin stability from region a to region m, we perturb oscillators in the region a and check whether the oscillators in the region m return back the synchronous state or not after a long time. In detail, the oscillators in each region initially take values at the synchronous state. We perturb the states at region a randomly in $[-\alpha, \alpha]$ following the uniform distribution for independent M_a times and count the number by which the oscillators in region m converge back to the synchronous states for each group, denoted by $s^g_{a\to m}$, where

$g = HC,\ SZD$ stand for the healthy control and schizophrenia groups, respectively. Thus, to evaluate the influence between different groups, partial basin stability from a to m in the group g is calculated by

$$\mathcal{PBS}^{g}_{a\to m} = \frac{S^{g}_{a\to m}}{M_a}.$$

In particular, the self-loop stability is defined by $\mathcal{PBS}_{a\to a}$.

To understand these features of $\mathcal{PBS}$ with brain regions of schizophrenia in comparison to the healthy control, we define the following quantities to depict the difference of partial basin stability between the schizophrenia and healthy control as follows:

$$St_m = \sum_a 1 - H(\mathcal{PBS}^{HC}_{a\to m} - \mathcal{PBS}^{SZD}_{a\to m}),$$
$$InSt_m = \sum_a 1 - H(\mathcal{PBS}^{SZD}_{a\to m} - \mathcal{PBS}^{HC}_{a\to m}),$$

where $H(\cdot)$ is the Heaviside step function, $St_m \in [0, 90]$ ($InSt_m \in [0, 90]$) for all $m = 1, \cdots, 90$ quantifies the capability of partial stability (instability) of the region m by counting the number of regions in the schizophrenia group with larger (smaller) values of $\mathcal{PBS}$ than that in the healthy control.

As shown in Fig. 6.3, for both schizophrenia and healthy control groups, most regions have available stability influence on themselves with $\mathcal{PBS}_{a\to a} < 1$ but seldom affect the synchronous states of other regions with $\mathcal{PBS}_{a\to m} \approx 1$. Some regions show crucial difference between these two groups. To quantitatively demonstrate the stability influence of the schizophrenia compared to the healthy control, we define stability St and instability $InSt$ as shown in Fig. 6.4.

To simplify notation, given the threshold values of stability and instability, denoted by St_c and $InSt_c$ respectively, all regions with $St_m > St_c$ are collected as *schizophrenia-stable regions* and all regions with $InSt_m > InSt_c$ are defined as *schizophrenia-unstable regions*. We find that the the right precuneus (PCUN.R) and the left middle occipital gyrus (MOG.L) are schizophrenia-stable and the left precuneus (PCUN.L) is the schizophrenia-unstable region. The locations of these schizophrenia-stable (in blue) and schizo-unstable (in red) regions are plotted in Fig. 6.5 by the BrainNet software (Xia et al., 2013).

PCUN.R and PCUN.L show receiving significant influence from many other regions. The precuneus is a key component in the brain default mode network. As a "rich club" member, it has many long distance connections, is able to exert widespread influence on both cortical and limbic functions (Fransson and Marrelec, 2008), and it is involved in many different behavioral functions including reflective and self-related processing (Kjaer et al., 2002), awareness and conscious information processing (Cavanna, 2007), empathy (Harvey et al., 2013), episodic memory (Dörfel et al., 2009) and visuospatial processing (Wenderoth et al., 2005). Many of these functions are impaired in schizophrenia, and most notably studies have reported altered precuneus function associated with impaired self-processing (Zhao et al., 2013), insight (Faget-Agius et al., 2012), and empathy (Harvey et al., 2013) in schizophrenia patients.

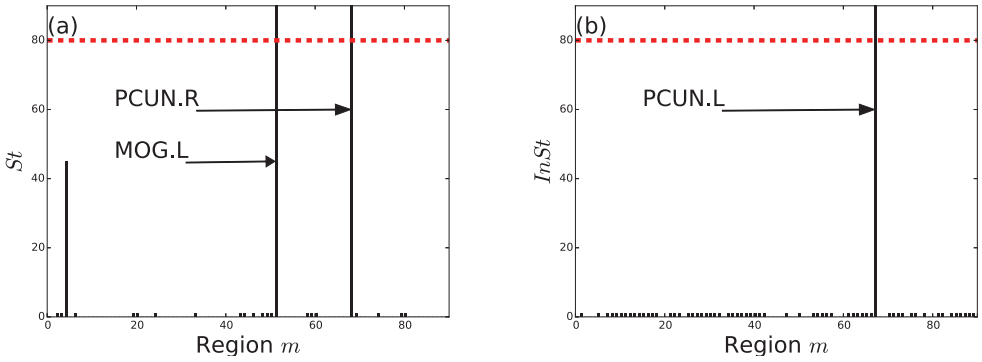

Figure 6.4: Bar-plots of partial stability, St_m, and partial instability, $InSt_m$, with respect to regions with the thresholds $St_c = 80$ and $InSt_c = 80$. The schizophrenia-stable regions: right precuneus (PCUN.R) and left middle occipital gyrus (MOG.L), and the schizophrenia-unstable region: left precuneus (PCUN.L) are outlined.

MOG.L are schizophrenia-stable. The middle occipital gyrus is considered as a part of the visual dorsal stream in sighted subjects (Dumoulin et al., 2000) and identifies a functional preference for processing spatial properties of both auditory and tactile stimuli (Renier et al., 2010). This functioning was observed impaired in schizophrenia patients and so the middle occipital gyrus has been reported abnormal in the schizophrenia. For instance, additional activation during visual hallucinations was found in the middle occipital gyrus (Oertel et al., 2007). In this region, the group differences were attributable to patients having a significantly reduced number of voxels with preferential responses to low spatial frequencies in the visual stimulus compared with controls (Martinez et al., 2008). An elevation of cerebral blood flow (rCBF) of this region occurred during nonverbal theory of mind task in schizophrenia patients (Brunet et al., 2003).

Via evaluating the stability of regions of a schizophrenia group compared to a group of healthy control, we find that right precuneus and left middle occipital gyrus are schizophrenia-stable and the left precuneus is schizophrenia-unstable. Our results are in agreement with these findings achieved via brain functional imaging, however, from the respective of dynamical system theory. The results would vary with increasing values of a coupling term, but our main findings are retained as shown in Fig. 6.6 and 6.7. The stability influence could be due to an impact of global topology (e.g. in neural networks) or local connection schemes. Partial basin stability quantifies the stability influence between different clusters and enhances the understanding of how perturbations spread, and it is a crucial point and is of highest actual importance from various aspects (economy, future society, sustainability etc).

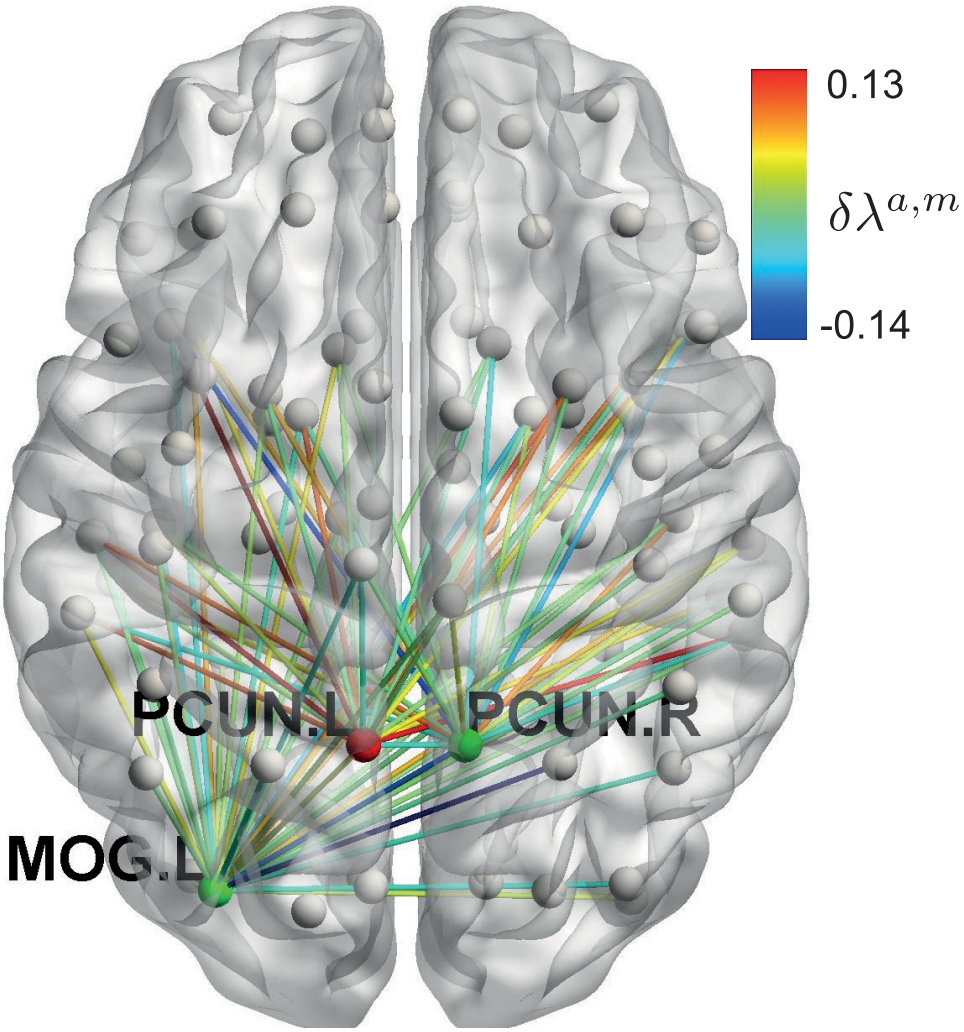

Figure 6.5: The locations of schizophrenia-stable (blue) and schizophrenia-unstable regions (red) on the brain cortex surface and all. We put one node on each region with equal size but different color to denote its stability. Nodes are in gray if its stability $St_m < St_c$ or instability $InSt_m < InSt_c$. The colormap indicates the fibers' number difference $\delta\lambda^{a,m}$ between the group of schizophrenia and healthy control. Here, we only show the links from/to the schizophrenia-stable (PCUN.R, MOG.L) and schizophrenia-unstable (PCUN.L) regions.

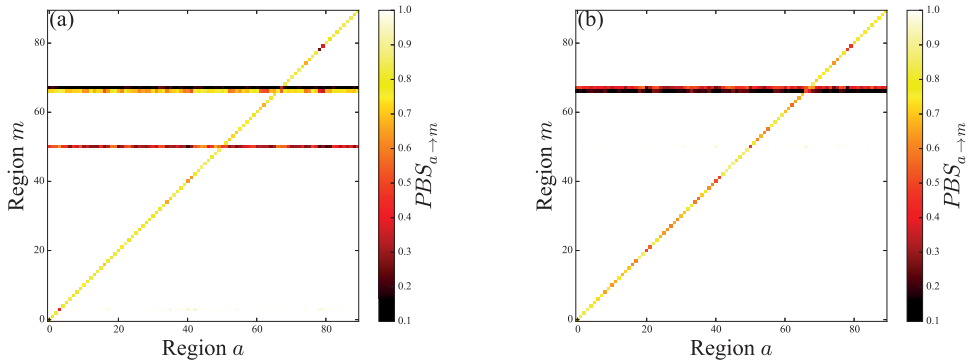

Figure 6.6: Partial basin stability $\mathcal{PBS}_{a\to m}$ from regions a to m in groups of healthy control (a) and schizophrenia (b). In simulations, $M_a^p = 100$. Here, we used different parameters with $\omega_i^a = 2 - i/(5N_a - 1)$, $N_a = 1$, $M = 90$, $\alpha = 10.0$, $\varepsilon = 0.6$ (increased), $\tau_p = 0.15$ and $\tau_d = 0.3$.

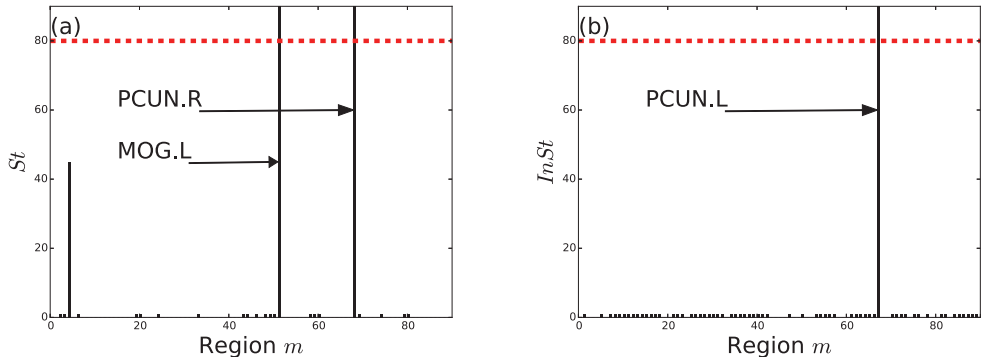

Figure 6.7: Compared to health normal group, the schizophrenia-stable regions of right precuneus (PCUN.R) and left middle occipital gyrus (MOG.L) and the schizophrenia-unstable region of left precuneus (PCUN.L) in the group of schizophrenia with $St_c = 80$ and $InSt_c = 80$. Here, we used different parameters with $\omega_i^a = 2 - i/(5N_a - 1)$, $N_a = 1$, $M = 90$, $\alpha = 10.0$, $\varepsilon = 0.6$ (increased), $\tau_p = 0.15$ and $\tau_d = 0.3$.

6.3.2 Materials

28 patients satisfying DSM-IV criteria for schizophrenia (32.6 ± 8.9 years, 23 males/5 females) and 32 patients parental socio-economic status (Rose and Pevalin, 2003) matched healthy controls (33.4 ± 9.1 years, 22 males/10 females) were included. Patients were recruited from the community-based mental health teams (including Early Intervention in Psychosis teams) in Nottinghamshire and Leicestershire, UK. The diagnosis was made in a clinical consensus meeting in accordance with the procedure of Leckman et al. (Leckman JF et al., 1982), using all available information including a review of case files and a standardized clinical interview (SSPI) (Liddle et al., 2002). All patients were in a stable phase of illness (defined as a change of no more than ten points in their Global Assessment of Function [GAF] score, assessed 6 weeks prior and immediately prior to study participation). The study was given ethical approval by the National Research Ethics Committee, Derbyshire, UK. All volunteers gave written informed consent.

Diffusion-weighted images were acquired using a single-shot, spin-echo, echo planar imaging (EPI) sequence in alignment with the anterior commissure-posterior commissure (AC-PC) plane. The acquisition parameters were as follows: Repetition Time (TR) = 8.63 s, Echo Time (TE) = 56.9 ms, voxel size = 2 mm isotropic, 112 × 112 matrix, Field of View (FoV) = 224 × 224 × 104, flip angle = 90^o, 52 slices, 32 directions with a b-factor of 1000 s/mm^2, EPI Factor = 59, total scan time = 6.29 min.

For DTI images, we first used FMRIB Software Library v5.0 (Jenkinson et al., 2012) to remove the eddy-current and extract the brain mask from the B0 image. Then, we used TrackVis (Wang et al., 2007) to obtain the fiber images by the deterministic tracking method, with anatomical regions defined using the AAL convention on the basis of co-registered T1 image from each subject. This enabled us to determine the presence of streamlines connecting every pair of brain regions. All the processes were performed using the PANDA suite (Cui et al., 2013).

6.4 Power grids

Decarbonizing the energy system requires a strongly increasing usage of low-carbon energy sources (Pachauri and Blair, 2006). The cheapest and widespread way is to link new renewable sources to the nearest neighbor in a power grid, which finally formulates a tree-like connection scheme (Menck et al., 2014). Such tree-like connections, so-called dead ends and dead trees, strongly diminish stability (Menck et al., 2014), i.e. given even a small perturbation, some nodes have a rather small probability to return to the synchronous state where all frequencies equal the reference frequency (50 or 60 Hz).

One of the fundamental problems is that perturbations on one node could cause the whole network failure (Cornelius et al., 2013). Tree-like connection schemes, so-called dead ends and dead trees, could strongly diminish the network stability and cause cascading failure.

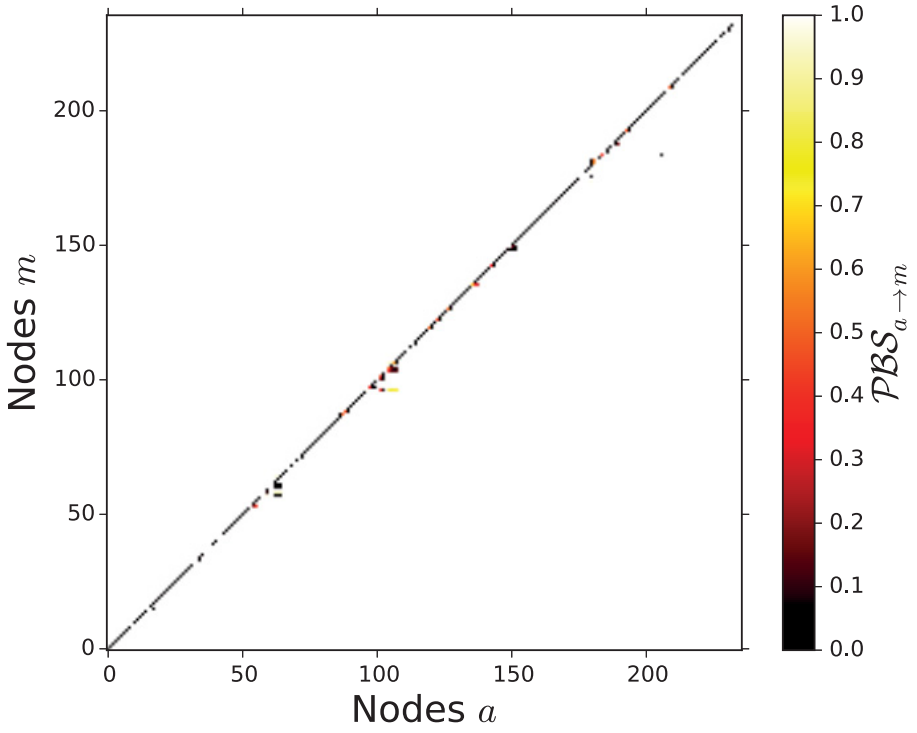

Figure 6.8: Contour plot of $\mathcal{PBS}_{a\to m}$, where, $a, m = 1, 2, \ldots, N$.

We use the classical power grid model based on the swing equation as follows

$$\begin{cases} \dot{\theta}_i = \omega_i \\ \dot{\omega}_i = -\alpha\omega_i + \Omega_i + \lambda \sum_{j=1}^{N} A_{ij} \sin(\theta_j - \theta_i), \end{cases} \tag{6.7}$$

where θ_i, ω_i, and Ω_i are, respectively, the phase, the frequency, and the net power input at generator $i = 1, \cdots, N$, α is the dissipation constant, and the coupling constant λ is the same for all different transmission lines. A_{ij} accounts for the underlying topology with $A_{ij} = 1$ if nodes i and j are connected and $A_{ij} = 0$, otherwise. $A_{ij} \sin(\theta_j - \theta_i)$ describes the power flows along transmission lines. In order to reach an equilibrium, the total energy generation and consumption should be balanced, i.e., $\sum \Omega_i = 0$, and we say that i is a net generator if $\Omega_i > 0$, or a net consumer if $\Omega_i < 0$. $\omega_i = 0, \forall i = 1, \cdots, N$ describe complete synchronization.

Towards partial basin stability, we define the partial attracting set as the frequencies of most nodes m close to 0, which is named *dominant frequency*. That is: $\mathscr{A}_m^\epsilon =$

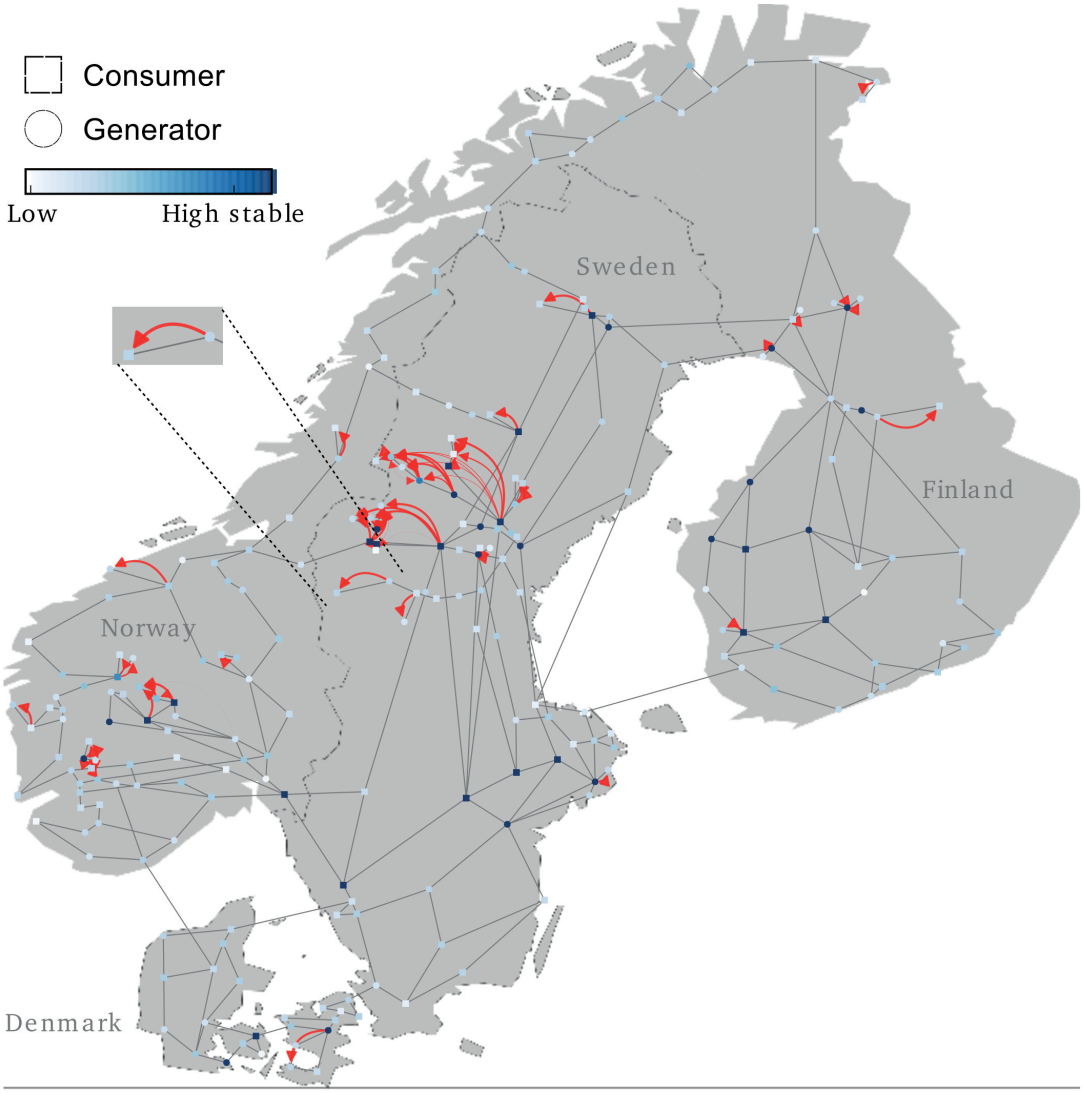

Figure 6.9: The load scenario of the northern European power grid was chosen randomly with half net generators (circles) and half net consumers (squares). The colors of nodes scale the values of self-loop stability, i.e., $\mathcal{PBS}_{a\to a}$, for all nodes. The weighted arrows unveil the existence of non-local influences by the way that the widths of arrows are proportional to the values of $1 - \mathcal{PBS}_{a\to m}$ with $a \neq m$. The subplot specifies a two-nodes motif where a net consumer connects a net generator in the grid.

$\{(\theta_m, \omega_m) : |\omega_m| \leq \epsilon\}$ for some small $0 < \epsilon \ll 1$. We write $\mathscr{A}_m^\epsilon$ by $\mathscr{A}_m$ for simplicity. Then, partial basin stability from nodes a to m can be used to discover local mechanisms and its calculation follows

$$\begin{aligned}&\mathcal{PBS}_{a\to m}(\mathscr{A}_m|(\theta_0^{\mathscr{I}}, \omega_0^{\mathscr{I}})) = \\ &\int\int 1_{\mathscr{A}_m}(\theta(0), \omega(0))\rho(\theta_a(0), \omega_a(0))\delta_{(\theta_a(0),\omega_a(0))}(\theta_0^{\mathscr{I}}, \omega_0^{\mathscr{I}})d\theta_a(0)d\omega_a(0),\end{aligned} \tag{6.8}$$

where $\omega_0^{\mathscr{I}} = 0$. We write $\mathcal{PBS}_{a\to m}(\mathscr{A}_m|(\theta_0^{\mathscr{I}}, \omega_0^{\mathscr{I}}))$ by $\mathcal{PBS}_{a\to m}$ for simplicity in this section.

Numerically, we calculate $\mathcal{PBS}_{a\to m}$ in the following way. Given the initial values of θ_a and ω_a of node a, we integrate system (6.7) for a sufficiently long period of length $t_1 + t_2$ and disregard the first t_1 time period. In order to quantify the stationary state, we average the frequencies in the duration $[t_1, t_1 + t_2]$ as follows

$$\tilde{\omega}_m = \frac{1}{t_2}\int_{t=t_1}^{t_1+t_2} \omega_m dt. \tag{6.9}$$

If $\tilde{\omega}_m$ is within the dominant frequency, i.e. $|\tilde{\omega}_m| \leq \epsilon$, we say that the node m is synchronized.

We integrate this system (6.7) for M_a times with independent different initial values of $(\theta_a(0), \omega_a(0))$ following the density $\rho(\theta_a, \omega_a)$. Then we count the number, for which node m converges to the dominant frequency, namely, $|\tilde{\omega}_m| \leq \epsilon$, and we denote it as $S_{a\to m}$. Then, partial basin stability is calculated by $\mathcal{PBS}_{a\to m} = S_{a\to m}/M_a$. $\mathcal{PBS}_{a\to m} = 1$ means that the synchronization of node m is independent of any perturbation on node a but $\mathcal{PBS}_{a\to m} < 1$ implies the existence of a non-local influence from a to m.

6.4.1 Northern European power grid

Here, we implement partial basin stability to investigate the non-local influence on the northern European power grid, which is extracted from the electricity transmission network in the nordic countries published in the svenska kraftnät, 2009 annual report. This grid has $N = 236$ nodes, and $E = 320$ transmission lines (Menck et al., 2014). The load scenario is chosen to be the same as in the reference (Menck et al., 2014) with half generators ($N/2$ with $\Omega_a = +1$) and half consumers ($N/2$ with $\Omega_a = -1$), as illustrated in Fig. 6.9. The simulation parameters are set with $\alpha = 0.1$ and $\lambda = 8$. Ordinary differential equations are solved by a 4-th order Runge-Kutta method with time step 0.01. In power grids, the dominant frequency is defined by setting $\epsilon = 10^{-4}$.

We have investigated the stability influence from nodes a to m in terms of $\mathcal{PBS}_{a\to m}$ on the northern European power grid. All situations are shown in the contour plot 6.8. The visualization on the grid is shown in Fig. 6.9. A power grid operates in the coexistence regime of stable fixed points and stable limit cycles (Rohden et al., 2012). In most cases, a perturbation on node a has a high probability to trigger itself away from a synchronous state, namely, $\mathcal{PBS}_{a\to a} < 1$. Most importantly, local stability

influences from the perturbation of node a towards the synchronization of another node m, namely, $\mathcal{PBS}_{a\to m} < 1$, although rare, could also be observed indicated by the red arrows.

It is surprising that some nodes that link to dead ends have a large value of partial basin stability, which contradicts to the fact that nodes adjacent to dead ends are likely to have low basin stability (Menck et al., 2014). This is owing to the difference of how the concepts of basin stability and partial basin stability measure stability: basin stability is counted when the *whole system* reaches synchrony, while, partial basin stability is counted when the single node a goes into the dominant frequency. It is valuable to concentrate on the very few transmission lines that have indeed influences between nodes, i.e., $\mathcal{PBS}_{a\to m} < 1$ for some $a \neq m$.

Dead ends are easily perturbed by its neighbors or nodes on the same dead trees. Hence, the dead ends can both undermine the network stability and enhance the local stability. The influence is determined by local connection schemes. Therefore, to discover the underlying mechanism, we have investigated a two-node motif especially, as shown by the subplot of Fig. 6.9, and observe a non-local influence to a dead end. studied a two-node motif separating from a large system.

6.4.2 Two-nodes motif

Dead end separating from a large system has been fully investigated in previous studies (Strogatz, 2014; Menck et al., 2013; Menck et al., 2014; Ji et al., 2013). Depending on the pair of parameters projected on the stability diagram, the system either converges to a synchronous state (in the region of a fixed point), attracts to a limit cycle (in the region of a limit cycle), or has two stationary states in terms of initial values (in the region of bistability).

It is still unclear how dead ends undermine the global stability of its neighbor in the dead trees but enhance the local stability. Therefore, we investigate a simple two-nodes motif: node 1 links to a dead end 2 and a large system. Accordingly, the dynamics of these two nodes follows

$$\ddot{\theta}_1 = -\alpha\dot{\theta}_1 + \Omega_1 + \lambda \sin(\theta_2 - \theta_1) + \lambda \sin(\theta_l - \theta_1), \tag{6.10}$$

$$\ddot{\theta}_2 = -\alpha\dot{\theta}_2 + \Omega_2 + \lambda \sin(\theta_1 - \theta_2), \tag{6.11}$$

where θ_l indicates the phase of the large system and could be taken as a constant. Without loss of generality, we set $\theta_l = 0$. In the region of bistability, when $\Omega_1 = -\Omega_2$, the system could converge to synchrony with $\theta_1^s = 0$, $\theta_2^s = \arcsin(\Omega_2/\lambda)$ and $\omega_1^s = \omega_2^s = 0$. When $\Omega_1 = \Omega_2$, the synchronous solution is indicated by $\theta_1^s = \arcsin(\frac{2\Omega_2}{\lambda})$, $\theta_2^s = \arcsin(\frac{\Omega_2}{\lambda}) + \arcsin(\frac{2\Omega_2}{\lambda})$ and $\omega_1^s = \omega_2^s = 0$.

Initially, the two nodes are at synchronous states. The node 1 is subjected to a random perturbation with $(\theta_1 - \theta_1^s, \omega_1 - \omega_1^s)$. Will the node 1 and/or node 2 return back to the synchronous state? After a long transition, if node 1 returns to the dominant frequency, then this contributes to the self-loop stability $\mathcal{PBS}_{1\to 1}$; if node 2 will not return back to the dominant frequency, then $\mathcal{PBS}_{1\to 2} < 1$.

Recalling that the stationary solution is quantified by the mean frequency. Therefore, given a perturbation on the node 1, we calculate $\tilde{\omega}_1$ and $\tilde{\omega}_2$, respectively, for nodes 1 and 2. After independently and randomly drawing perturbations $(\theta_1 - \theta_1^s, \omega_1 - \omega_1^s)$ from the state space $[-\pi, \pi] \times [-10, 10]$, we find 4 attractors, and show the projection of different attractions on (θ_1, ω_1) for node 1 in Fig. 6.10(a) and (θ_2, ω_2) for node 2 in Fig. 6.10(b). The basins of the different attractors are shown in Fig. 6.11. In what follows, we explain these 4 attractors in details.

Yellow denotes the fully synchronous state with (θ_1^s, ω_1^s) and (θ_2^s, ω_2^s). Black denotes the partial synchronous state, in particular node 1 oscillates around 0 but node 2 converges to the limit cycle. Red denotes a kind of synchronous states, each node oscillates around zero but with large amplitudes. Orange indicates that both oscillators are attracted to limit cycles. Each node runs around its own natural frequency, i.e. not synchronized. In terms of partial basin stability, $\mathcal{PBS}_{1\to 1,2}$ counts the probability that the node 1 or 2 synchronize to the dominant frequency, $\tilde{\omega}_{1,2} \approx 0$.

In Fig. 6.12 we show $\mathcal{PBS}_{1\to 1,2}$ with respect to the coupling strength λ. As expected, $\mathcal{PBS}$ increases with the increasing of λ. At each coupling strength, color bars show the volume of different attractors. $\mathcal{PBS}_{1\to 1}$ sums the volumes of the bottom three attractors. $\mathcal{PBS}_{1\to 2}$ is proportional to the yellow attractor.

Next, we discuss the limit cycles in black and orange, separately.

Black attractor

In the regime of the black attractor, the node 1 oscillates periodically around 0, the node 2 runs periodically around $\tilde{\omega}_2 = \Omega_2/\alpha$ and $\theta_2 \approx \tilde{\omega}_2 t + \theta_2(0)$. To simplify the situation, we assume that the first node is at the synchronous state with constant phase $\theta_1 = 0$, and $\omega_2 = \tilde{\omega}_2 + f_2$, where f_2 is a residual term to be solved, yielding

$$\dot{f}_2(t) = -\alpha f_2(t) - \lambda \sin\left(\tilde{\omega}_2 t + \theta_2(0)\right). \tag{6.12}$$

The special solution to this equation is

$$f_2(t) = \frac{-\alpha \sin\left(\theta_2(0) + \tilde{\omega}_2 t\right) + \tilde{\omega}_2 \cos\left(\theta_2(0) + \tilde{\omega}_2 t\right)}{\alpha^2 + \tilde{\omega}_2^2}. \tag{6.13}$$

Therefore,

$$\omega_2(t) = \tilde{\omega}_2 + \frac{-\alpha \sin\left(\theta_2(0) + \tilde{\omega}_2 t\right) + \tilde{\omega}_2 \cos\left(\theta_2(0) + \tilde{\omega}_2 t\right)}{\alpha^2 + \tilde{\omega}_2^2}. \tag{6.14}$$

Orange attractor

In the state of the orange attractor, nodes 1 and 2 run around its natural frequency $\tilde{\omega}_1 = \Omega_1/\alpha$ and $\tilde{\omega}_2 = \Omega_2/\alpha$, respectively. Therefore, $\theta_1(t) \approx \tilde{\omega}_1 t + \theta_1(0)$ and

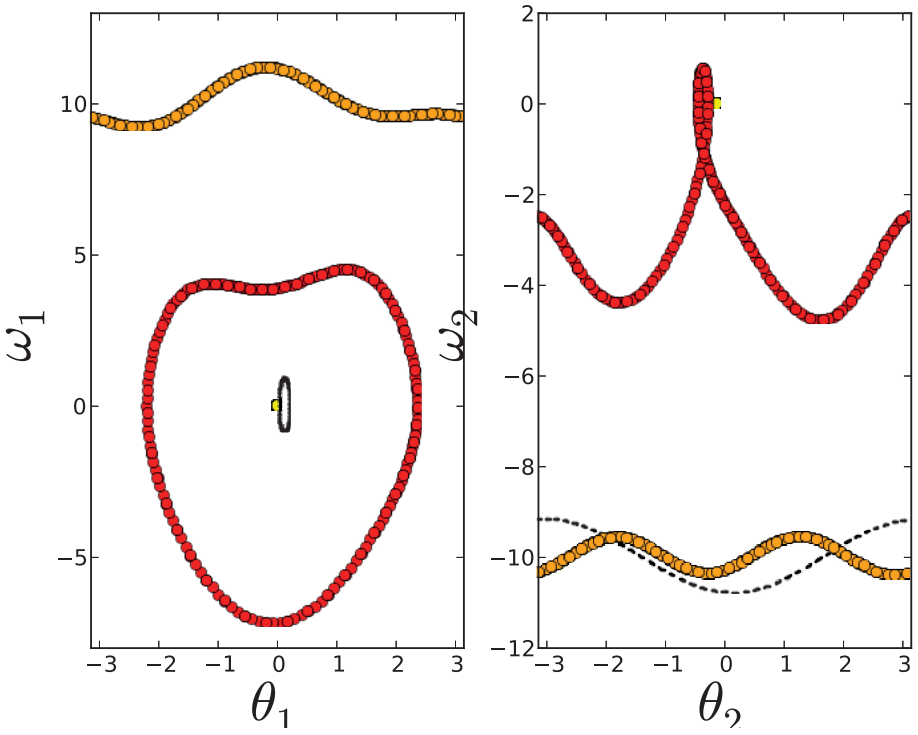

Figure 6.10: Projections of 4 attractors in the phase space (θ_1, ω_1) (a) and (θ_2, ω_2) (b), respectively for nodes 1 and 2. Attractors are in different color.

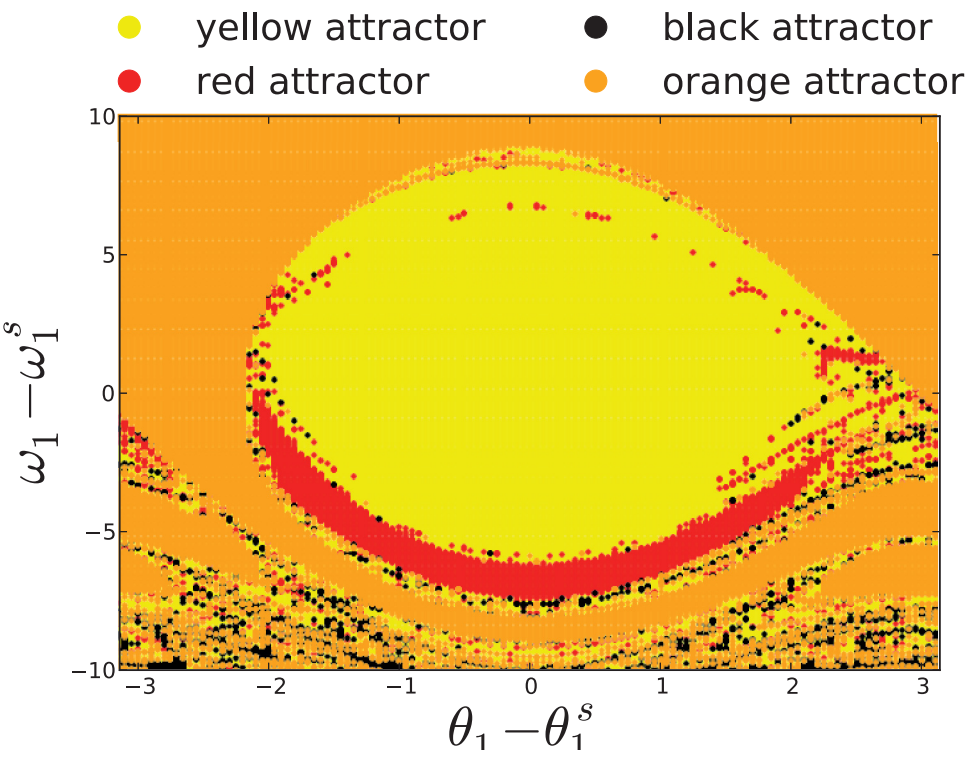

Figure 6.11: Basin of attraction of 4 different attractors in different colors. Here, we set $\Omega_1 = -\Omega_2 = 1$, $\alpha = 0.1$ and $\lambda = 8$.

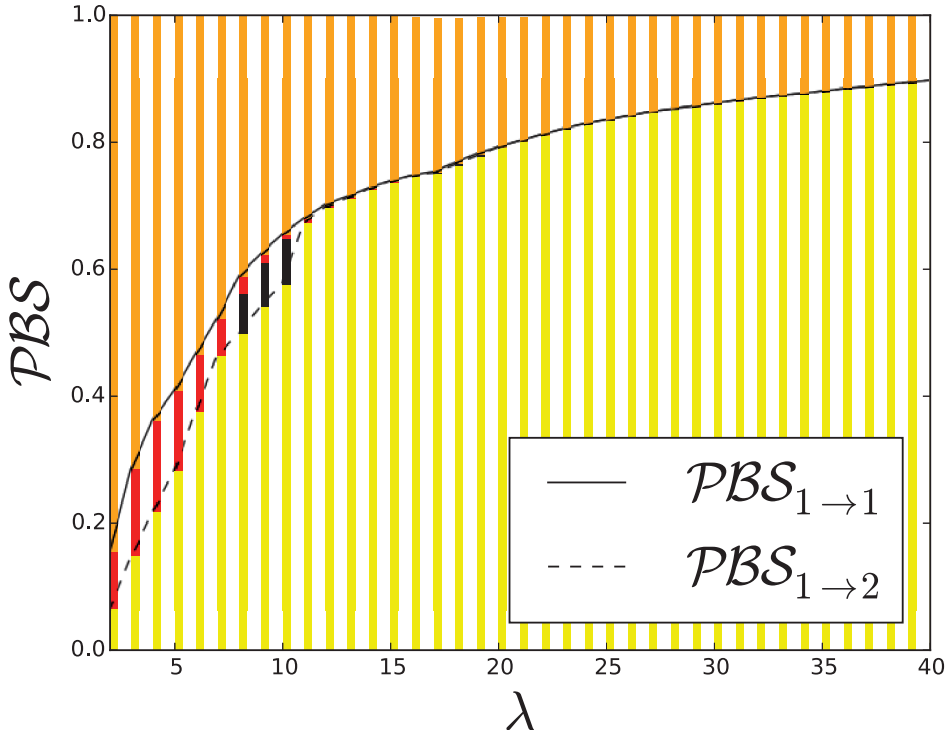

Figure 6.12: Partial basin stability $\mathcal{PBS}$ with respect to the coupling strength λ. In color bars, the volume of different colors is proportional to the percentage of different attractors.

$\theta_2(t) \approx \tilde{\omega}_2 t + \theta_2(0)$. Following the same above process, we assume that $\omega_1 = \tilde{\omega}_1 + f_1(t)$ and $\omega_2 = \tilde{\omega}_2 + f_2(t)$. Substituting the assumption into Eq. (6.11) yields

$$\dot{f}_1(t) = -\alpha f_1(t) + \lambda \sin\left(\tilde{\omega}_2 t + \theta_2(0) - \tilde{\omega}_1 t - \theta_1(0)\right) - \lambda \sin\left(\tilde{\omega}_1 t + \theta_1(0)\right), \tag{6.15}$$

and

$$\dot{f}_2(t) = -\alpha f_2(t) + \lambda \sin\left(\tilde{\omega}_1 t + \theta_1(0) - \tilde{\omega}_2 t - \theta_2(0)\right). \tag{6.16}$$

Due to $\tilde{\omega}_2 = -\tilde{\omega}_1$, for convenience, we set $\delta\theta_{12} \equiv \theta_1(0) + \theta_2(0)$ and rewrite Eq. (6.15) and Eq. (6.16), as follows

$$\dot{f}_1(t) = -\alpha f_1(t) - \lambda \sin\left(2(\tilde{\omega}_1 t + \theta_1(0)) - \delta\theta_{12}\right) - \lambda \sin\left(\tilde{\omega}_1 t + \theta_1(0)\right), \tag{6.17}$$

and

$$\dot{f}_2(t) = -\alpha f_2(t) + \lambda \sin\left(-2\tilde{\omega}_2 t - 2\theta_2(0) + \delta\theta_{12}\right). \tag{6.18}$$

Via discarding higher order terms, we get the approximation of $f_1(t)$ and $f_2(t)$ as

$$f_1(t) \approx \lambda\alpha \frac{\cos\left(\delta\theta_{12} - 2\theta_1(t)\right) + 2\cos\left(\theta_1(t)\right)}{2\tilde{\omega}_1}, \tag{6.19}$$

and

$$f_2(t) \approx \lambda \frac{a \sin\left(\delta\theta_{12} - 2\theta_2(t)\right) + 2\tilde{\omega}_2 \cos\left(\delta\theta_{12} - 2\theta_2(t)\right)}{a^2 + 4{\tilde{\omega}_2}^2}. \tag{6.20}$$

Therefore,

$$\omega_1(t) \approx \tilde{\omega}_1 + \lambda\alpha \frac{\cos\left(\delta\theta_{12} - 2\theta_1(t)\right) + 2\cos\left(\theta_1(t)\right)}{2\tilde{\omega}_1}, \tag{6.21}$$

and

$$\omega_2 \approx \tilde{\omega}_2 + \lambda \frac{a \sin\left(\delta\theta_{12} - 2\theta_2(t)\right) + 2\tilde{\omega}_2 \cos\left(\delta\theta_{12} - 2\theta_2(t)\right)}{a^2 + 4\tilde{\omega}_2^2}. \tag{6.22}$$

In Fig. 6.13, simulations are conducted to validate the analytical solution.

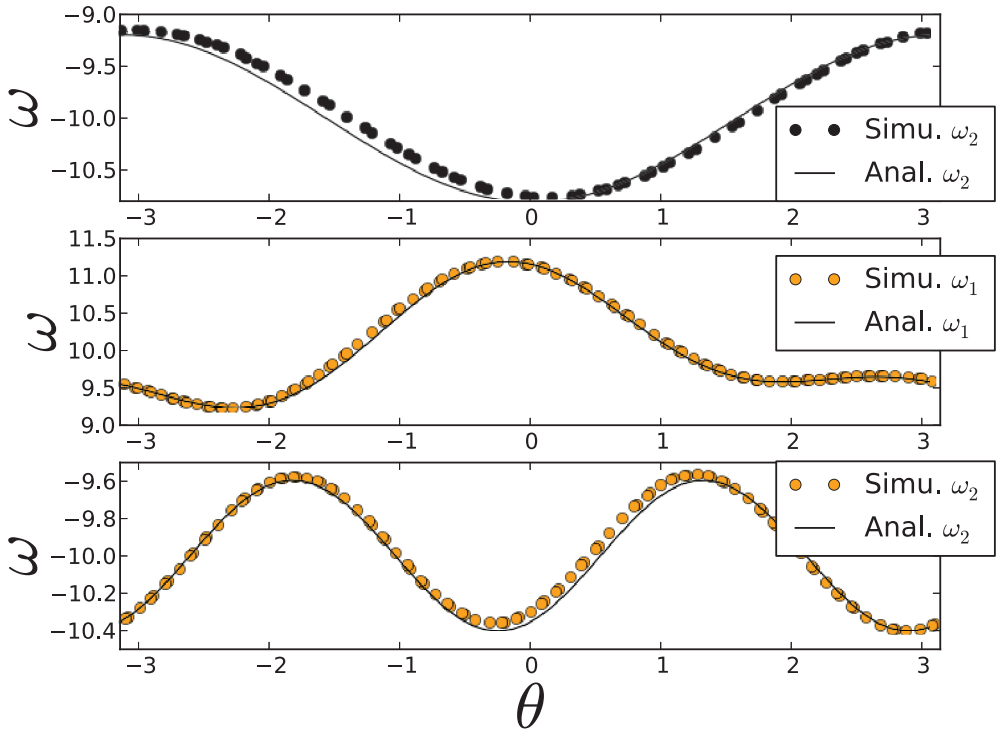

Figure 6.13: Analytical and simulation results of the limit cycle of the node 2 in the state of the black attractor (a). In the state of the orange attractor, the panels (b) and (c) show the limit cycles for the nodes 1 and 2, respectively. The analytical solutions are obtained from Eqs. (6.14) (a), (6.21) (b) and (6.22) (c). The $\delta\theta_{12} = -0.5$ is determined by the initial phase difference.

6.5 Conclusions

In this chapter, we implement the concept of partial basin stability on two examples of networked systems: neural networks and the northern European power grid, both from real data.

The neural network of the brain is well known to be partitioned into different functional sub-networks (clusters/regions) according to its functional and anatomical features. Partial synchronization in each sub-network is essential for specific cognition behavior. Long-distant axonal and synaptic couplings play an important role in the information transmission. Hence, we will measure such interactions by partial synchronization between sub-networks in terms of partial basin stability.

As illustrated in (Menck et al., 2014), tree-like connection schemes (so-called-dead ends and dead trees) are crucial to diminish basin stability of the whole network. To deepen the understanding of the underlying mechanism how dead ends and dead trees undermine the power grid stability, we evaluate the influence of the perturbation of a randomly selected node a on the remote nodes m, in particular dead ends, using partial basin stability.

Chapter 7

Conclusion and outlook

Nonlinear dynamics has been boosted in the past few years thanks to theoretical and methodological developments and the discovery of a plethora of rich phenomena. For instance, the properties of low-dimensional behavior were first characterized by Watanabe-Strogatz theory (Watanabe and Strogatz, 1994) and later further improved by Ott and Antonsen (Ott and Antonsen, 2008). Others include discontinuous phase transitions induced by the correlation between dynamics and topology (Gómez-Gardenes et al., 2011), and basin stability (Menck et al., 2013) in terms of the attracting basin of desirable states. This thesis was motivated by these fascinating phenomena and explored novel extensions for the Kuramoto model with inertia.

I hope that the contributions of this thesis as summarized below not only provide novel theoretical and methodological insights for the Kuramoto model with inertia, but also spark new ideas on inertia effects of related systems.

7.1 Summary

In the following, I summarize the main contributions of this thesis and give an outlook to further avenues for research. The relevant papers are also listed for reference.

As mentioned above, the Ott-Antonsen ansatz triggered many works on the low-dimensional behavior of the first-order Kuramoto model. Regarding the second-order Kuramoto model, we explored its low dimensional behavior in terms of the ansatz considering stationary density functions of phase oscillators following a Poisson kernel, which unfortunately turns out to be an unsuccessful approach due to the problem of the Fourier expansion of the density functions. Alternatively, we have derived self-consistent equations for the order parameter yielding a nonlinear time-dependent function (Sec. 3.3).

Relevant papers: (Ji et al., 2014b).

The first research question of this thesis was devoted to discontinuous phase transitions in the presence of a positive correlation between the dynamics and the network topology (Chapter 4). Subsequently, we focused on basin stability in complex networks (Chapter. 5) and its extension to cluster synchronization (Chapter 6). To achieve these goals, we have employed a mean-field approximation with an asymmetrical natural frequency, simulations in the presence of heterogeneous connections, and other approaches.

As the first main part of this thesis, we substantially extended the first-order Kuramoto model with frequency-degree correlation to the Kuramoto model with inertia to demonstrate phase transitions to synchronization, by considering the natural frequency of each oscillator proportional to its degree (Sec. 4.2). Unlike explosive synchronization (Gómez-Gardenes et al., 2011), where all nodes synchronize at the same time, we have found that nodes of the same degree can form clusters, where low degree nodes join the synchronous component simultaneously and high degree nodes synchronize successively. We called the newly observed phenomenon *cluster explosive synchronization* (Sec. 4.2). However, abrupt phase synchronizations depend not only on the degree-frequency correlation but also on assortative mixing. In particular, we have shown the existence of discontinuous phase transitions in disassortative as well as assortative networks. Furthermore, we have found that the effects of assortative mixing in the connections can be compensated by adjusting the dissipation associated to the oscillators' phases (Sec. 4.3). In other words, similar dynamical states can be obtained by either tuning the network structure or the intrinsic characteristics of its units. This might have important potential applications, e.g., for power grids.

Relevant papers: (Ji et al., 2013; Ji et al., 2014a; Peron et al., 2015).

In the context of abrupt transitions, different initial conditions allow hysteresis. For large perturbations the system could move from desirable states to undesirable states. The corresponding probability of returning to the desirable states is quantified by basin stability (Menck et al., 2013).

As the second main part of this thesis, we firstly investigated the transitions uncovered by basin stability of synchronized states of different oscillators in the continuum limit and have found that two first-order transitions occur successively consisting of *an onset transition* from instability to local stability and *a suffusing transition* from local to global stability (Sec. 5.2).

Relevant papers: (Ji and Kurths, 2014a; Ji and Kurths, 2014b; Ji et al., 2015).

Basin stability indicates how likely *the whole system* returns to a desirable state. For cluster synchronization, we have proposed a new concept of *partial basin stability* to quantify the stability influence between clusters (Sec. 6.2). This concept was applied to two highly relevant examples: neural networks (Sec. 6.3) and the northern European power grid (Sec. 6.4). For the case of neural networks, we have identified abnormal regions (the precuneus and the left middle occipital gyrus) in the human brain in a patient group of schizophrenia from a dynamical point of view, which confirms previous findings based on observations (Sec. 6.3). For power grids, we have explained how dead ends can decrease the network stability (Sec. 6.4).

We believe that partial basin stability will provide a powerful tool to deepen the understanding of the underlying mechanisms of perturbation spreading in research areas such as medicine, systems biology, and earth system analysis.

7.2 Outlook

We have provided a theoretical framework of cluster explosive synchronization for the second-order Kuramoto model with frequency-degree correlations in uncorrelated networks (in the continuum limit). Still, the underlying mechanism for the occurrence of hysteresis in scale-free networks still remains an interesting open question and the effects of, e.g., time delays and noise might give rise to novel phenomena. Further, while we have numerically illustrated the effects of assortative mixing, a mean-field approximation is still missing and also a theoretical framework of the second-order Kuramoto model in assortative networks in the continuum limit is still subject for further research (Restrepo and Ott, 2014). Moreover, as specified by Tanaka et al. (Tanaka et al., 1997a; Tanaka et al., 1997b), while a framework exists for uniform, Lorentzian, and Gaussian intrinsic frequency distributions in the second-order Kuramoto model, the results are still open for asymmetrical natural distributions.

The above results are derived, provided that the stationary solution of the order parameter r is assumed to be constant, especially when the network size approaches infinity or in the continuum limit. But due to the effects of inertia, drifting oscillators as well as locked oscillators contribute to the phase coherence, and a secondary synchronization within the drifting oscillators emerges. Fluctuations of r are, therefore, unavoidable due to the inertia effects, and the underlying mechanisms need to be further investigated.

As illustrated in Ref. (Filatrella et al., 2008), the system is either capable to withstand a perturbation or looses its stability depending on not only the strength of perturbations, but also on the duration, which has not yet been included in the definition of basin stability. It would be interesting to investigate how the duration of perturbations affects, e.g., the stability of dead ends and dead trees (Menck et al., 2014).

Bibliography

Acebrón, J. A. and R. Spigler (Sept. 14, 1998). "Adaptive Frequency Model for Phase-Frequency Synchronization in Large Populations of Globally Coupled Nonlinear Oscillators". In: *Physical Review Letters* 81.11, pp. 2229–2232. DOI: 10.1103/PhysRevLett.81.2229.

Acebrón, J. A., L. L. Bonilla, and R. Spigler (Sept. 1, 2000). "Synchronization in populations of globally coupled oscillators with inertial effects". In: *Physical Review E* 62.3, pp. 3437–3454. DOI: 10.1103/PhysRevE.62.3437.

Acebrón, Juan A., L. L. Bonilla, Conrad J. Pérez Vicente, Félix Ritort, and Renato Spigler (Apr. 7, 2005). "The Kuramoto model: A simple paradigm for synchronization phenomena". In: *Reviews of Modern Physics* 77.1, pp. 137–185. DOI: 10.1103/RevModPhys.77.137.

Achlioptas, Dimitris, Raissa M. D'Souza, and Joel Spencer (Mar. 13, 2009). "Explosive Percolation in Random Networks". In: *Science* 323.5920, pp. 1453–1455. ISSN: 0036-8075, 1095-9203. DOI: 10.1126/science.1167782.

Alexander, J.c., James A. Yorke, Zhiping You, and I. Kan (Dec. 1, 1992). "Riddled basins". In: *International Journal of Bifurcation and Chaos* 02.4, pp. 795–813. ISSN: 0218-1274. DOI: 10.1142/S0218127492000446.

Allefeld, Carsten, Markus Müller, and Jürgen Kurths (Oct. 1, 2007). "Eigenvalue decomposition as a generalized synchronization cluster analysis". In: *International Journal of Bifurcation and Chaos* 17.10, pp. 3493–3497. ISSN: 0218-1274. DOI: 10.1142/S0218127407019251.

Arenas, Alex, Albert Diaz-Guilera, Jurgen Kurths, Yamir Moreno, and Changsong Zhou (Dec. 2008). "Synchronization in complex networks". In: *Physics Reports* 469.3, pp. 93–153. ISSN: 0370-1573. DOI: 10.1016/j.physrep.2008.09.002.

Barlev, Gilad, Thomas M. Antonsen, and Edward Ott (June 1, 2011). "The dynamics of network coupled phase oscillators: An ensemble approach". In: *Chaos: An Interdisciplinary Journal of Nonlinear Science* 21.2, p. 025103. ISSN: 1054-1500, 1089-7682. DOI: 10.1063/1.3596711.

Barrat, Alain, Marc Barthélemy, and Alessandro Vespignani (Oct. 23, 2008). *Dynamical Processes on Complex Networks*. Cambridge University Press. 586 pp. ISBN: 9781107377424.

Basnarkov, Lasko and Viktor Urumov (Nov. 5, 2007). "Phase transitions in the Kuramoto model". In: *Physical Review E* 76.5, p. 057201. DOI: 10.1103/PhysRevE.76.057201.

– (July 18, 2008). "Kuramoto model with asymmetric distribution of natural frequencies". In: *Physical Review E* 78.1, p. 011113. DOI: 10.1103/PhysRevE.78.011113.

Boccaletti, S., V. Latora, Y. Moreno, M. Chavez, and D. U. Hwang (Feb. 2006). "Complex networks: Structure and dynamics". In: *Physics Reports* 424.4, pp. 175–308. ISSN: 0370-1573. DOI: 10.1016/j.physrep.2005.10.009.

Brede, Markus (Apr. 7, 2008). "Synchrony-optimized networks of non-identical Kuramoto oscillators". In: *Physics Letters A* 372.15, pp. 2618–2622. ISSN: 0375-9601. DOI: 10.1016/j.physleta.2007.11.069.

Brunet, Eric, Yves Sarfati, Marie-Christine Hardy-Baylé, and Jean Decety (2003). "Abnormalities of brain function during a nonverbal theory of mind task in schizophrenia". In: *Neuropsychologia* 41.12, pp. 1574–1582. ISSN: 0028-3932. DOI: 10.1016/S0028-3932(03)00119-2.

Buldyrev, Sergey V., Roni Parshani, Gerald Paul, H. Eugene Stanley, and Shlomo Havlin (Apr. 15, 2010). "Catastrophic cascade of failures in interdependent networks". In: *Nature* 464.7291, pp. 1025–1028. ISSN: 0028-0836. DOI: 10.1038/nature08932.

Buzna, Lubos, Sergi Lozano, and Albert Diaz-Guilera (Dec. 23, 2009). "Synchronization in symmetric bipolar population networks". In: *Physical Review E* 80.6, p. 066120. DOI: 10.1103/PhysRevE.80.066120.

Cavanna, Andrea E. (July 2007). "The Precuneus and Consciousness". In: *CNS Spectrums* 12.7, pp. 545–552. ISSN: 2165-6509. DOI: 10.1017/S1092852900021295.

Chavez, M., D.-U. Hwang, J. Martinerie, and S. Boccaletti (Dec. 14, 2006). "Degree mixing and the enhancement of synchronization in complex weighted networks". In: *Physical Review E* 74.6, p. 066107. DOI: 10.1103/PhysRevE.74.066107.

Chen, Hanshuang, Gang He, Feng Huang, Chuansheng Shen, and Zhonghuai Hou (Sept. 1, 2013). "Explosive synchronization transitions in complex neural networks". In: *Chaos: An Interdisciplinary Journal of Nonlinear Science* 23.3, p. 033124. ISSN: 1054-1500, 1089-7682. DOI: 10.1063/1.4818543.

Chiang, Hsiao-Dong (Mar. 16, 2011). *Direct Methods for Stability Analysis of Electric Power Systems: Theoretical Foundation, BCU Methodologies, and Applications*. John Wiley & Sons. 510 pp. ISBN: 9781118088128.

Cho, Y. S., J. S. Kim, J. Park, B. Kahng, and D. Kim (Sept. 23, 2009). "Percolation Transitions in Scale-Free Networks under the Achlioptas Process". In: *Physical Review Letters* 103.13, p. 135702. DOI: 10.1103/PhysRevLett.103.135702.

Chung, Fan and Linyuan Lu (Dec. 10, 2002). "The average distances in random graphs with given expected degrees". In: *Proceedings of the National Academy of Sciences* 99.25, pp. 15879–15882. ISSN: 0027-8424, 1091-6490. DOI: 10.1073/pnas.252631999.

Cornelius, Sean P., William L. Kath, and Adilson E. Motter (June 27, 2013). "Realistic control of network dynamics". In: *Nature Communications* 4. DOI: 10.1038/ncomms2939.

Costa, R. A. da, S. N. Dorogovtsev, A. V. Goltsev, and J. F. F. Mendes (Dec. 14, 2010). "Explosive Percolation Transition is Actually Continuous". In: *Physical Review Letters* 105.25, p. 255701. DOI: 10.1103/PhysRevLett.105.255701.

Coutinho, B. C., A. V. Goltsev, S. N. Dorogovtsev, and J. F. F. Mendes (Mar. 4, 2013). "Kuramoto model with frequency-degree correlations on complex networks". In: *Physical Review E* 87.3, p. 032106. DOI: 10.1103/PhysRevE.87.032106.

Cui, Zaixu, Suyu Zhong, Pengfei Xu, Yong He, and Gaolang Gong (Feb. 21, 2013). "PANDA: a pipeline toolbox for analyzing brain diffusion images". In: *Frontiers in Human Neuroscience* 7. ISSN: 1662-5161. DOI: 10.3389/fnhum.2013.00042.

Del Genio, Charo I., Thilo Gross, and Kevin E. Bassler (Oct. 17, 2011). "All Scale-Free Networks Are Sparse". In: *Physical Review Letters* 107.17, p. 178701. DOI: 10.1103/PhysRevLett.107.178701.

DHuys, O., R. Vicente, T. Erneux, J. Danckaert, and I. Fischer (Sept. 1, 2008). "Synchronization properties of network motifs: Influence of coupling delay and symmetry". In: *Chaos: An Interdisciplinary Journal of Nonlinear Science* 18.3, p. 037116. ISSN: 1054-1500, 1089-7682. DOI: 10.1063/1.2953582.

Di Bernardo, M., F. Garofalo, and F. Sorrentino (Oct. 1, 2007). "Effects of degree correlation on the synchronization of networks of oscillators". In: *International Journal of Bifurcation and Chaos* 17.10, pp. 3499–3506. ISSN: 0218-1274. DOI: 10.1142/S0218127407019263.

Dörfel, Denise, Annett Werner, Michael Schaefer, Rüdiger Von Kummer, and Anke Karl (Nov. 1, 2009). "Distinct brain networks in recognition memory share a defined region in the precuneus". In: *European Journal of Neuroscience* 30.10, pp. 1947–1959. ISSN: 1460-9568. DOI: 10.1111/j.1460-9568.2009.06973.x.

Dörfler, F. and F. Bullo (Jan. 1, 2012). "Synchronization and Transient Stability in Power Networks and Nonuniform Kuramoto Oscillators". In: *SIAM Journal on Control and Optimization* 50.3, pp. 1616–1642. ISSN: 0363-0129. DOI: 10.1137/110851584.

Dörfler, Florian, Michael Chertkov, and Francesco Bullo (Feb. 5, 2013). "Synchronization in complex oscillator networks and smart grids". In: *Proceedings of the National Academy of Sciences* 110.6, pp. 2005–2010. ISSN: 0027-8424, 1091-6490. DOI: 10.1073/pnas.1212134110.

Dumoulin, Serge O., Richard G. Bittar, Noor J. Kabani, Curtis L. Baker, Georges Le Goualher, G. Bruce Pike, and Alan C. Evans (May 1, 2000). "A New Anatomical Landmark for Reliable Identification of Human Area V5/MT: a Quantitative Analysis of Sulcal Patterning". In: *Cerebral Cortex* 10.5, pp. 454–463. ISSN: 1047-3211, 1460-2199. DOI: 10.1093/cercor/10.5.454.

Ermentrout, B. (June 1, 1991). "An adaptive model for synchrony in the firefly Pteroptyx malaccae". In: *Journal of Mathematical Biology* 29.6, pp. 571–585. ISSN: 0303-6812, 1432-1416. DOI: 10.1007/BF00164052.

Faget-Agius, Catherine, Laurent Boyer, Romain Padovani, RaphaÃ«lle Richieri, Olivier Mundler, Christophe LanÃ§on, and Eric Guedj (Sept. 2012). "Schizophrenia with preserved insight is associated with increased perfusion of the precuneus". In: *Journal of psychiatry & neuroscience: JPN* 37.5, pp. 297–304. ISSN: 1488-2434. DOI: 10.1503/jpn.110125.

Filatrella, G., A. H. Nielsen, and N. F. Pedersen (Mar. 7, 2008). "Analysis of a power grid using a Kuramoto-like model". In: *The European Physical Journal B* 61.4, pp. 485–491. ISSN: 1434-6028, 1434-6036. DOI: 10.1140/epjb/e2008-00098-8.

Fransson, Peter and Guillaume Marrelec (Sept. 2008). "The precuneus/posterior cingulate cortex plays a pivotal role in the default mode network: Evidence from a

partial correlation network analysis". In: *NeuroImage* 42.3, pp. 1178–1184. ISSN: 1053-8119. DOI: 10.1016/j.neuroimage.2008.05.059.

Gómez-Gardenes, Jesús, Sergio Gómez, Alex Arenas, and Yamir Moreno (Mar. 23, 2011). "Explosive Synchronization Transitions in Scale-Free Networks". In: *Physical Review Letters* 106.12, p. 128701. DOI: 10.1103/PhysRevLett.106.128701.

Guckenheimer, John and Philip Holmes (1983). *Nonlinear Oscillations, Dynamical Systems, and Bifurcations of Vector Fields*. Springer Science & Business Media. 475 pp. ISBN: 9781461211402.

Gupta, Shamik, Alessandro Campa, and Stefano Ruffo (Feb. 2014). "Nonequilibrium first-order phase transition in coupled oscillator systems with inertia and noise". In: *Physical Review E* 89.2. Cited by 0008, p. 022123. DOI: 10.1103/PhysRevE.89.022123.

Harvey, Philippe-Olivier, Jamil Zaki, Junghee Lee, Kevin Ochsner, and Michael F. Green (May 1, 2013). "Neural Substrates of Empathic Accuracy in People With Schizophrenia". In: *Schizophrenia Bulletin* 39.3, pp. 617–628. ISSN: 0586-7614, 1745-1701. DOI: 10.1093/schbul/sbs042.

Hong, H., M. Y. Choi, and Beom Jun Kim (Jan. 2002). "Synchronization on small-world networks". In: *Physical Review E* 65.2, p. 026139. DOI: 10.1103/PhysRevE.65.026139.

Iatsenko, D., S. Petkoski, P. V. E. McClintock, and A. Stefanovska (Feb. 5, 2013). "Stationary and Traveling Wave States of the Kuramoto Model with an Arbitrary Distribution of Frequencies and Coupling Strengths". In: *Physical Review Letters* 110.6, p. 064101. DOI: 10.1103/PhysRevLett.110.064101.

Ichinomiya, Takashi (Aug. 30, 2004). "Frequency synchronization in a random oscillator network". In: *Physical Review E* 70.2, p. 026116. DOI: 10.1103/PhysRevE.70.026116.

Jenkinson, Mark, Christian F. Beckmann, Timothy E. J. Behrens, Mark W. Woolrich, and Stephen M. Smith (Aug. 15, 2012). "FSL". In: *NeuroImage*. 20 YEARS OF fMRI 20 YEARS OF fMRI 62.2, pp. 782–790. ISSN: 1053-8119. DOI: 10.1016/j.neuroimage.2011.09.015.

Ji, Peng and Jürgen Kurths (Jan. 1, 2014a). "Basin Stability in Complex Oscillator Networks". In: *Nonlinear Dynamics of Electronic Systems*. Ed. by Valeri M. Mladenov and Plamen Ch Ivanov. Communications in Computer and Information Science 438. Springer International Publishing, pp. 211–218. ISBN: 978-3-319-08671-2, 978-3-319-08672-9.

– (June 2014b). "Basin stability of the Kuramoto-like model in small networks". en. In: *The European Physical Journal Special Topics* 223.12, pp. 2483–2491. ISSN: 1951-6355, 1951-6401. DOI: 10.1140/epjst/e2014-02213-0.

Ji, Peng, Thomas K. DM. Peron, Peter J. Menck, Francisco A. Rodrigues, and Jürgen Kurths (May 23, 2013). "Cluster Explosive Synchronization in Complex Networks". In: *Physical Review Letters* 110.21, p. 218701. DOI: 10.1103/PhysRevLett.110.218701.

Ji, Peng, Thomas K. DM. Peron, Francisco A. Rodrigues, and Jürgen Kurths (Dec. 18, 2014a). "Analysis of cluster explosive synchronization in complex networks". In: *Physical Review E* 90.6, p. 062810. DOI: 10.1103/PhysRevE.90.062810.

Ji, Peng, Thomas K. D. M. Peron, Francisco A. Rodrigues, and Jürgen Kurths (May 2, 2014b). "Low-dimensional behavior of Kuramoto model with inertia in complex networks". In: *Scientific Reports* 4. DOI: 10.1038/srep04783.

Ji, Peng, Wenlian Lu, and Jürgen Kurths (Mar. 2015). "Onset and suffusing transitions towards synchronization in complex networks". en. In: *EPL (Europhysics Letters)* 109.6, p. 60005. ISSN: 0295-5075. DOI: 10.1209/0295-5075/109/60005.

Kjaer, Troels W., Markus Nowak, and Hans C. Lou (Oct. 2002). "Reflective Self-Awareness and Conscious States: PET Evidence for a Common Midline Parietofrontal Core". In: *NeuroImage* 17.2, pp. 1080–1086. ISSN: 1053-8119. DOI: 10.1006/nimg.2002.1230.

Kuramoto, Yoshiki (1975). "Self-entrainment of a population of coupled non-linear oscillators". In: *International Symposium on Mathematical Problems in Theoretical Physics*. Ed. by Prof Huzihiro Araki. Lecture Notes in Physics 39. Springer Berlin Heidelberg, pp. 420–422. ISBN: 978-3-540-07174-7, 978-3-540-37509-8.

– (2003). *Chemical Oscillations, Waves, and Turbulence*. Courier Corporation. 180 pp. ISBN: 9780486428819.

Lai, Yi Ming and Mason A. Porter (July 9, 2013). "Noise-induced synchronization, desynchronization, and clustering in globally coupled nonidentical oscillators". In: *Physical Review E* 88.1, p. 012905. DOI: 10.1103/PhysRevE.88.012905.

Le Bihan, Denis, Jean-FranÃ§ois Mangin, Cyril Poupon, Chris A. Clark, Sabina Pappata, Nicolas Molko, and Hughes Chabriat (Apr. 1, 2001). "Diffusion tensor imaging: Concepts and applications". In: *Journal of Magnetic Resonance Imaging* 13.4, pp. 534–546. ISSN: 1522-2586. DOI: 10.1002/jmri.1076.

Leckman JF, Sholomskas D, Thompson D, Belanger A, and Weissman MM (Aug. 1, 1982). "Best estimate of lifetime psychiatric diagnosis: A methodological study". In: *Archives of General Psychiatry* 39.8, pp. 879–883. ISSN: 0003-990X. DOI: 10.1001/archpsyc.1982.04290080001001.

Lee, Wai Shing, Edward Ott, and Thomas M. Antonsen (July 22, 2009). "Large Coupled Oscillator Systems with Heterogeneous Interaction Delays". In: *Physical Review Letters* 103.4, p. 044101. DOI: 10.1103/PhysRevLett.103.044101.

Leyva, I., R. Sevilla-Escoboza, J. M. Buldú, I. Sendina-Nadal, J. Gómez-Gardenes, A. Arenas, Y. Moreno, S. Gómez, R. Jaimes-Reátegui, and S. Boccaletti (Apr. 20, 2012). "Explosive First-Order Transition to Synchrony in Networked Chaotic Oscillators". In: *Physical Review Letters* 108.16, p. 168702. DOI: 10.1103/PhysRevLett.108.168702.

Leyva, I., A. Navas, I. Sendina-Nadal, J. A. Almendral, J. M. Buldú, M. Zanin, D. Papo, and S. Boccaletti (Feb. 15, 2013). "Explosive transitions to synchronization in networks of phase oscillators". In: *Scientific Reports* 3. DOI: 10.1038/srep01281.

Li, Ping, Kai Zhang, Xiaoke Xu, Jie Zhang, and Michael Small (Apr. 3, 2013). "Reexamination of explosive synchronization in scale-free networks: The effect of

disassortativity". In: *Physical Review E* 87.4, p. 042803. DOI: 10.1103/PhysRevE.87.042803.

Liddle, Peter F., Elton T. C. Ngan, Gary Duffield, King Kho, and Anthony J. Warren (Jan. 1, 2002). "Signs and Symptoms of Psychotic Illness (SSPI): a rating scale". In: *The British Journal of Psychiatry* 180.1, pp. 45–50. ISSN: 0007-1250, 1472-1465. DOI: 10.1192/bjp.180.1.45.

Liu, Weiqing, Ye Wu, Jinghua Xiao, and Meng Zhan (Feb. 1, 2013). "Effects of frequency-degree correlation on synchronization transition in scale-free networks". In: *EPL (Europhysics Letters)* 101.3, p. 38002. ISSN: 0295-5075. DOI: 10.1209/0295-5075/101/38002.

Machowski, Jan, Janusz Bialek, and Dr Jim Bumby (Aug. 31, 2011). *Power System Dynamics: Stability and Control*. John Wiley & Sons. 780 pp. ISBN: 9781119965053.

Maistrenko, Yuri L., Borys Lysyansky, Christian Hauptmann, Oleksandr Burylko, and Peter A. Tass (June 18, 2007). "Multistability in the Kuramoto model with synaptic plasticity". In: *Physical Review E* 75.6, p. 066207. DOI: 10.1103/PhysRevE.75.066207.

Manik, Debsankha, Dirk Witthaut, Benjamin Schäfer, Moritz Matthiae, Andreas Sorge, Martin Rohden, Eleni Katifori, and Marc Timme (Sept. 26, 2014). "Supply networks: Instabilities without overload". In: *The European Physical Journal Special Topics* 223.12, pp. 2527–2547. ISSN: 1951-6355, 1951-6401. DOI: 10.1140/epjst/e2014-02274-y.

Martinez, Antigona, Steven A. Hillyard, Elisa C. Dias, Donald J. Hagler, Pamela D. Butler, David N. Guilfoyle, Maria Jalbrzikowski, Gail Silipo, and Daniel C. Javitt (July 23, 2008). "Magnocellular Pathway Impairment in Schizophrenia: Evidence from Functional Magnetic Resonance Imaging". In: *The Journal of Neuroscience* 28.30, pp. 7492–7500. ISSN: 0270-6474, 1529-2401. DOI: 10.1523/JNEUROSCI.1852-08.2008.

Menck, Peter J. and Juergen Kurths (July 2012). "Topological Identification of Weak Points in Power Grids". In: *Nonlinear Dynamics of Electronic Systems, Proceedings of NDES 2012*. Nonlinear Dynamics of Electronic Systems, Proceedings of NDES 2012. Cited by 0000, pp. 1–4.

Menck, Peter J., Jobst Heitzig, Norbert Marwan, and Jürgen Kurths (Feb. 2013). "How basin stability complements the linear-stability paradigm". In: *Nature Physics* 9.2, pp. 89–92. ISSN: 1745-2473. DOI: 10.1038/nphys2516.

Menck, Peter J., Jobst Heitzig, Jürgen Kurths, and Hans Joachim Schellnhuber (June 9, 2014). "How dead ends undermine power grid stability". In: *Nature Communications* 5. DOI: 10.1038/ncomms4969.

Newman, M. E. J. (Oct. 28, 2002). "Assortative Mixing in Networks". In: *Physical Review Letters* 89.20, p. 208701. DOI: 10.1103/PhysRevLett.89.208701.

– (Feb. 27, 2003). "Mixing patterns in networks". In: *Physical Review E* 67.2, p. 026126. DOI: 10.1103/PhysRevE.67.026126.

Nicosia, Vincenzo, Miguel Valencia, Mario Chavez, Albert Diaz-Guilera, and Vito Latora (Apr. 25, 2013). "Remote Synchronization Reveals Network Symmetries

and Functional Modules". In: *Physical Review Letters* 110.17, p. 174102. DOI: 10.1103/PhysRevLett.110.174102.

Nusse, Helena E. and James A. Yorke (Mar. 8, 1996). "Basins of Attraction". In: *Science* 271.5254, pp. 1376–1380. ISSN: 0036-8075, 1095-9203. DOI: 10.1126/science.271.5254.1376.

Oertel, Viola, Anna Rotarska-Jagiela, Vincent G van de Ven, Corinna Haenschel, Konrad Maurer, and David E. J. Linden (Dec. 15, 2007). "Visual hallucinations in schizophrenia investigated with functional magnetic resonance imaging". In: *Psychiatry Research: Neuroimaging* 156.3, pp. 269–273. ISSN: 0925-4927. DOI: 10.1016/j.pscychresns.2007.09.004.

Olmi, Simona, Adrian Navas, Stefano Boccaletti, and Alessandro Torcini (Oct. 6, 2014). "Hysteretic transitions in the Kuramoto model with inertia". In: *Physical Review E* 90.4, p. 042905. DOI: 10.1103/PhysRevE.90.042905.

Omelchenko, Oleh E. and Matthias Wolfrum (Oct. 17, 2012). "Nonuniversal Transitions to Synchrony in the Sakaguchi-Kuramoto Model". In: *Physical Review Letters* 109.16, p. 164101. DOI: 10.1103/PhysRevLett.109.164101.

Ott, Edward (2006). "Basin of attraction". In: *Scholarpedia* 1.8, p. 1701. ISSN: 1941-6016. DOI: 10.4249/scholarpedia.1701.

Ott, Edward and Thomas M. Antonsen (Sept. 1, 2008). "Low dimensional behavior of large systems of globally coupled oscillators". In: *Chaos: An Interdisciplinary Journal of Nonlinear Science* 18.3, p. 037113. ISSN: 1054-1500, 1089-7682. DOI: 10.1063/1.2930766.

Pachauri, Rajendra and Tony Blair (Mar. 6, 2006). *Avoiding Dangerous Climate Change*. Ed. by Hans Joachim Schellnhuber, Wolfgang Cramer, Nebojsa Nakicenovic, Tom Wigley, and Gary Yohe. 1 edition. Cambridge u.a.: Cambridge University Press. 408 pp. ISBN: 9780521864718.

Pazó, Diego (Oct. 18, 2005). "Thermodynamic limit of the first-order phase transition in the Kuramoto model". In: *Physical Review E* 72.4, p. 046211. DOI: 10.1103/PhysRevE.72.046211.

Pecora, Louis M. and Thomas L. Carroll (Mar. 9, 1998). "Master Stability Functions for Synchronized Coupled Systems". In: *Physical Review Letters* 80.10, pp. 2109–2112. DOI: 10.1103/PhysRevLett.80.2109.

Pecora, Louis M., Francesco Sorrentino, Aaron M. Hagerstrom, Thomas E. Murphy, and Rajarshi Roy (June 13, 2014). "Cluster synchronization and isolated desynchronization in complex networks with symmetries". In: *Nature Communications* 5. DOI: 10.1038/ncomms5079.

Peron, Thomas K. DM, Peng Ji, Francisco A. Rodrigues, and Jürgen Kurths (Apr. 2015). "Effect of assortative mixing in the second-order Kuramoto model". In: *arXiv:1504.05447 [nlin, physics:physics]*. arXiv: 1504.05447.

Peron, Thomas Kaue DalMaso and Francisco A. Rodrigues (Nov. 12, 2012a). "Determination of the critical coupling of explosive synchronization transitions in scale-free networks by mean-field approximations". In: *Physical Review E* 86.5, p. 056108. DOI: 10.1103/PhysRevE.86.056108.

Peron, Thomas Kaue DalMaso and Francisco A. Rodrigues (July 6, 2012b). "Explosive synchronization enhanced by time-delayed coupling". In: *Physical Review E* 86.1, p. 016102. DOI: 10.1103/PhysRevE.86.016102.

Petkoski, Spase and Aneta Stefanovska (Oct. 23, 2012). "Kuramoto model with time-varying parameters". In: *Physical Review E* 86.4, p. 046212. DOI: 10.1103/PhysRevE.86.046212.

Pikovsky, Arkady, Michael Rosenblum, and Jürgen Kurths (Apr. 24, 2003). *Synchronization: A Universal Concept in Nonlinear Sciences*. Cambridge University Press. 435 pp. ISBN: 9780521533522.

Radicchi, Filippo and Santo Fortunato (Oct. 13, 2009). "Explosive Percolation in Scale-Free Networks". In: *Physical Review Letters* 103.16, p. 168701. DOI: 10.1103/PhysRevLett.103.168701.

Renier, Laurent A., Irina Anurova, Anne G. De Volder, Synnöve Carlson, John VanMeter, and Josef P. Rauschecker (Oct. 6, 2010). "Preserved Functional Specialization for Spatial Processing in the Middle Occipital Gyrus of the Early Blind". In: *Neuron* 68.1, pp. 138–148. ISSN: 0896-6273. DOI: 10.1016/j.neuron.2010.09.021.

Restrepo, Juan G. and Edward Ott (Sept. 1, 2014). "Mean-field theory of assortative networks of phase oscillators". In: *EPL (Europhysics Letters)* 107.6, p. 60006. ISSN: 0295-5075. DOI: 10.1209/0295-5075/107/60006.

Restrepo, Juan G., Edward Ott, and Brian R. Hunt (Mar. 30, 2005). "Onset of synchronization in large networks of coupled oscillators". In: *Physical Review E* 71.3, p. 036151. DOI: 10.1103/PhysRevE.71.036151.

Riordan, Oliver and Lutz Warnke (July 15, 2011). "Explosive Percolation Is Continuous". In: *Science* 333.6040, pp. 322–324. ISSN: 0036-8075, 1095-9203. DOI: 10.1126/science.1206241.

Risken, Professor Dr Hannes (1984). "Fokker-Planck Equation". In: *The Fokker-Planck Equation*. Springer Series in Synergetics 18. Springer Berlin Heidelberg, pp. 63–95. ISBN: 978-3-642-96809-9, 978-3-642-96807-5.

Rohden, Martin, Andreas Sorge, Marc Timme, and Dirk Witthaut (Aug. 9, 2012). "Self-Organized Synchronization in Decentralized Power Grids". In: *Physical Review Letters* 109.6, p. 064101. DOI: 10.1103/PhysRevLett.109.064101.

Rose, David and David J Pevalin (2003). *A researcher's guide to the national statistics socio-economic classification*. SAGE Publications Ltd.

Schnitzler, Alfons and Joachim Gross (Apr. 2005). "Normal and pathological oscillatory communication in the brain". In: *Nature Reviews. Neuroscience* 6.4, pp. 285–296. ISSN: 1471-003X. DOI: 10.1038/nrn1650.

Sendiña-Nadal, I., I. Leyva, A. Navas, J. A. Villacorta-Atienza, J. A. Almendral, Z. Wang, and S. Boccaletti (Mar. 2015). "Effects of degree correlations on the explosive synchronization of scale-free networks". In: *Physical Review E* 91.3, p. 032811. DOI: 10.1103/PhysRevE.91.032811.

Skardal, P. S., J. Sun, D. Taylor, and J. G. Restrepo (Jan. 1, 2013). "Effects of degree-frequency correlations on network synchronization: Universality and full phase-locking". In: *EPL (Europhysics Letters)* 101.2, p. 20001. ISSN: 0295-5075. DOI: 10.1209/0295-5075/101/20001.

Skardal, Per Sebastian and Alex Arenas (June 24, 2014). "Disorder induces explosive synchronization". In: *Physical Review E* 89.6, p. 062811. DOI: 10.1103/PhysRevE.89.062811.

Skardal, Per Sebastian, Edward Ott, and Juan G. Restrepo (Sept. 16, 2011). "Cluster synchrony in systems of coupled phase oscillators with higher-order coupling". In: *Physical Review E* 84.3, p. 036208. DOI: 10.1103/PhysRevE.84.036208.

Skardal, Per Sebastian, Dane Taylor, and Jie Sun (Sept. 30, 2014). "Optimal Synchronization of Complex Networks". In: *Physical Review Letters* 113.14, p. 144101. DOI: 10.1103/PhysRevLett.113.144101.

Sonnenschein, Bernard and Lutz Schimansky-Geier (May 14, 2012). "Onset of synchronization in complex networks of noisy oscillators". In: *Physical Review E* 85.5, p. 051116. DOI: 10.1103/PhysRevE.85.051116.

– (Nov. 8, 2013). "Approximate solution to the stochastic Kuramoto model". In: *Physical Review E* 88.5, p. 052111. DOI: 10.1103/PhysRevE.88.052111.

Sonnenschein, Bernard, Francesc Sagués, and Lutz Schimansky-Geier (Jan. 2013). "Networks of noisy oscillators with correlated degree and frequency dispersion". In: *The European Physical Journal B* 86.1. ISSN: 1434-6028, 1434-6036. DOI: 10.1140/epjb/e2012-31026-x.

Sorrentino, Francesco, Mario Di Bernardo, and Franco Garofalo (July 1, 2007). "Synchronizability and synchronization dynamics of weighed and unweighed scale free networks with degree mixing". In: *International Journal of Bifurcation and Chaos* 17.7, pp. 2419–2434. ISSN: 0218-1274. DOI: 10.1142/S021812740701849X.

Strogatz, Steven H. (Sept. 1, 2000). "From Kuramoto to Crawford: exploring the onset of synchronization in populations of coupled oscillators". In: *Physica D: Nonlinear Phenomena* 143.1, pp. 1–20. ISSN: 0167-2789. DOI: 10.1016/S0167-2789(00)00094-4.

– (Jan. 2001). *Nonlinear Dynamics And Chaos: With Applications To Physics, Biology, Chemistry, And Engineering*. 1 edition. Cited by 0337. Cambridge, MA: Westview Press. ISBN: 9780738204536.

– (Apr. 14, 2004). *Sync: How Order Emerges From Chaos In the Universe, Nature, and Daily Life*. Reprint edition. New York, NY: Hachette Books. 352 pp. ISBN: 9780786887217.

– (Aug. 26, 2014). *Nonlinear Dynamics and Chaos: With Applications to Physics, Biology, Chemistry, and Engineering*. Westview Press. 531 pp. ISBN: 0813349117.

Su, Guifeng, Zhongyuan Ruan, Shuguang Guan, and Zonghua Liu (Aug. 1, 2013). "Explosive synchronization on co-evolving networks". In: *EPL (Europhysics Letters)* 103.4, p. 48004. ISSN: 0295-5075. DOI: 10.1209/0295-5075/103/48004.

Tanaka, Hisa-Aki, Allan J. Lichtenberg, and Shin'ichi Oishi (Mar. 17, 1997a). "First Order Phase Transition Resulting from Finite Inertia in Coupled Oscillator Systems". In: *Physical Review Letters* 78.11, pp. 2104–2107. DOI: 10.1103/PhysRevLett.78.2104.

– (Feb. 1, 1997b). "Self-synchronization of coupled oscillators with hysteretic responses". In: *Physica D: Nonlinear Phenomena* 100.3, pp. 279–300. ISSN: 0167-2789. DOI: 10.1016/S0167-2789(96)00193-5.

Tass, Peter A. and Milan Majtanik (Jan. 2006). "Long-term anti-kindling effects of desynchronizing brain stimulation: a theoretical study". In: *Biological Cybernetics* 94.1, pp. 58–66. ISSN: 0340-1200. DOI: 10.1007/s00422-005-0028-6.

Trees, B. R., V. Saranathan, and D. Stroud (Jan. 14, 2005). "Synchronization in disordered Josephson junction arrays: Small-world connections and the Kuramoto model". In: *Physical Review E* 71.1, p. 016215. DOI: 10.1103/PhysRevE.71.016215.

Tzourio-Mazoyer, N., B. Landeau, D. Papathanassiou, F. Crivello, O. Etard, N. Delcroix, B. Mazoyer, and M. Joliot (Jan. 2002). "Automated Anatomical Labeling of Activations in SPM Using a Macroscopic Anatomical Parcellation of the MNI MRI Single-Subject Brain". In: *NeuroImage* 15.1, pp. 273–289. ISSN: 1053-8119. DOI: 10.1006/nimg.2001.0978.

Wang, R, T Benner, AG Sorensen, and VJ Wedeen (2007). "Diffusion toolkit: a software package for diffusion imaging data processing and tractography". In: *Proc Intl Soc Mag Reson Med*. Vol. 15. 3720.

Watanabe, Shinya and Steven H. Strogatz (July 1994). "Constants of motion for superconducting Josephson arrays". In: *Physica D: Nonlinear Phenomena* 74.3, p. 197. DOI: 10.1016/0167-2789(94)90196-1.

Wenderoth, Nicole, Filiep Debaere, Stefan Sunaert, and Stephan P. Swinnen (July 1, 2005). "The role of anterior cingulate cortex and precuneus in the coordination of motor behaviour". In: *European Journal of Neuroscience* 22.1, pp. 235–246. ISSN: 1460-9568. DOI: 10.1111/j.1460-9568.2005.04176.x.

Wiley, Daniel A., Steven H. Strogatz, and Michelle Girvan (Mar. 1, 2006). "The size of the sync basin". In: *Chaos: An Interdisciplinary Journal of Nonlinear Science* 16.1, p. 015103. ISSN: 1054-1500, 1089-7682. DOI: 10.1063/1.2165594.

Witthaut, Dirk and Marc Timme (Aug. 1, 2012). "Braess's paradox in oscillator networks, desynchronization and power outage". In: *New Journal of Physics* 14.8, p. 083036. ISSN: 1367-2630. DOI: 10.1088/1367-2630/14/8/083036.

Xia, Mingrui, Jinhui Wang, and Yong He (July 2013). "BrainNet Viewer: A Network Visualization Tool for Human Brain Connectomics". In: *PLoS ONE* 8.7, e68910. DOI: 10.1371/journal.pone.0068910.

Xulvi-Brunet, R. and I. M. Sokolov (Dec. 2, 2004). "Reshuffling scale-free networks: From random to assortative". In: *Physical Review E* 70.6, p. 066102. DOI: 10.1103/PhysRevE.70.066102.

Zhang, Xiyun, Xin Hu, J. Kurths, and Zonghua Liu (July 15, 2013). "Explosive synchronization in a general complex network". In: *Physical Review E* 88.1, p. 010802. DOI: 10.1103/PhysRevE.88.010802.

Zhang, Xiyun, Stefano Boccaletti, Shuguang Guan, and Zonghua Liu (Jan. 21, 2015). "Explosive Synchronization in Adaptive and Multilayer Networks". In: *Physical Review Letters* 114.3, p. 038701. DOI: 10.1103/PhysRevLett.114.038701.

Zhao, Weihua, Lizhu Luo, Qin Li, and Keith M. Kendrick (Aug. 15, 2013). "What Can Psychiatric Disorders Tell Us about Neural Processing of the Self?" In: *Frontiers in Human Neuroscience* 7. ISSN: 1662-5161. DOI: 10.3389/fnhum.2013.00485.

Zhou, Changsong and Jürgen Kurths (Mar. 1, 2006). "Hierarchical synchronization in complex networks with heterogeneous degrees". In: *Chaos: An Interdisciplinary*

Journal of Nonlinear Science 16.1, p. 015104. ISSN: 1054-1500, 1089-7682. DOI: 10.1063/1.2150381.

Zhu, Liuhua, Liang Tian, and Daning Shi (Oct. 28, 2013). "Criterion for the emergence of explosive synchronization transitions in networks of phase oscillators". In: *Physical Review E* 88.4, p. 042921. DOI: 10.1103/PhysRevE.88.042921.

Zou, Yong, Tiago Pereira, Michael Small, Zonghua Liu, and Jürgen Kurths (Mar. 18, 2014). "Basin of Attraction Determines Hysteresis in Explosive Synchronization". In: *Physical Review Letters* 112.11, p. 114102. DOI: 10.1103/PhysRevLett.112.114102.

Selbständigkeitserklärung

Ich erkläre, dass ich die vorliegende Arbeit selbständig und nur unter Verwendung der angegebenen Literatur und Hilfsmittel angefertigt habe.

Potsdam, den 21. September 2015 Peng Ji